AWARD NUMBER: W81XWH-18-1-0082

TITLE: Design of a 3D Mammography System in the Age of Personalized Medicine

PRINCIPAL INVESTIGATOR: Raymond J. Acciavatti, Ph.D.

CONTRACTING ORGANIZATION: University of Pennsylvania
Philadelphia, PA 19104

REPORT DATE: April 2020

TYPE OF REPORT: Annual

PREPARED FOR: U.S. Army Medical Research and Development Command
Fort Detrick, Maryland 21702-5012

REPORT DOCUMENTATION PAGE

Form Approved
OMB No. 0704-0188

1. REPORT DATE	2. REPORT TYPE	3. DATES COVERED
April 2020	Annual	15 March 2019 – 14 March 2020

4. TITLE AND SUBTITLE

Design of a 3D Mammography System in the Age of Personalized Medicine

5a. CONTRACT NUMBER

5b. GRANT NUMBER
W81XWH-18-1-0082

5c. PROGRAM ELEMENT NUMBER

6. AUTHOR(S)

Raymond J. Acciavatti, Ph.D.

E-Mail: racci@pennmedicine.upenn.edu

5d. PROJECT NUMBER

5e. TASK NUMBER

5f. WORK UNIT NUMBER

7. PERFORMING ORGANIZATION NAME(S) AND ADDRESS(ES)

University of Pennsylvania
Philadelphia, PA 19104

8. PERFORMING ORGANIZATION REPORT NUMBER

9. SPONSORING / MONITORING AGENCY NAME(S) AND ADDRESS(ES)

U.S. Army Medical Research and Development Command
Fort Detrick, Maryland 21702-5012

10. SPONSOR/MONITOR'S ACRONYM(S)

11. SPONSOR/MONITOR'S REPORT NUMBER(S)

12. DISTRIBUTION / AVAILABILITY STATEMENT

Approved for Public Release; Distribution Unlimited

13. SUPPLEMENTARY NOTES

14. ABSTRACT

Despite the latest move toward 3D breast cancer screening with digital breast tomosynthesis (DBT), current systems continue to suffer from blurring in calcification imaging. We performed virtual clinical trials (VCTs) of anthropomorphic phantoms to analyze calcification detection in DBT. Additionally, we investigated super-resolution (SR) as a mechanism to improve calcification visibility. It is known from previous work that there are anisotropies in SR in current systems and that these anisotropies can be eliminated with the use of detector motion. We have recently shown that it is possible to eliminate the anisotropies by re-arranging the source positions in clusters with submillimeter spacing. This new design eliminates the need for detector motion and hence the need for a thick detector housing, which is cumbersome for patients. We have also modeled SR in magnification imaging, and showed that SR is optimized by circular source motions as opposed to linear motions. In addition, we analyzed how personalized acquisition geometries, customized around the size and shape of the breast, improve dense tissue visualization. While our early work was focused on Defrise phantoms, this analysis has recently expanded to anthropomorphic phantoms. We validated this phantom model as having realistic textural detail compared against clinical data.

15. SUBJECT TERMS

Digital breast tomosynthesis (DBT), mammography, super-resolution, personalized medicine, Defrise phantom, image reconstruction, calcification, virtual clinical trial, magnification mammography.

16. SECURITY CLASSIFICATION OF:			17. LIMITATION OF ABSTRACT	18. NUMBER OF PAGES	19a. NAME OF RESPONSIBLE PERSON
a. REPORT	b. ABSTRACT	c. THIS PAGE			USAMRMC
Unclassified	Unclassified	Unclassified	Unclassified	114	19b. TELEPHONE NUMBER *(include area code)*

Table of Contents

1. INTRODUCTION

In digital breast tomosynthesis (DBT), a reconstruction is generated from multiple x-ray projection views acquired over a narrow range of angles.[1-3] Rafferty *et al*. showed that DBT offers an improvement in mass imaging over conventional 2D digital mammography (DM).[4] However, one disadvantage of DBT is blurring in images of calcifications. These lesions can act as an early sign of breast cancer.[5] We are investigating super-resolution (SR) as a mechanism to improve calcification visibility.[6] In the past 12 months, we have successfully used virtual clinical trials (VCTs) with anthropomorphic voxel phantoms[7,8] to demonstrate the improvements in calcification detection with the use of SR. Additionally, we have shown that more complex motions for the x-ray tube give rise to SR with even better quality and at more positions in the image. Another benefit of these new scanning motions is improving the visualization of dense tissue. To maximize the image quality, we have shown that the scanning motion should be personalized to the woman being imaged; specifically, to the size of the breast.[9] A key advantage of VCTs is that these new system designs for DBT are being identified and optimized in a rapid and cost-effective manner without requiring human subject recruitment.[10]

2. KEYWORDS

Digital breast tomosynthesis (DBT), mammography, super-resolution, personalized medicine, Defrise phantom, image reconstruction, calcification, virtual clinical trial, magnification mammography.

3. ACCOMPLISHMENTS

3.A. What were the major goals of the project?

The Statement of Work is shown below, focusing on Years 1-2. Milestones achieved in the past 12 months are summarized for each of the major tasks. More detail about these milestones is given in Section 3.B.

3.A.1. Specific Aim 1: Design a personalized image acquisition technique for screening mammography.

Specific Aim 1: Design a personalized image acquisition technique for screening mammography.	**Timeline (Months)**
Major Task 1: Optimize super-resolution (SR) with simulations of high-frequency, sinusoidal test objects and calculations of the *r*-factor.	
Subtask 1: Develop a design for optimizing SR. Through our prototype system, we learned that SR can be optimized by introducing detector motion that varies the source-to-image distance (SID) during the scan. However, to minimize the need for a thick detector housing, we will investigate more complex combinations of x-ray tube and detector motion that can be used to optimize SR.	1-12
Subtask 2: Make refinements to the motions of the x-ray tube and detector based on the on-going results of the virtual clinical trial (VCT) in specific aim 3.	13-30
Milestones Achieved In the Past 12 Months: Model of super-resolution using high-frequency test objects in DBT (documents 2, 3, 7, and 9 of Section 9); Theoretical model of new DBT system design with x-ray source positions re-arranged in clusters with submillimeter spacing (documents 3 and 7 of Section 9).	
Major Task 2: Simulate the reconstruction of glandular and adipose tissue with Defrise phantoms.	
Subtask 1: Prepare Defrise phantoms modeled in the shape of breasts.	1-3
Subtask 2: Simulate the image acquisition. First, a 2D scout image is acquired at low radiation dose. Second, the 3D scan parameters are determined based on estimates of the breast size, shape, and internal composition.	4-9
Subtask 3: Prepare reconstructions, and calculate the relative contrast at the septa between glandular and adipose tissue.	10-15
Subtask 4: Determine the effect of the reconstruction filter on the relative contrast. To optimize the image quality, the filter will be personalized to the phantom.	16-21

Subtask 5: Update the reconstructions and calculations of contrast as new acquisition geometries are identified based on the on-going results of the virtual clinical trial in specific aim 3.	22-30
Milestone Achieved in the Past 12 Months: Manuscript draft on Defrise phantoms and personalized scanning motions (document 1 of Section 9) being prepared for journal submission.	
Major Task 3: Develop a personalized acquisition geometry yielding a more accurate segmentation of the breast outline.	
Subtask 1: Prepare database of binary phantom masks (uniform phantoms with no internal composition). These will be used to calculate the breast outline (convex hull) in the reconstruction.	4-6
Subtask 2: Determine the motions of the x-ray tube and detector that yield the most accurate breast outline segmentation. These motions will be personalized to the breast size and shape based on a 2D scout image.	7-21
Milestone Achieved in the Past 12 Months: Development of automated thresholding technique for breast outline segmentation as described in document 1 of Section 9 (manuscript draft on Defrise phantoms and personalized scanning motions).	

3.A.2. Specific Aim 2: Design a 3D Magnification Mammography Call-Back Exam.

Specific Aim 2: Design a 3D Magnification Mammography Call-Back Exam.	**Timelines (Months)**
Major Task 4: Optimize super-resolution (SR).	
Subtask 1: Develop designs for the source and detector motion that optimize SR in magnification imaging. This will ensure the highest image quality in imaging calcifications (small, closely-spaced structures).	1-12
Subtask 2: Make refinements to the motion of the x-ray tube and detector based on the on-going results of the virtual clinical trial in specific aim 3.	13-30
Milestones Achieved in the Past 12 Months: Theoretical model of SR in magnification tomosynthesis; Comparative analysis of circular and linear scanning motions, as described in Section 3.B.2. of this report.	
Major Task 5: Perform a contrast-detail reader study.	
Subtask 1: Simulate a contrast-detail (C-D) array in a uniform background at different positions. The scan parameters for the 3D acquisition will be customized around the region containing the C-D array.	7-12
Subtask 2: Perform a reader study. Prepare plots of the smallest thickness visible as a function of the cross-sectional area of the lesion. Determine how a personalized 3D acquisition compares against: (1) a non-personalized 3D acquisition, and (2) 2D magnification imaging (the current gold standard).	13-18
Subtask 3: Repeat subtasks 1 and 2 with the C-D array in structured (anatomical) backgrounds. Determine how the breast background (density and texture) impacts the reader performance.	19-24
Milestone Achieved in the Past 12 Months: Database of calcification polycubes with varying size (detail) and varying contrast (percentage of hydroxyapatite, or weighting fraction), as described in documents 5, 8, and 10 of Section 9 – enables future simulations of magnification tomosynthesis.	

3.A.3. Specific Aim 3: Evaluate the new designs for screening and call-back imaging with a virtual clinical trial.

Specific Aim 3: Evaluate the new designs for screening and call-back imaging with a virtual clinical trial.	**Timeline (Months)**
Major Task 6: Quantify breast density in anatomical phantoms.	
Subtask 1: Prepare anatomical phantoms with variable size, shape, and internal composition.	1-3
Subtask 2: Simulate x-ray images in personalized and non-personalized acquisition geometries.	4-6
Subtask 3: Calculate reconstructions. Model the differentiation between adipose and glandular tissue as a binary classification task with a receiver operating characteristic (ROC) curve.	7-12

Subtask 4: Optimize the reconstruction filter; it will be personalized to the phantom. The filter should maximize the area under the ROC curve.	13-18
Subtask 5: Repeat subtasks 2-4 as on-going refinements are made to the motion paths of the x-ray tube and detector, as well as the reconstruction filter. We are working to maximize the area under the ROC curve.	19-30
Milestone Achieved in the Past 12 Months: ROC curves modeling differentiation of adipose and glandular tissue in anatomical phantoms, illustrating the benefits of new scanning motions in DBT (described in Section 3.B.3. of this report).	
Major Task 7: Perform a virtual clinical trial (VCT) with simulated lesions.	
Subtask 1: Prepare computational breast phantoms with lesions (masses and calcifications) of variable size, shape, and contrast.	1-6
Subtask 2: Design the VCT. Numerical observers will be trained on the statistics of images. Channelized Hotelling Observer parameters will be determined to match the performance of the observer on real and breast model images.	7-12
Subtask 3: Conduct the VCT. The sensitivity index (d') and call-back rate will be estimated for the detection and characterization of lesions in different system designs. These calculations will be used to compare new acquisition geometries against conventional acquisition geometries.	13-30
Milestone Achieved in the Past 12 Months: Virtual clinical trials of breast phantom models with simulated lesions (documents 5, 7, and 8 of Section 9); Validation of breast phantom model (document 6 of Section 9); X-ray technique optimization for breast phantom (document 4 of Section 9).	

3.B. What was accomplished under these goals?

3.B.1. Specific Aim 1: Design a personalized image acquisition technique for screening mammography.

Optimizing Calcification Imaging:

First, we tackled the problem of improving calcification visibility in DBT. To optimize this imaging task, we have shown that the x-ray source positions should be re-arranged in "clusters"[11]; this idea is illustrated in Fig. 1. This design differs from a conventional DBT system in which the source positions are equally spaced over a circular arc.[2] This design can be implemented by rapidly pulsing the x-ray source during a continuous sweep of the x-ray tube. We have written two papers on this new design: a paper presented at the 2020 SPIE Medical Imaging Conference in Houston, TX (document 3 of Section 9), and a paper accepted for presentation at the International Workshop on Breast Imaging (IWBI) in May 2020 (document 7 of Section 9). As of this report, it is projected that the IWBI conference presentation will be given virtually.

We have analyzed super-resolution (SR) as the mechanism for improving calcification visibility. SR can be demonstrated with high-resolution test patterns, as described in documents 2, 3, 7, and 9 of Section 9. Based on our analysis of these test patterns, we have concluded that clinical DBT systems are not yet designed to maximize SR, and that there are unavoidable anisotropies in SR.[6,12,13] This idea is illustrated in Fig. 2 showing anisotropies at the positions denoted by the arrows. Prior to this DoD grant, we proposed the idea of detector motion to eliminate these anisotropies.[12] While detector motion was proven to be an effective strategy for optimizing SR, it requires a thicker (bulkier) detector housing, which can be cumbersome for patient positioning. The advantage of our newly proposed design (Fig. 1) is that the anisotropies can be eliminated without requiring detector motion. For this reason, we have successfully met our goal to optimize SR without requiring a thick (bulky) detector housing.

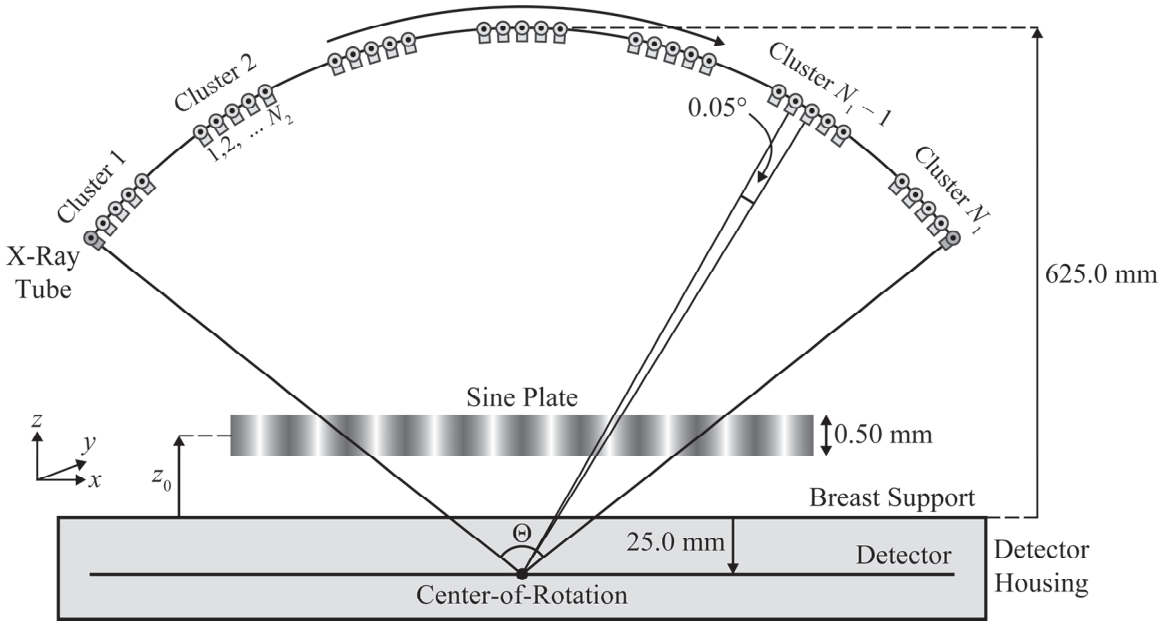

Figure 1. In conventional DBT, the source positions are equally spaced over an arc. As an anti-aliasing strategy, we developed a new system design in which the source positions are re-arranged in clusters. There are N_1 clusters and N_2 source positions per cluster. This figure is adapted from document 3 of Section 9.

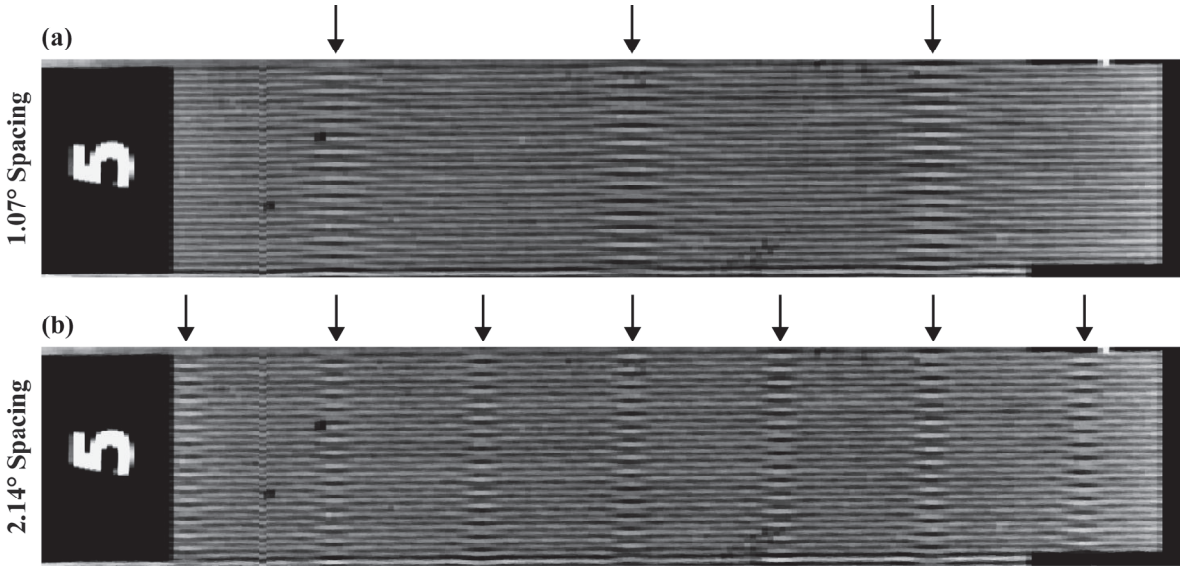

Figure 2. There are aliasing artifacts (anisotropies) at the positions denoted by the arrows. This figure is adapted from document 3 of Section 9.

Optimizing Dense Tissue Visualization:

In clinical DBT systems, the x-ray tube moves in only one direction (laterally). Our new DBT system includes an additional component of x-ray tube motion in the posteroanterior (PA) direction. We have used virtual Defrise phantoms to illustrate the advantage of this motion in terms of dense tissue visualization. This work is summarized in document 1 of Section 9 (a paper draft that we are preparing for submission to a journal); this document expands upon our SPIE 2019 conference proceedings manuscript[9], which was included with last year's progress report. Each phantom is modeled in the shape of a breast, and consists of alternating bands of dense and adipose tissue. In a conventional scan [Fig. 3(a)], there are blurring and streaking artifacts, making it difficult to see the interfaces between dense and adipose tissue. These artifacts are eliminated in a scan with 90.0 mm of PA source motion [Fig. 3(b)].

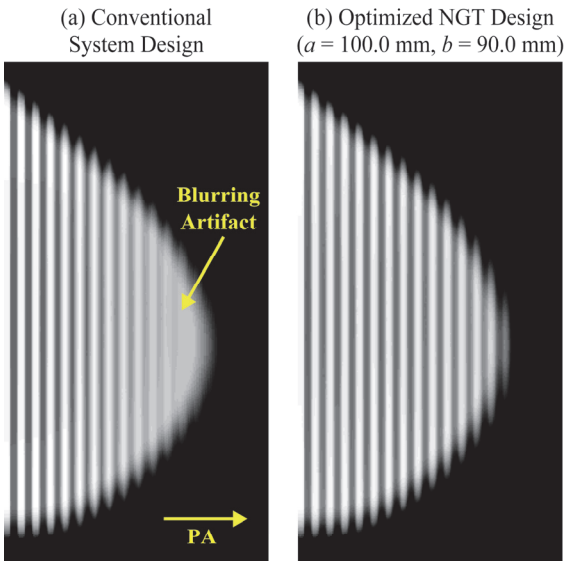

Figure 3. Dense tissue visualization is improved in our new system design with PA source motion. Customizing the PA motion around the size of the breast (chest wall-to-nipple distance) yields the highest possible image quality. This figure is adapted from the work of Acciavatti *et al*.[9]

To date, we have simulated 120 Defrise phantoms in 441 acquisition geometries, corresponding to 21 ranges of source motion laterally and 21 ranges of source motion posteroanteriorly. We identified the best scanning motion for each phantom by analyzing the reconstruction voxel-by-voxel as a binary classification task with a receiver operating characteristic (ROC) curve.[14] We demonstrated that each phantom was optimized by a different scanning motion, and that this motion is dependent on the chest wall-to-nipple distance (CND). In phantoms with a larger CND, it is necessary to translate the source further from the chest-wall plane to optimize the image quality. Based on these results, we successfully met our goal of demonstrating that image quality is improved by personalizing the scanning motion to the woman being imaged; specifically, to the size of the breast. Our progress is summarized in document 1 of Section 9.

3.B.2. Specific Aim 2: Design a 3D Magnification Mammography Call-Back Exam.

In breast imaging, the technology for call-back imaging (magnification mammography) has not kept up with the advancements made in screening. Clinical magnification mammography still relies on conventional 2D imaging techniques. In magnification mammography, a 2D image is acquired with the breast elevated closer to the x-ray source. Our goal is to design a 3D magnification exam with the highest possible spatial resolution (Fig. 4).

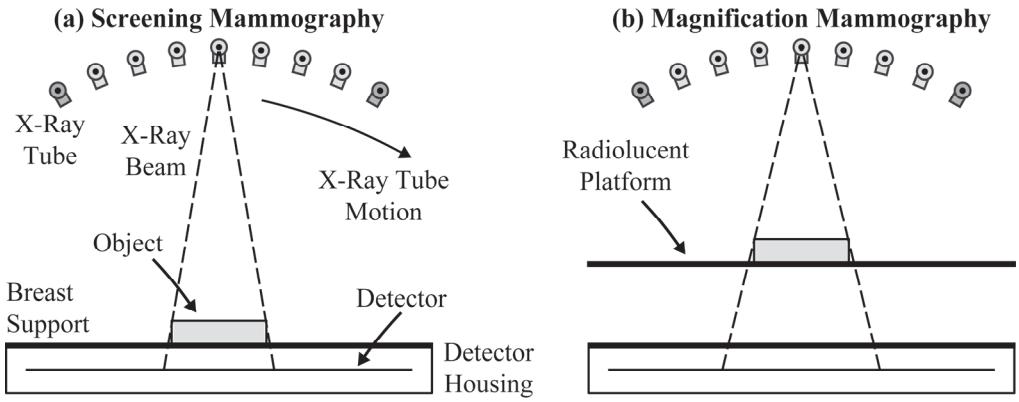

Figure 4. Schematic diagram of the acquisition geometry in screening mammography and magnification mammography.

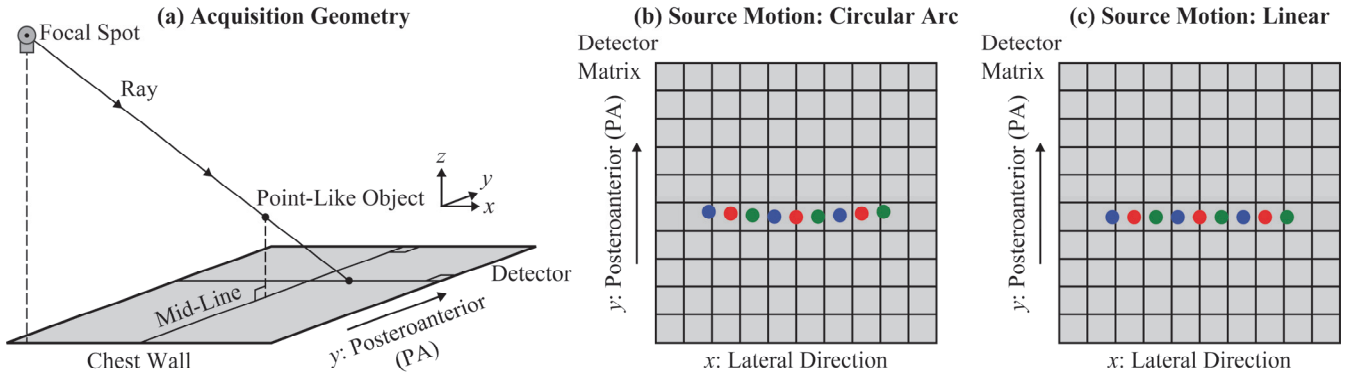

Figure 5. In a system with linear source motion, super-resolution is not achieved in the *y* direction (PA), since there are no subpixel shifts in the image of the object between projections. However, if the source rotates in a circular arc, subpixel shifts in the image of the object are indeed present in the *y* direction and these shifts become more pronounced with increasing magnification. This figure is adapted from document 7 of Section 9.

Similar to specific aim 1, we have focused on optimizing calcification imaging, specifically in terms of ensuring that super-resolution (SR) is achieved without anisotropies. We compared two scanning motions: linear and circular. Fig. 5 illustrates the projection images of a point-like object for these two motions. In a system with linear x-ray source motion (hence no change in *z*), there are no shifts in the in the *y* direction (PA) and thus SR cannot be achieved in this direction. However, with the use of x-ray tube motion in a circular arc [Fig. 4(b)], the shifts in the PA direction become more pronounced, and for this reason, one would expect SR to be feasible in magnification tomosynthesis. We now provide the mathematical proof of this result.

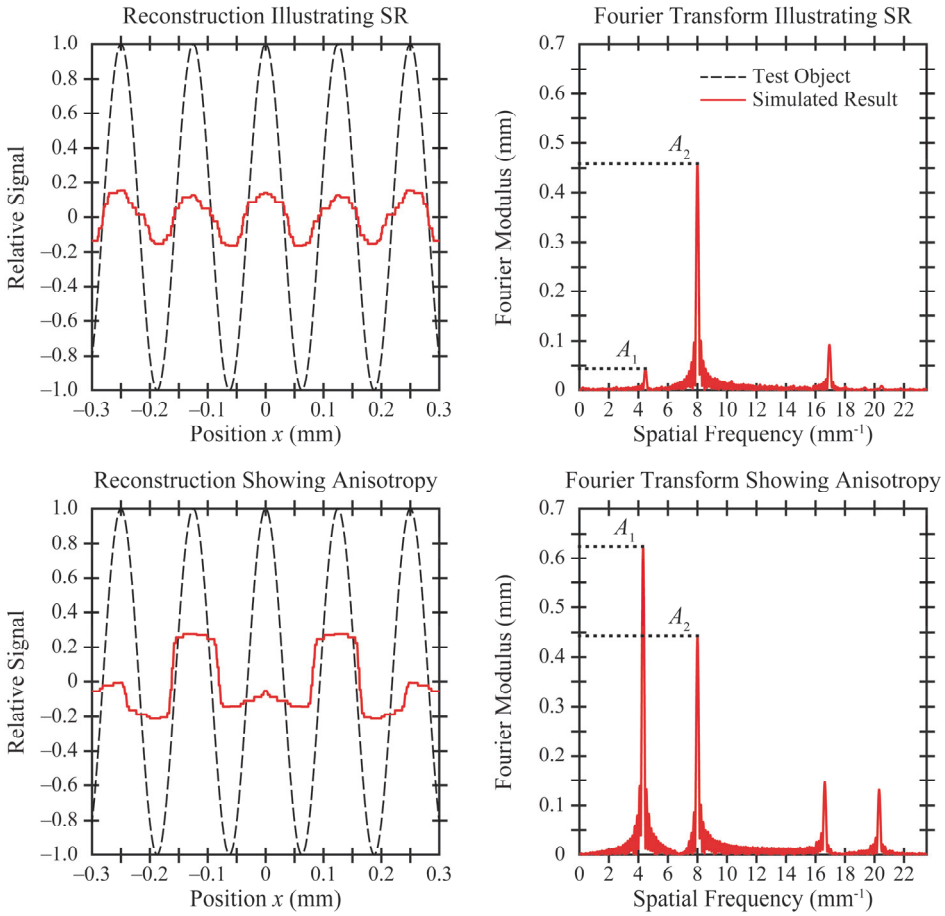

Figure 6. The Fourier transform of the reconstruction is analyzed in terms of two peaks: one at the input frequency (A_2) and one at a lower frequency (A_1). This figure is adapted from document 3 of Section 9.

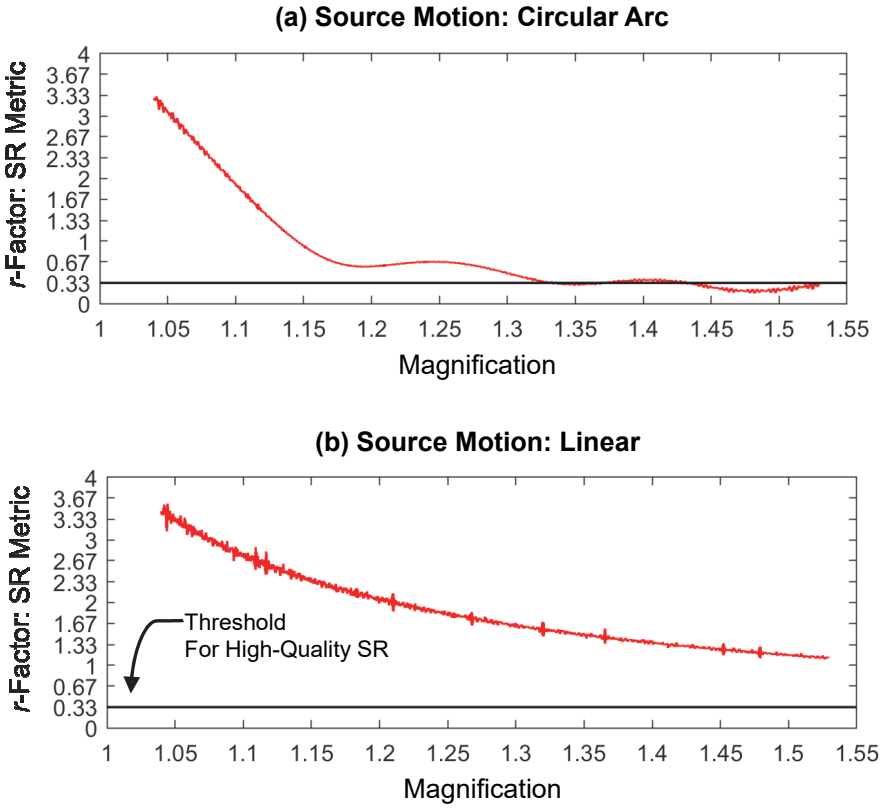

Figure 7. The *r*-factor quantifies anisotropies in super-resolution or SR (a measure of image quality). In a linear scanning motion, high-quality SR cannot be achieved in the PA direction at any magnification, since *r*-factor exceeds the threshold of 1/3. However, in a circular scanning motion, high-quality SR can be achieved in the PA direction at magnifications exceeding 1.33. For the purpose of this simulation, the sine wave was centered at the position 25.0 mm anterior to the chest wall.

Fig. 6 provides an overview of the methods used to identify the anisotropies in SR. These methods are described in detail in documents 3 and 7 of Section 9, where the reconstruction of a sinusoidal test object is calculated from first principles. The Fourier transform has a major peak at the input frequency if the object is resolved [Fig. 6(b)], but has a major peak at a lower frequency if the object is aliased [Fig. 6(d)]. In order for SR to be achieved with high quality, the *r*-factor (ratio of amplitudes A_1 to A_2) should be as small as possible. In documents 3 and 7 of Section 9, we set the following threshold for high-quality SR: *r*-factor < 1/3. To identify all the coordinates of the anisotropies, we generated a plot of *r*-factor as a function of the magnification (Fig. 7). In the system with x-ray tube motion in a circular arc [Fig. 7(a)], the *r*-factor falls below the threshold of 1/3 at a magnification of 1.33 (a *z*-coordinate of 137.5 mm above the breast support). Hence the anisotropies in SR in the PA direction are eliminated entirely at magnifications exceeding 1.33. A linear scanning motion does not achieve SR at any magnification [Fig. 7(b)]. Based on these results, we conclude that a linear scanning motion is not optimal for magnification tomosynthesis and that a circular scanning motion offers better image quality.

3.B.3. Specific Aim 3: Evaluate the New Designs for Screening and Call-Back Imaging with a Virtual Clinical Trial

Calcification Imaging:

We have performed virtual clinical trials (VCTs) with anthropomorphic voxel phantoms to analyze calcification detection in various system designs for mammography:

- Complementing specific aim 1, we have used VCTs to validate super-resolution (SR) as a mechanism for improving calcification detection (document 8 of Section 9).

- Using VCT software, we have validated the existence of anisotropies in SR, as we predicted in specific aim 1 with theoretical modeling. We have shown that these anisotropies can impact the way calcifications are portrayed in the image (document 7 of Section 9).
- We have analyzed how the detection of calcifications is dependent on the range of x-ray tube motion, and have used VCTs to optimize the x-ray tube motion (document 5 of Section 9).
- VCTs were extensively used by a summer student (Brian Vu, University of Houston) mentored by the PI (Raymond Acciavatti) between 6/3/2019 and 8/9/2019. Brian participated in the AAPM summer undergraduate fellowship program as well as the Summer Undergraduate Program for Educating Radiation Scientists (SUPERS) at the University of Pennsylvania. He prepared an abstract and gave a presentation on 8/7/2019, describing how calcification visibility differs between synthetic 2D mammography, conventional 2D DM, and 3D DBT (document 10 of Section 9).

(a) Conventional Design **(b) New Design with PA Source Motion**

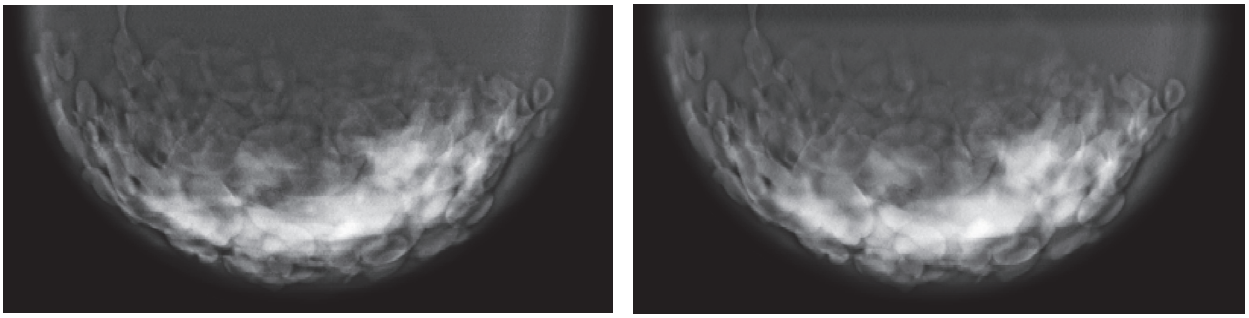

Figure 8. Reconstruction of anthropomorphic voxel phantom under two different system designs.

Dense Tissue Visualization:

In specific aim 1, we used Defrise phantoms (Fig. 3) to investigate how dense tissue visualization is improved in our new system design. We have performed the same analysis with anthropomorphic voxel phantoms in VCTs; the ROC methods are based off those described in document 1 of Section 9. These results are illustrated for one phantom in Figs. 8-9; i.e., a 52.5 mm thick phantom with 18.9% density and a volume of 270 mL. For the purpose of this simulation, the conventional system is modeled with source motion in the x direction (laterally), while the new design is modeled with an additional component of source motion in the y direction (posteroanteriorly). The area under the ROC curve (AUC) is higher in the new design [Fig. 9(b)] than in the conventional design [Fig. 9(a)], and hence dense tissue is visualized better. The AUC results can be analyzed further[7,15] in terms of the detectability index d'.

$$d' = 2 \cdot \mathrm{erf}^{-1}\left(2 \cdot \mathrm{AUC} - 1\right) \tag{1}$$

The d' values for the conventional and new designs are 0.464 and 0.741, respectively (effectively increasing the signal-to-noise ratio by 60% in our new design).

To ensure that our VCTs include the most realistic breast phantoms possible, we have validated that our breast phantom model has realistic parenchymal texture relative to clinical data (document 6 of Section 9). We have also acquired images of a breast phantom over many technique settings (document 4 of Section 9) and are using this analysis for x-ray technique optimization in VCTs.

(a) Conventional Design **(b) New Design with PA Source Motion**

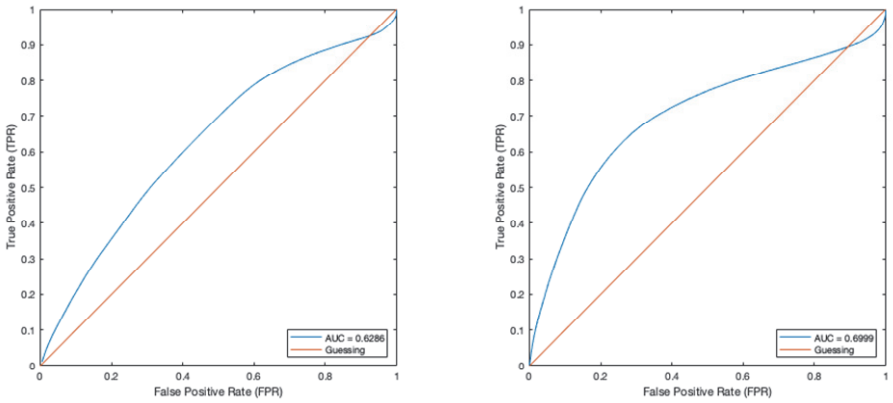

Figure 9. ROC results for dense tissue visualization in two system designs. The area under the curve is improved in the new design with PA source motion.

3.C. What opportunities for training and professional development has the project provided?

- The PI (Raymond Acciavatti) was a mentor for the summer undergraduate fellowship program through the American Association of Physicists in Medicine (AAPM) between 6/3/19 and 8/9/19. The research performed by the summer student is described in document 10 of Section 9; it is complementary to the VCTs in Specific Aim 3 (Section 3.B.3.).

- At the SPIE Medical Imaging Conference in Houston, the PI (Raymond Acciavatti) was a teaching assistant for the class "SC1239: Virtual Clinical Trials: An In-depth Tutorial", which was held on 2/18/2020. The class instructors were Andrew Maidment, Predrag Bakic, and Bruno Barufaldi (all from the University of Pennsylvania). This class on VCTs is complementary to research conducted in Specific Aim 3 (Section 3.B.3.).

3.D. How were the results disseminated to communities of interest?

- Our work on VCTs was presented in a "Live Demonstration" session on 2/16/2020 at the SPIE Medical Imaging conference in Houston. Conference attendees were given a demonstration of our VCT software. The PI (Raymond Acciavatti) was a co-author on this demonstration.

3.E. What do you plan to do during the next reporting period to accomplish the goals?

We have the following goals for the next 12 months:

3.E.1. Specific Aim 1: Design a personalized image acquisition technique for screening mammography.

- Finalize document 1 of Section 9 for submission to a journal – personalized scanning motions for dense tissue visualization in Defrise phantoms (Fig. 3 of Section 3.B.1.).
- Expand our conference proceedings manuscripts on optimizing super-resolution for calcification imaging (documents 3 and 7 of Section 9) for submission to a journal (Figs. 1-2 of Section 3.B.1.).

3.E.2. Specific Aim 2: Design a 3D Magnification Mammography Call-Back Exam.

- In magnification mammography, we have modeled SR in one direction (PA) as described in Section 3.B.2. In our future work, we will model high-frequency test objects oriented in other directions to prove that our new design is capable of isotropic SR (i.e., SR in all directions).

3.E.3. Specific Aim 3: Evaluate the New Designs for Screening and Call-Back Imaging with a Virtual Clinical Trial

- Expand VCT simulations of screening mammography to model personalized scanning motions, similar to those considered in document 1 of Section 9. The VCTs will model anthropomorphic phantoms with lesions using scanning motions customized to the phantom being imaged.
- Conduct VCT simulations of magnification tomosynthesis, guided by the scanning motions derived in Specific Aim 2.

4. IMPACT

4.A. What was the impact on the development of the principal discipline(s) of the project?

Impact on Screening Mammography:

In screening mammography, our work has an impact on both low- and high-frequency imaging tasks.

- We have shown that image quality is improved by customizing the scanning motion around the size of the breast; this improves dense tissue visualization (a low-frequency imaging task) as described in document 1 of Section 9.

- We have shown that super-resolution can be achieved with better quality at more positions in the image by re-designing the scanning motion (Fig. 1). This improves the visualization of calcifications (a high-frequency imaging task), as described in documents 3 and 7 of Section 9.

Impact on Magnification Mammography (A Call-Back Exam):

In document 7 of Section 9, we show that a screening exam requires PA source motion to optimize SR. Fig. 7 suggests that magnification tomosynthesis (a call-back exam) does not require the use of PA source motion. This result is significant, since it means that a magnification tomosynthesis exam can be done at a shorter scan time than the screening exam. The benefit of a short scan time is that there is less potential for patient motion (which could introduce blurring artifacts in the image).

4.B. What was the impact on other disciplines?
Nothing to report.

4.C. What was the impact on technology transfer?
Nothing to report.

4.D. What was the impact on society beyond science and technology?
Nothing to report.

5. CHANGES / PROBLEMS

5.A. Changes in approach and reasons for change
Nothing to report.

5.B. Actual or anticipated problems or delays and actions or plans to resolve them
Nothing to report.

5.C. Changes that had a significant impact on expenditures
Nothing to report.

5.D. Significant changes in use or care of human subjects, vertebrate animals, biohazards, and/or select agents
Nothing to report.

5.E. Significant changes in use or care of human subjects
Nothing to report.

5.F. Significant changes in use or care of vertebrate animals
Nothing to report.

5.G. Significant changes in use of biohazards and/or select agents
Nothing to report.

6. PRODUCTS.

6.A. Publications, conference papers, and presentations

- **Journal publications**
  - Acciavatti RJ, Cohen EA, Maghsoudi OH, Gastounioti A, Pantalone L, Hsieh M-K, Barufaldi B, Bakic PR, Chen J, Conant EF, Kontos D, Maidment ADA. Calculation of Radiomic Features to Validate the Textural Realism of Physical Anthropomorphic Phantoms for Digital Mammography (IWBI 2020, in press).
  - Acciavatti RJ, Vent TL, Barufaldi B, Wileyto EP, Noël PB, Maidment ADA. Super-Resolution in Digital Breast Tomosynthesis: Limitations of the Conventional System Design and Strategies for Optimization (IWBI 2020, in press).
  - Barufaldi B, Vent TL, Acciavatti RJ, Bakic PR, Noël PB, Maidment ADA. MRMC ROC Analysis of Calcification Detection in Tomosynthesis Using Computed Super-Resolution and Virtual Clinical Trials (IWBI 2020, in press).
  - Vent TL, Barufaldi B, Acciavatti RJ, Maidment ADA. Simulation of High-Resolution Test Objects using Non-Isocentric Acquisition Geometries in Next-Generation Digital Tomosynthesis (IWBI 2020, in press).

- **Books or other non-periodical, one-time publications**
  - Nothing to report.

- **Other publications, conference papers, and presentations**
  - Acciavatti RJ, Vent TL, Barufaldi B, Wileyto EP, Noël PB, Maidment ADA. Proposing Rapid Source Pulsing for Improved Super-Resolution in Digital Breast Tomosynthesis. In: Chen G-H, Bosmans H, editors; Physics of Medical Imaging; 2020; Houston, TX: SPIE; 2020. p. 113125G. The PI (Raymond Acciavatti) presented this work as a poster at the SPIE Medical Imaging conference on 2/17/2020 in Houston, TX.
  - Acciavatti RJ, Cohen EA, Maghsoudi OH, Gastounioti A, Pantalone L, Hsieh M-K, Conant EF, Scott CG, Winham SJ, Kerlikowske K, Vachon C, Maidment ADA, Kontos D. Robust Radiomic Feature Selection in Digital Mammography: Understanding the Effect of Imaging Acquisition Physics Using Phantom and Clinical Data Analysis. In: Hahn HK, Mazurowski MA, editors; Computer-Aided Diagnosis; 2020; Houston, TX: SPIE; 2020. p. 113140W. The PI (Raymond Acciavatti) gave an oral presentation at the SPIE Medical Imaging conference on 2/17/2020 in Houston, TX.

- Barufaldi B, Vent TL, Acciavatti RJ, Bakic PR, Noël PB, Conant EF, Maidment ADA. Determining the Optimal Angular Range of the X-Ray Source Motion in Tomosynthesis Using Virtual Clinical Trials. In: Chen G-H, Bosmans H, editors; Physics of Medical Imaging; 2020; Houston, TX: SPIE; 2020. p. 113120I. Bruno Barufaldi (first author of this paper) gave an oral presentation at the SPIE Medical Imaging conference on 2/16/2020 in Houston, TX.

6.B. Website(s) or other Internet site(s)
The VCT software developed at the University of Pennsylvania can be accessed through the website https://sourceforge.net/projects/openvct/.

6.C. Technologies or techniques
Nothing to report.

6.D. Inventions, patent applications, and/or licenses
Nothing to report.

6.E. Other products
Nothing to report.

7. PARTICIPANTS AND OTHER COLLABORATING ORGANIZATIONS.

7.A. What individuals have worked on the project?

Name:	Raymond J. Acciavatti, Ph.D.
Project Role:	Principal Investigator (Research Associate)
Research Identifier:	ORCiD ID: 0000-0003-4822-3353
Nearest person month worked:	8 (Increased from 7 person months in previous annual report).
Contribution to project:	Lead investigator for all specific aims of the project; author on documents detailed in Section 9.
Funding Support:	

Name:	David Higginbotham
Project Role:	Software Developer
Research Identifier:	
Nearest person month worked:	4 (Increased from 2 person months in previous annual report).
Contribution to project:	VCT software development for x-ray projection simulation and breast phantom creation.
Funding Support:	

7.B. Has there been a change in the active other support of the PD/PI(s) or senior / key personnel since the last reporting period?

Since the start of this project, the following grants have concluded and are no longer actively funding key personnel:

IIR13264610 Maidment, Andrew 2/15/2014-2/14/2018
Susan G. Komen $ 201,859
Foundation
Scientific Grants Manager: Amy Dworkin
Next-Generation Digital Breast Tomosynthesis for Superior Calcification Imaging
This grant proposes the construction of a prototype digital breast tomosynthesis (DBT) system with superior spatial resolution for research use. Funding was previously provided to Raymond J. Acciavatti, Emily F. Conant, and Andrew D. A. Maidment.

U54-CA163313-04 Rev Schnall, Mitchell 9/21/2011-5/31/2018
NIH $ 903,517
Program Official: Tonya Parker
Penn Center for Innovation in Personalized Breast Screening
This proposal will advance a personalized breast cancer screening paradigm by developing a new tool (breast complexity index) for predicting individual screening outcomes. Funding was previously provided to Emily F. Conant, Despina Kontos, and Andrew D. A. Maidment.

The most <u>current</u> description of <u>active</u> grant support for all key personnel is included in the pages that follow.

Raymond J. Acciavatti, Ph.D. – Active Grant Support:

W81XWH-18-1-0082 Acciavatti, Raymond 3/15/2018-3/14/2021 7.8 calendar
Department of Defense Breast Cancer Research Program Breakthrough Award (Level 1) $ 125,000
Science Officer: Laurie Shuman-Moss
Design of a 3D Mammography System in the Age of Personalized Medicine.
This grant proposes a personalized acquisition geometry for 3D mammography, as well as additional design changes that offer improvements in super-resolution.

1R01CA207084 Vachon, Celine 4/1/2017-3/31/2022 3.0 calendar
Mayo Clinic (Subcontract) $ 121,394
Program Official: Pamela M. Marcus
Radiomic phenotypes of breast parenchyma and association with breast cancer risk and detection
No overlap. The main goals of this study are to characterize 'intrinsic' parenchymal complexity features reflecting the heterogeneity of breast tissue, to examine the association of 'intrinsic' parenchymal complexity features with breast cancer risk and to examine the contribution of parenchymal complexity features to masking cancers.

R01CA161749 Kontos, Despina 4/1/2017-3/31/2022 0.60 calendar
NIH $ 481,172
Program Official: Houston Baker
Digital breast tomosynthesis imaging biomarkers for breast cancer risk estimation
No overlap. The improved clinical performance achieved with digital breast tomosynthesis is currently fueling a broad adaptation of tomosynthesis for general population breast cancer screening. Our study will be the first to evaluate tomosynthesis imaging measures in breast cancer risk assessment and will develop the necessary technology to enable larger multi-center studies. Ultimately, these novel imaging biomarkers may lead to more accurate individualized risk stratification, improving personalized breast cancer screening and prevention.

IRSA 1016451 Maidment, Andrew 9/1/2016-8/31/2021 0.60 calendar
Burroughs Wellcome Fund $ 100,000
Contact: Rusty Kelley
ViCTRE – Virtual Clinical Trials in the Regulatory Environment.
No overlap. We propose ViCTRE as a cost-effective and timely alternative to the current regulatory process. This vision is not fanciful; the elements of our proposed VCT pipeline are mature. VCTs are already commonly used in the design and development of imaging devices by academia and industry.

OVERLAP: There is no scientific or budgetary overlap between active research grants and DoD grant W81XWH-18-1-0082.

Emily Conant, M.D. – Active Grant Support:

W81XWH-18-1-0082 Acciavatti, Raymond 3/15/2018-3/14/2021 0.12 calendar
Department of Defense Breast Cancer Research Program Breakthrough Award (Level 1) $125,000
Science Officer: Laurie Shuman-Moss
Design of a 3D Mammography System in the Age of Personalized Medicine.
This grant proposes a personalized acquisition geometry for 3D mammography, as well as additional design changes that offer improvements in super-resolution.

Hologic Conant, Emily 11/21/2019-5/31/2020 0.48 calendar
Hologic $121,527
Hologic Case Transfer Agreement
No overlap. The objective of this protocol is IRB-approved case collection for research, development, user training and support further product performance claims for breast imaging modalities and computer-aided detection. The collection will include mammography, tomosynthesis, and computer-generated images, including image meta-data and corresponding medical reports, relevant associated exams and reports which are all de-identified prior to transfer to the Sponsor.

R01CA161749 Kontos, Despina 4/1/2017-3/31/2022 1.20 calendar
NIH $ 370,701
Program Official: Houston Baker
Digital breast tomosynthesis imaging biomarkers for breast cancer risk estimation
No overlap. The improved clinical performance achieved with digital breast tomosynthesis is currently fueling a broad adaptation of tomosynthesis for general population breast cancer screening. Our study will be the first to evaluate tomosynthesis imaging measures in breast cancer risk assessment and will develop the necessary technology to enable larger multi-center studies. Ultimately, these novel imaging biomarkers may lead to more accurate individualized risk stratification, improving personalized breast cancer screening and prevention.

1R01CA207084 (NIH) Vachon, Celine 4/1/2017-3/31/2022 0.48 calendar
Mayo Clinic (Subcontract) $ 140,248
Program Official: Pamela M. Marcus
Radiomic phenotypes of breast parenchyma and association with breast cancer risk and detection
No overlap. The main goals of this study are to characterize 'intrinsic' parenchymal complexity features reflecting the heterogeneity of breast tissue, to examine the association of 'intrinsic' parenchymal complexity features with breast cancer risk and to examine the contribution of parenchymal complexity features to masking cancers.

R01-CA191207 Li, Lin 7/2/2015-6/30/2020 0.12 calendar
NIH $ 388,596
Program Official: Lori A. Henderson
Redox imaging for breast cancer prognosis
No overlap. The objective of this project is to demonstrate that the mitochondrial redox imaging, i.e., fluorescence imaging of endogenous NADH and oxidized flavoproteins (Fp including FAD), has prognostic value in managing breast cancer (BC). Our central hypothesis is that the heterogeneity-associated mitochondrial redox imaging (HAMRI) indices (Fp, NADH and the redox ratios, e.g., Fp/NADH) can predict or add value for predicting BC prognosis.

OVERLAP: There is no scientific or budgetary overlap between active research grants and DoD grant W81XWH-18-1-0082.

Despina Kontos, Ph.D. – Active Grant Support:

W81XWH-18-1-0082 Acciavatti, Raymond 3/15/2018-3/14/2021 0.12 calendar
Department of Defense Breast Cancer Research Program Breakthrough Award (Level 1) $ 125,000
Science Officer: Laurie Shuman-Moss
Design of a 3D Mammography System in the Age of Personalized Medicine.
This grant proposes a personalized acquisition geometry for 3D mammography, as well as additional design changes that offer improvements in super-resolution.

R01-CA161749 Kontos, Despina 4/1/2017-3/31/2022 2.16 calendar
NIH $ 481,172
Program Official: Houston Baker
Digital breast tomosynthesis imaging biomarkers for breast cancer risk estimation
No overlap. The improved clinical performance achieved with digital breast tomosynthesis is currently fueling a broad adaptation of tomosynthesis for general population breast cancer screening. Our study will be the first to evaluate tomosynthesis imaging measures in breast cancer risk assessment and will develop the necessary technology to enable larger multi-center studies. Ultimately, these novel imaging biomarkers may lead to more accurate individualized risk stratification, improving personalized breast cancer screening and prevention.

1R01CA197000-01A1 Kontos, Despina 4/19/2016-3/31/2021 1.92 calendar
NIH $ 267,315
Program Official: Houston Baker
Multi-parametric 4-D Imaging Biomarkers for Neoadjuvant Treatment Response
No overlap. Pattern analysis and machine learning methods are powerful knowledge discovery tools that can be very effective in identifying complex multi-parametric patterns from a diverse set of imaging and non-imaging biomarkers that can best predict treatment response and outcome. Our method will leverage the richness of available data to point to new imaging biomarkers that are better early predictors of response, enabling personalized treatment decisions for women undergoing neoadjuvant chemotherapy for breast cancer.

U24-CA189523-01A1 Davatzikos/Kontos 9/1/2015-8/31/2020 0.72 calendar
NIH $ 408,411
Program Official: George O. Redmond
Cancer imaging phenomics software suite: application to brain and breast cancer
No overlap. This project will develop advanced computer analysis methodology for interpretation of radiologic images of cancer, emphasizing brain and breast cancer. The functionality of the software will substantially transcend limitations of current analysis of cancer images, and will open the way for more precise and effective surgical planning as well as for more specific diagnosis of cancer based on its imaging characteristics, eventually leading to individualized medicine.

1R01CA207084 Vachon, Celine 4/1/2017-3/31/2022 2.76 calendar
Mayo Clinic (Subcontract) $ 124,500
Program Official: Pamela M. Marcus
Radiomic phenotypes of breast parenchyma and association with breast cancer risk and detection
No overlap. The main goals of this study are to characterize ‘intrinsic’ parenchymal complexity features reflecting the heterogeneity of breast tissue, to examine the association of ‘intrinsic’ parenchymal complexity features with breast cancer risk and to examine the contribution of parenchymal complexity features to masking cancers.

1R01CA223816 Kontos/Chodosh 7/3/2018-5/31/2023 1.50 calendar
NIH $ 414,065
Program Official: Houston Baker
Radiogenomic Biomarkers of Breast Cancer Recurrence
No overlap. We propose to analyze imaging features of phenotypic tumor heterogeneity that will provide information to complement histopathologic and molecular markers, enhancing our prognostic ability for breast cancer. Ultimately, integrating imaging with novel molecular tumor markers could enable more informed, precision-medicine, treatment decisions to reduce unnecessary side-effects while improving long-term outcomes for women diagnosed with breast cancer.

UM1CA221939 Ritzwoller/Doubeni 4/15/2018-3/31/2023 0.84 calendar(years 1-3)
NCI $ 2,397,802
Program Official: Priyanga Tuovinen
Center for Research to Optimize Precision Lung Cancer Screening in Diverse Populations
No overlap. The goal of this Center is to build a comprehensive data ecosystem of the entire lung cancer screening process and to assess associated multilevel factors to conduct high impact multilevel studies including interventions to address gaps in care that may lead to lung cancer health disparities in the PROSPR initiative. Role: Project leader (0.72 cal years 4-5).

R33-CA-225310 Mankoff, David 9/1/2017-8/31/2020 1.20 calendar
NIH $ 136,575 TC
Program Official: Yantian Zhang
Area B: Multi-Tracer Volumetric PET (MTV-PET) to Measure Tumor Glutamine and Glucose Metabolic Rates in a Single Imaging Session
No overlap. We will take advantage of recent developments in volumetric positron emission tomography (PET) scanners, fast reconstruction, and 4D image analysis to develop methods for multi-tracer PET with the goal of generating quantitative, multi-parametric whole-body images of specific aspects of cancer biology, including cancer metabolism as the focus of our proposed technology development projects. Successful completion of our proposed technology development will yield a clinically practical method for multi-tracer PET that would provide multi-valent, whole-body molecular parametric images that would change the landscape for cancer imaging diagnostic biomarkers and precision oncology.

OVERLAP: There is no scientific or budgetary overlap between active research grants and DoD grant W81XWH-18-1-0082.

Andrew Maidment, Ph.D. – Active Grant Support:

W81XWH-18-1-0082 Acciavatti, Raymond 3/15/2018-3/14/2021 0.24 calendar
Department of Defense Breast Cancer Research Program Breakthrough Award (Level 1) $ 125,000
Science Officer: Laurie Shuman-Moss
Design of a 3D Mammography System in the Age of Personalized Medicine.
This grant proposes a personalized acquisition geometry for 3D mammography, as well as additional design changes that offer improvements in super-resolution.

R01EB018958 Eckstein, Miguel 8/15/2015-5/31/2020 0.50 calendar
University of California, Santa Barbara (UCSB)/NIH $ 69,131
Program Official: Behrouz Shabestari
Assessment of Medical Image Quality with Foveated Search Models
No overlap. To develop a novel method for the assessment of image quality in 2D and 3D clinical x-ray breast images using foveated search observer models, developed at UCSB.

R01CA227142 Cormode, David 5/1/2018-4/30/2023 1.20 calendar
NIH $ 361,282
Program Official: Peter Ogunbiyi
Nanoparticle contrast agents for earlier breast cancer detection.
No overlap. The objective of this project is to develop polyphosphazene nanoparticles containing silver alloy contrast agents to enhance the efficacy of dual energy mammography for tumor detection.

R01CA161749 Kontos, Despina 4/1/2017-3/31/2022 0.60 calendar
NIH $ 370,701
Program Official: Houston Baker
Digital breast tomosynthesis imaging biomarkers for breast cancer risk estimation
No overlap. The improved clinical performance achieved with digital breast tomosynthesis is currently fueling a broad adaptation of tomosynthesis for general population breast cancer screening. Our study will be the first to evaluate tomosynthesis imaging measures in breast cancer risk assessment and will develop the necessary technology to enable larger multi-center studies. Ultimately, these novel imaging biomarkers may lead to more accurate individualized risk stratification, improving personalized breast cancer screening and prevention.

IRSA 1016451 Maidment, Andrew 9/1/2016-8/31/2021 1.20 calendar
Burroughs Wellcome Fund $ 100,000
Contact: Rusty Kelley
ViCTRE – Virtual Clinical Trials in the Regulatory Environment.
No overlap. We propose ViCTRE as a cost-effective and timely alternative to the current regulatory process. This vision is not fanciful; the elements of our proposed VCT pipeline are mature. VCTs are already commonly used in the design and development of imaging devices by academia and industry.

R01-CA196528-01A1 Surti, Suleman 4/1/2016-3/31/2021 1.20 calendar
NIH $ 361,505
Program Official: Houston Baker
High Performance, Quantitative Breast PET Scanner Integrated with Tomosynthesis
No overlap. A dedicated breast PET-DBT scanner provides higher resolution and sensitivity compared to a wholebody PET/CT scanner, and hence quantitative images from such a device can play a significant role in providing personalized therapy for patients diagnosed with breast cancer. In this project we develop such a device in an integrated multi-modality design, and subsequently evaluate its clinical performance in patients for ER+ tumor characterization and diagnostic imaging of patients with dense breasts.

OVERLAP: There is no scientific or budgetary overlap between active research grants and DoD grant W81XWH-18-1-0082.

7.C. What other organizations were involved as partners?
Nothing to report.

8. SPECIAL REPORTING REQUIREMENTS.

8.A. Collaborative Awards
Nothing to report.

8.B. Quad Charts
Nothing to report.

REFERENCES

1. Friedewald SM, Rafferty EA, Rose SL, et al. Breast Cancer Screening Using Tomosynthesis in Combination With Digital Mammography. *Journal of the American Medical Association.* 2014;311(24):2499-2507.
2. Sechopoulos I. A review of breast tomosynthesis. Part I. The image acquisition process. *Medical Physics.* 2013;40(1):014301-014301 to 014301-014312.
3. Sechopoulos I. A review of breast tomosynthesis. Part II. Image reconstruction, processing and analysis, and advanced applications. *Medical Physics.* 2013;40(1):014302-014301 to 014302-014317.
4. Rafferty EA, Park JM, Philpotts LE, et al. Assessing Radiologist Performance Using Combined Digital Mammography and Breast Tomosynthesis Compared with Digital Mammography Alone: Results of a Multicenter, Multireader Trial. *Radiology.* 2013;266(1):104-113.
5. Lanyi M. Chapter 7: Differential Diagnosis of Microcalcifications. *Diagnosis and Differential Diagnosis of Breast Calcifications*. Berlin: Springer-Verlag; 1988:193-231.
6. Acciavatti RJ, Maidment ADA. Observation of super-resolution in digital breast tomosynthesis. *Medical Physics.* 2012;39(12):7518-7539.
7. Bakic PR, Barufaldi B, Higginbotham D, et al. Virtual Clinical Trial of Lesion Detection in Digital Mammography and Digital Breast Tomosynthesis. Paper presented at: SPIE Medical Imaging2018; Houston, TX.
8. Pokrajac DD, Maidment ADA, Bakic PR. Optimized generation of high resolution breast anthropomorphic software phantoms. *Medical Physics.* 2012;39(4):2290-2302.
9. Acciavatti RJ, Barufaldi B, Vent TL, Wileyto EP, Maidment ADA. Personalization of X-Ray Tube Motion in Digital Breast Tomosynthesis Using Virtual Defrise Phantoms. Paper presented at: SPIE Medical Imaging2019; San Diego, CA.
10. Barufaldi B, Higginbotham D, Bakic PR, Maidment ADA. OpenVCT: A GPU-Accelerated Virtual Clinical Trial Pipeline for Mammography and Digital Breast Tomosynthesis. Paper presented at: SPIE Medical Imaging2018; Houston, TX.
11. Acciavatti RJ, Noël PB, Maidment ADA. Proposing Rapid Source Pulsing for Improved Super-Resolution in Digital Breast Tomosynthesis. Paper presented at: SPIE Medical Imaging2020 (accepted); Houston, TX.
12. Acciavatti RJ, Wileyto EP, Maidment ADA. Modeling Acquisition Geometries with Improved Super-Resolution in Digital Breast Tomosynthesis. Paper presented at: SPIE Medical Imaging2016; San Diego, CA.
13. Acciavatti RJ, Maidment ADA. Proposing an Acquisition Geometry That Optimizes Super-Resolution in Digital Breast Tomosynthesis. *Lecture Notes in Computer Science.* 2012;7361:386-393.
14. Bakic PR, Ng S, Ringer P, Carton A-K, Conant EF, Maidment ADA. Validation and Optimization of Digital Breast Tomosynthesis Reconstruction using an Anthropomorphic Software Breast Phantom. Paper presented at: SPIE Medical Imaging2010; San Diego, CA.
15. Barufaldi B, Vent TL, Acciavatti RJ, et al. Determining the Optimal Angular Range of the X-Ray Source Motion in Tomosynthesis Using Virtual Clinical Trials. Paper presented at: SPIE Medical Imaging2020 (accepted); Houston, TX.

9. APPENDICES

1. Acciavatti RJ, Barufaldi B, Vent TL, Wileyto EP, Maidment ADA. Personalized Scanning Motions for Suppressing the Cone-Beam Artifact in Digital Breast Tomosynthesis. This paper is being prepared for submission to a journal (28 pages).
2. Vent TL, Acciavatti RJ, Maidment ADA. Development and Evaluation of a Spatial Resolution Metric for Digital Breast Tomosynthesis. This paper expands upon work presented in last year's progress report, and is being prepared for submission to a journal (9 pages).
3. Acciavatti RJ, Vent TL, Barufaldi B, Wileyto EP, Noël PB, Maidment ADA. Proposing Rapid Source Pulsing for Improved Super-Resolution in Digital Breast Tomosynthesis. In: Chen G-H, Bosmans H, editors; Physics of Medical Imaging; 2020; Houston, TX: SPIE; 2020. p. 113125G. The PI (Raymond Acciavatti) presented this work as a poster at the SPIE Medical Imaging conference on 2/17/2020 in Houston, TX (9 pages).
4. Acciavatti RJ, Cohen EA, Maghsoudi OH, Gastounioti A, Pantalone L, Hsieh M-K, Conant EF, Scott CG, Winham SJ, Kerlikowske K, Vachon C, Maidment ADA, Kontos D. Robust Radiomic Feature Selection in Digital Mammography: Understanding the Effect of Imaging Acquisition Physics Using Phantom and Clinical Data Analysis. In: Hahn HK, Mazurowski MA, editors; Computer-Aided Diagnosis; 2020; Houston, TX: SPIE; 2020. p. 113140W. The PI (Raymond Acciavatti) gave an oral presentation at the SPIE Medical Imaging conference on 2/17/2020 in Houston, TX (9 pages).
5. Barufaldi B, Vent TL, Acciavatti RJ, Bakic PR, Noël PB, Conant EF, Maidment ADA. Determining the Optimal Angular Range of the X-Ray Source Motion in Tomosynthesis Using Virtual Clinical Trials. In: Chen G-H, Bosmans H, editors; Physics of Medical Imaging; 2020; Houston, TX: SPIE; 2020. p. 113120I (7 pages).
6. Acciavatti RJ, Cohen EA, Maghsoudi OH, Gastounioti A, Pantalone L, Hsieh M-K, Barufaldi B, Bakic PR, Chen J, Conant EF, Kontos D, Maidment ADA. Calculation of Radiomic Features to Validate the Textural Realism of Physical Anthropomorphic Phantoms for Digital Mammography. This work was accepted by the IWBI conference; it is projected that this conference will be held virtually in May 2020 (7 pages).
7. Acciavatti RJ, Vent TL, Barufaldi B, Wileyto EP, Noël PB, Maidment ADA. Super-Resolution in Digital Breast Tomosynthesis: Limitations of the Conventional System Design and Strategies for Optimization. This work was accepted by the IWBI conference; it is projected that this conference will be held virtually in May 2020 (9 pages).
8. Barufaldi B, Vent TL, Acciavatti RJ, Bakic PR, Noël PB, Maidment ADA. MRMC ROC Analysis of Calcification Detection in Tomosynthesis Using Computed Super-Resolution and Virtual Clinical Trials. This work was accepted by the IWBI conference; it is projected that this conference will be held virtually in May 2020 (5 pages).
9. Vent TL, Barufaldi B, Acciavatti RJ, Maidment ADA. Simulation of High-Resolution Test Objects using Non-Isocentric Acquisition Geometries in Next-Generation Digital Tomosynthesis. This work was accepted by the IWBI conference; it is projected that this conference will be held virtually in May 2020 (5 pages).
10. Vu B-T, Barufaldi B, Vent T, Acciavatti R, Maidment A. Automation of Virtual Clinical Trials Used to Evaluate Efficacy of Breast Cancer Screening Modalities. The PI (Raymond Acciavatti) mentored an undergraduate student (Brian Vu, Univ. of Houston) in 2019 through the AAPM summer undergraduate fellowship program. During that summer, Brian also participated in the Summer Undergraduate Program for Educating Radiation Scientists (SUPERS), for which he prepared an abstract and gave a presentation on 8/7/2019 (1 page).
11. Award Chart summarizing progress made in Years 1 and 2 of the grant (1 page).

Personalized Scanning Motions for Suppressing the Cone-Beam Artifact in Digital Breast Tomosynthesis

Raymond J. Acciavatti, Bruno Barufaldi, Trevor L. Vent, E. Paul Wileyto,

and Andrew D. A. Maidment

ABSTRACT (300 Words)

In the conventional design for digital breast tomosynthesis (DBT) systems, the source moves in only one direction (laterally). This yields a cone-beam artifact distal to the plane of source motion. This artifact can be visualized with a Defrise phantom. Our previous work demonstrated that image quality is improved by introducing source motion in the posteroanterior (PA) direction. However, to date we have not analyzed how to optimize the range of PA motion. The purpose of this paper is to demonstrate the benefit of personalizing the range of motion around the dimensions of the object. To this end, virtual Defrise phantoms were created in the shape of breasts under compression. Their internal structure consisted of fibroglandular and adipose tissue arranged in a square wave. Each phantom was analyzed in 441 acquisition geometries, corresponding to 21 ranges of source motion laterally and 21 ranges of source motion posteroanteriorly. A scout image was also simulated, allowing for estimation of the phantom dimensions. To analyze the reconstructions, a signal-intensity threshold was introduced to classify each voxel as either fibroglandular or adipose tissue. We generated a receiver operating characteristic (ROC) curve based on the percentage of true and false classifications of fibroglandular tissue at each threshold. Area under the ROC curve (AUC) was the figure-of-merit used to evaluate each acquisition geometry. We showed that the cone-beam artifact can be simulated in a conventional acquisition geometry. Based on the AUC results, the optimum acquisition geometry was then identified for each phantom. The optimum range of source motion was found to vary based on the size of the phantom in the PA direction. In larger phantoms, it was necessary to translate the source further

from the chest-wall plane to optimize the image quality. In summary, this paper demonstrates the benefit of personalized acquisition geometries in DBT.

Index Terms: Virtual clinical trials, digital breast tomosynthesis, Defrise phantom, cone-beam artifact, receiver operating characteristic curve, image quality.

DISCLOSURE OF CONFLICTS OF INTEREST

Andrew D. A. Maidment is a scientific advisor to Real Time Tomography (RTT), and his spouse is an employee and shareholder of RTT.

I. INTRODUCTION

In cone-beam computed tomography (CBCT), the cone-beam artifact can be visualized with a Defrise phantom.[1] Our previous work demonstrated the existence of a similar artifact in digital breast tomosynthesis (DBT).[2-4] We built a Defrise phantom by laser-cutting rectangular plastic plates, which were spaced in the direction perpendicular to the source motion; *i.e.*, the posteroanterior (PA) direction. In this direction, the rays must traverse multiple plates before reaching the detector, and hence the contrast between the plastic-air separations is degraded.

We later constructed a prototype "next-generation" tomosynthesis (NGT) system to analyze how image quality in DBT can be improved.[5, 6] The NGT system is capable of source motion with an additional degree of freedom in the PA direction, unlike a clinical DBT system. Since there are rays normal to the plastic-air separations in the Defrise phantom, we showed that the cone-beam artifact is suppressed with the use of PA source motion.

The source motion in the NGT system can be understood in parallel with similar design strategies used in CBCT. For example, in a work on optimizing CBCT reconstruction algorithms,

Tang *et al*. investigated a scanning motion combining a conventional circular orbit with two additional arcs in the perpendicular direction, and demonstrated improvements in the visualization of a Disc phantom.[7] More recently, Becker *et al*. showed that the cone-beam artifact in dedicated breast CT can be suppressed by the use of a multi-source array.[8] In that work and a follow-up study by Boone *et al*.[9], they analyzed an acquisition geometry with up to five circular orbits, each spaced in 2.0 cm increments. They demonstrated that the use of a multi-source array broadens the field-of-view over which all the interfaces in a Defrise phantom are visible to within detectable limits. Regardless of whether a single- or multi-source geometry is used, these CBCT system designs are similar to the NGT system in that acquisition poses are introduced in the direction perpendicular to the conventional scanning motion.

In addition to PA source motion, we are investigating how the acquisition geometry in DBT can be customized around the object and the imaging task. This idea can also be understood in parallel with CBCT, as described for example by Fischer *et al*.[10] In that work, they simulated many projection views of industrial objects based on CAD-drawings, and identified the views that maximize the detectability index for two tasks: detecting a welded joint in a steel structure and imaging the six faces of an aluminum cube with drilled holes. They showed that reconstruction artifacts in acquisitions with circular or helical motion (for example, translucency artifacts in the steel structure) were mitigated with the use of a customized scanning motion. The gain in image quality was achieved with even fewer projection views than a conventional scan.

Previous work also explored how customized scanning motions can be applied to image-guided therapy.[11, 12] Capostagno *et al*. demonstrated that in interventional neuroradiology, there are photon starvation artifacts surrounding an embolization coil used to treat an aneurysm, and that these artifacts obscure the visualization of adjacent lesions, such as low-contrast hemorrhages.[12]

They simulated the presence of these lesions in a phantom model and demonstrated that the detectability index for this task can be optimized with the use of a customized scanning motion.

In this paper, the idea of deriving customized scanning motions from virtual objects is applied to DBT. To this end, we simulate virtual Defrise phantoms modeled in the shape of breasts under compression.[13] The phantoms are given internal structure consisting of two tissue types (fibroglandular and adipose) arranged in a square wave. Unlike the CBCT studies, the task in this paper is not to improve the visualization of specific details, but instead to optimize the acquisition in such a way that the cone-beam artifact is suppressed uniformly throughout the 3D image.

Since there are no specific locations at which image quality is being optimized, it is not possible to define a detectability index and hence to identify the projection views that optimize this index. For this reason, we apply a different metric of image quality than the one used in the CBCT studies. This metric was proposed by Bakic *et al*., who quantified how well fibroglandular and adipose tissue are portrayed in phantoms.[14] Each voxel in the reconstruction is classified as either fibroglandular or adipose tissue based on a signal-intensity threshold, and these classifications are compared against the known ground truth. The percentage of true and false classifications are analyzed in terms of a receiver operating characteristic (ROC) curve by varying the signal intensity used to threshold the two tissue types.

Area under the ROC curve (AUC) is the figure-of-merit used to identify the best scanning motion. To maximize AUC, we show that the scanning motion needs to be customized around the dimensions of the phantom. Since the dimensions of the object are not known *a priori* in a clinical screening exam, we also investigate whether the scanning motion can be customized around the dimensions obtained from a 2D scout image.

II. METHODS

A. Phantom Creation

Breast outlines were simulated using the model of Rodríguez-Ruiz *et al*.[13] In that work, MATLAB® software was developed in which the user can specify the phantom thickness, and generate random outlines varying in terms of chest wall-to-nipple distance (CND). We selected the option for "advanced 3D curvature".

The thicknesses supported by this model range from 35 to 85 mm. We varied thickness between these bounds in 10 mm steps. Five random phantoms were created at each thickness. Thus a total of 30 breast outlines were generated; the mean CND was 10.9 cm and the standard deviation was 2.9 cm.

The phantoms then underwent additional processing in MATLAB®. As described in previous work, some slices at the superior surface were truncated, since the shape of the phantom was not representative of a breast under compression.[15] Additionally, the 3D phantom, which was initially created with 1.0 mm^3 voxels, was up-sampled to 0.50 mm^3 voxels.

Next, the phantoms were given internal structure consisting of fibroglandular and adipose tissue arranged in a Defrise pattern. As shown in Figure 1, the square wave can be oriented posteroanteriorly (top row) or laterally (bottom row). Also, two frequencies were analyzed: 0.17 mm^{-1} and 0.083 mm^{-1}. By varying the orientation and frequency of the square wave for all 30 phantom outlines, a total of 120 phantoms were created for this study.

B. Acquisition Poses

Figure 2 shows the motion of the source in a plane. Unlike a conventional DBT system which supports only lateral source motion (x), the NGT system supports motion in two directions (x and y); for example, a half ellipse (Figure 2).

For the purpose of these simulations, the acquisition poses were arranged in 30° increments around two half ellipses, with the midpoint of each ellipse (*i.e.*, the midpoint of the chest wall) corresponding to an additional acquisition pose. The semi-axis lengths for the outer ellipse were defined to be a and b in the x and y directions, respectively. The corresponding lengths for the inner ellipse were one-half of these values.

We varied parameter a between 50.0 and 150.0 mm in 5.0 mm increments (or 21 steps), and parameter b between 0 and 200.0 mm in 10.0 mm increments (also 21 steps). In the special case $b = 0$, source motion was modeled in only one direction (x), with uniform spacing between the acquisition poses (plot not shown). In summary, there were 441 acquisition geometries simulated for each phantom.

C. Imaging Simulation

We used the automatic exposure control table from the work of Feng and Sechopoulos to calculate the technique settings for a DBT system with a W/Al target filter combination.[16] First, kV was determined from the phantom thickness by linearly interpolating the values in the table. This result was rounded to the nearest integer. The mAs for phantoms with 50% glandular fraction was then calculated based on the kV (also by linearly interpolating the values in the table).

All other acquisition parameters were consistent with those used in the NGT system.[5, 6, 15, 17, 18] In all projection views, the source-to-image distance was 652.0 mm. The breast support was 31.0 mm above the detector. The AXS-2430 detector (Analogic Canada Corporation, Montreal, Quebec, Canada) with 0.085 mm pixelation was simulated.

X-ray projection images were calculated with ray tracing software developed for virtual clinical trials. Reconstructions were calculated in Briona™ (Real Time Tomography, LLC, Villanova, PA) with a 0.085 mm in-plane resolution and a slice thickness of 0.50 mm.

Subsequently, the in-plane resolution was down-scaled to 0.50 mm using bicubic interpolation, so the voxels in the reconstruction were matched one-to-one with the input phantom.

D. Metric of Image Quality

We applied the method of Bakic *et al*. to quantify how well the two tissue types were separated from each other in the reconstruction.[14] Signal intensities were analyzed separately in each tissue type, using the input phantom to identify the true fibroglandular and true adipose voxels. Examples of histograms derived from signal in each tissue type are shown in Figure 3(a). These examples are generated from one phantom (0.083 mm^{-1}, PA orientation) with a CND of 12 cm under acquisition settings consistent with a conventional acquisition geometry (a = 100.0 mm, b = 0). The histograms were Z-score normalized with the transformation

$$Z = \frac{I - \frac{\mu_F + \mu_A}{2}}{\sqrt{\frac{\sigma_F^2 + \sigma_A^2}{2}}}, \quad (1)$$

where the subscripts F and A denote fibroglandular and adipose tissue, respectively, and μ and σ denote the mean and standard deviation of signal intensity (I) in each tissue type. With this transformation, the origin is shifted halfway between μ_F and μ_A. Also, the signal intensity is normalized by the pooled standard deviation. The histograms in Figure 3(a) are truncated to within ± two units of the pooled standard deviation.

Next, a signal-intensity threshold was introduced to classify voxels as either fibroglandular or adipose tissue. At each threshold, we calculated the percentage of true and false fibroglandular classifications. A ROC curve was generated by varying the threshold. An example of a ROC curve is shown in Figure 3(b). This example was generated from the histograms in Figure 3(a). AUC was

in turn calculated as a figure-of-merit using the trapezoidal method; AUC is a measure of how well the two histograms in Figure 3(a) are separated from each other.

In summary, 52,920 reconstructions (441 acquisitions multiplied by 120 phantoms) were analyzed with these methods. The total run time of these simulations (including projecting, reconstructing, and calculating AUC) was 4 GPU-months.

E. Scout Image for Estimating Phantom Dimensions

Out of 441 acquisition geometries, the one with the highest AUC was identified for each phantom. We investigated whether there was a relationship between the optimum acquisition parameters and the physical dimensions of the phantom. These dimensions can be estimated from a scout image; for example, the image obtained with the acquisition pose used in 2D digital mammography (the center of each half ellipse in Figure 2). Figure 4(a) shows an example of a scout image for the phantom described previously.

The histogram derived from the scout image can be used to segment the phantom from the background (Figure 5). Previous work described how the threshold for segmentation can be determined iteratively with the midpoint method.[19] For the purpose of this paper, the median signal was used as the first iterate. We continued iterating until the difference between iterates converged to zero. The masks for all 120 phantoms were checked to ensure they passed a visual inspection. An example of a mask is shown in Figure 4(b).

III. RESULTS

A. Conventional Acquisition Geometry

First, to illustrate the conventional acquisition geometry, reconstructions of the phantom described previously are shown in Figure 6. The acquisition parameters were: a = 100.0 mm and

$b = 0$. The central slice of the reconstruction, corresponding to the mid-thickness of the phantom, is shown.

These reconstructions illustrate how the image quality varies based on the orientation of the Defrise pattern. All the interfaces between fibroglandular and adipose tissue can be visualized clearly if frequency is oriented laterally [Fig. 6(a), (c)]. However, some interfaces are blurred if frequency is oriented posteroanteriorly [Fig. 6(b), (d)]. As frequency increases, the cone-beam artifact comes into existence more proximal to the chest wall, and hence there is a narrower range of positions in the PA direction over which the interfaces are all distinguishable [Fig. 6(d)]. These results are consistent with our previous work studying the effect of orientation and frequency in physical experiments in the conventional acquisition geometry.[2, 3]

B. Effect of Varying the Acquisition Geometry

Using the same phantom, AUC is plotted as a function of the acquisition parameters *a* and *b* in Figure 7. As shown, the range of AUC variation differs between the two orientations (lateral and PA). The AUC is less sensitive to the acquisition geometry if frequency is oriented laterally.

While we do not show surface plots for all 120 phantoms, we calculated the total range of AUC variation to summarize the results. This summary metric (denoted ΔAUC) is the difference between the maximum and minimum AUC values across all acquisition geometries; it is a measure of how much image quality is sensitive to variation in the acquisition parameters. The ΔAUC results, grouped based on the orientation and frequency of the Defrise pattern, are shown in Figure 8 with boxplots.

We applied a paired, one-sided *t*-test to demonstrate that the two orientations (lateral and PA) are characterized by statistically-different ΔAUC results at the 0.05 level of significance. Test

statistics (t_{29}) were calculated under 29 degrees of freedom. For low- and high- frequency phantoms, t_{29} was -4.46 ($p = 0.0001$) and -8.98 ($p < 0.0001$), respectively.

In summary, optimization of the scanning parameters is not as critical if frequency is oriented laterally, since image quality is not as sensitive to the acquisition geometry. For this reason, in identifying the optimum scanning parameters in the next section, we choose to focus only on the PA orientation of the input frequency.

C. Calculation of the Optimum Scanning Motion

In this section, we now shift our focus to the PA orientation of the input frequency. It can be seen from the results obtained from one phantom [Fig. 7(b), 7(d)] that AUC is effectively insensitive to variations in parameter *a*. This parameter controls the range of source motion laterally, which in this example is orthogonal to the input frequency. To show that this result can be generalized to all the phantoms, we created boxplots of ΔAUC under variations in parameters *a* and *b* separately, holding the other parameter constant. The boxplots in Figure 9 prove that AUC is affected minimally by parameter *a* and much more strongly by parameter *b*.

Based on the observation that AUC is effectively insensitive to parameter *a*, the optimum source motion was calculated under variation in parameter *b* only (the PA-motion parameter). This calculation was done at a fixed value of *a* (100.0 mm, an intermediate range laterally). Figure 10 demonstrates that there is a relationship between the optimum value of *b* and the size of the phantom; specifically, the maximum PA distance measured relative to the chest wall in the scout image (denoted y_s in Figure 4).

In the low-frequency phantom, the relationship between y_s and the optimum value of *b* is well-described by a linear fit with $R^2 = 0.853$. However, at high frequency, the relationship is not as well-described by a linear fit ($R^2 = 0.476$, plot not shown), but by a power-law fit ($R^2 = 0.6480$).

These trend lines demonstrate that, as the phantom increase in size, the source needs to have a broader range of PA motion to optimize the image quality.

Overall, AUC was optimized by higher values of b (broader PA motion) in the low-frequency phantom than in the high-frequency phantom. Under a paired, one-sided t-test, this result was found to be statistically significant at the 0.05 level ($t_{29} = -3.39$, $p = 0.001$). This finding suggests that the task of optimizing the scanning parameters is dependent on the internal composition of the object. This idea is explored in more detail in the Discussion section.

D. Variation in Image Quality Across Phantoms

Next, we performed an analysis of how AUC varies with the size of the phantom. For these calculations, we continued to assume that $a = 100.0$ mm and that frequency is oriented in the PA direction. As can be seen from the results in Figures 11-12, small phantoms intrinsically have higher AUC. In a phantom with a CND of 7.1 cm shown as an example in Figure 12(a)-(d), the cone-beam artifact is effectively absent in the conventional geometry ($b = 0$). The image quality is not readily different from the optimum geometry ($b = 60$ mm). For this reason, optimization of the acquisition parameters is not as critical in smaller phantoms.

In larger phantoms, by contrast, there is a prominent cone-beam artifact. This idea is illustrated in Figure 12(e) and (g) in a phantom with a CND of 16 cm in the conventional geometry. The gain in AUC achieved by optimizing the geometry is substantial (AUC differences of 0.093 and 0.12 for low- and high-frequency phantoms, respectively, relative to the conventional geometry). With the use of PA source motion, every interface between fibroglandular and adipose tissue can be visualized properly.

It can also be understood from Figures 11-12 that image quality is dependent on the size of the phantom. There is inherently poorer image quality in larger phantoms, and we offer proof of

this trend with linear fitting (Figure 11). This trend holds even if the acquisition geometry is optimized to maximize AUC.

IV. DISCUSSION AND CONCLUSIONS

In a clinical DBT system, there is no source motion in the PA direction, and this gives rise to a cone-beam artifact distal to the chest-wall plane. The Defrise phantom is a test object for visualizing this artifact. The phantom was simulated using a model of two tissue types (fibroglandular and adipose), and the reconstruction was analyzed voxel-by-voxel as a binary classification task with a ROC curve.[14]

Although two orientations of the input frequency were considered, we showed that the PA orientation is more sensitive to variations in the acquisition geometry, and that the PA motion of the source (parameter b) can be optimized in this orientation. To maximize image quality, the motion of the source needs to be customized around the dimensions of the phantom. There should be broader source motion in the PA direction for phantoms with larger CND (distance y_s as measured in the chest wall-to-nipple direction).

We also studied the effect of altering the spacing between the two tissue types, a surrogate for varying the complexity of the internal composition of the object. Two frequencies were analyzed as examples to illustrate this idea. Comparing the results at each frequency pair-wise, there was a statistically-significant difference in the optimum scanning parameters, and this suggests that the task of optimizing the acquisition geometry is sensitive to the internal composition of the object. In future work, the task of optimizing the separation between fibroglandular and adipose tissue should be evaluated in anthropomorphic phantoms with more realistic parenchymal distributions and broader variability in terms of the complexity of these patterns.[20-22]

This paper demonstrates that there is a relationship between the optimum scanning motion and the distance y_s from the chest wall to the nipple. Future work also needs to explore whether the optimum scanning motion is related to additional features in the scout image, such as other measures of size and shape, as well as the complexity of the internal composition.

Future work should also investigate whether there is a benefit to customizing the reconstruction filter around the object and imaging task. The filtering used in this paper was the same for all acquisitions. In Figure 3(b), the ROC curve bends toward the chance line reading the graph from left-to-right; filtering needs to be explored as a means of optimizing the shape of the ROC curve.

In our early work on the NGT system, we initially proposed the idea of PA source motion as a way to suppress the cone-beam artifact.[2-4] However, our recent work demonstrated that there are other benefits to this motion, such as improving high-frequency resolution.[23, 24] With theoretical modeling, we quantified how resolution varies across the detector area due to anisotropies in the angle of x-ray incidence, and showed that the use of PA source motion helps to minimize these anisotropies.

A disadvantage of PA source motion is that it increases the path length of the x-ray tube orbit and hence scan time, potentially increasing the likelihood of blurring due to patient motion.[25-28] Another trade-off of PA source motion is some loss of tissue coverage at the chest wall. For example, based on a formula derived in our previous work[2], it can be shown that in a slice 25.0 mm above the breast support in the NGT system, there is 8.6 mm of missed tissue anterior to the chest wall, assuming 100.0 mm of PA source motion.

This paper demonstrates that the Defrise phantom is a tool for optimizing the PA motion of the source, but it has limited value in terms of optimizing the lateral motion (parameter a). Optimization of the lateral motion requires an analysis of a different imaging task. For example,

previous work showed that calcification imaging is optimized by a narrow range of source motion laterally. The task of customizing the acquisition geometry around the detection and characterization of lesions should be explored in future work.

The major advantage of virtual clinical trials (VCTs) is that numerous DBT acquisitions (52,920 in total in this paper) can be evaluated in a timely and cost-effective manner. VCTs are computational tools that can help guide the design of imaging systems, limiting the number of physical experiments needed to demonstrate the benefit of a new system design.

ACKNOWLEDGEMENTS

Support was provided by the following grants: W81XWH-18-1-0082 from the Department of Defense Breast Cancer Research Program, IRSA 1016451 from the Burroughs Wellcome Fund, 1R01CA196528 from the National Institute of Health, and IIR13264610 from Susan G. Komen®. In addition, equipment support was provided by Analogic Inc., Barco NV, and Real Time Tomography (RTT). The content is solely the responsibility of the authors and does not necessarily represent the official views of the funding agencies. The authors thank Margaret Nolan, Elizabeth Kobe, Sushmitha Yarrabothula, and Lucy Chai for their early work in developing customized scanning motions in tomosynthesis. We also acknowledge Johnny Kuo, Susan Ng, and Peter Ringer of RTT for providing technical assistance with Briona™.

REFERENCES

[1] Hsieh J. Chapter 10: Multislice and Cone-beam CT. Computed Tomography: Principles, Design, Artifacts, and Recent Advances. Third ed. Bellingham, WA: SPIE Press; 2015. p. 423-86.
[2] Acciavatti RJ, Chang A, Woodbridge L, Maidment ADA, editors. Optimizing the Acquisition Geometry for Digital Breast Tomosynthesis Using the Defrise Phantom. SPIE Medical Imaging; 2014; San Diego, CA: SPIE.
[3] Acciavatti RJ, Mannherz W, Nolan M, Maidment ADA, editors. An Alternate Design for the Defrise Phantom To Quantify Resolution in Digital Breast Tomosynthesis. SPIE Medical Imaging; 2017; Orlando, FL: SPIE.

[4] Acciavatti RJ, Barufaldi B, Vent TL, Wileyto EP, Maidment ADA, editors. Personalization of X-Ray Tube Motion in Digital Breast Tomosynthesis Using Virtual Defrise Phantoms. SPIE Medical Imaging; 2019; San Diego, CA: SPIE.
[5] Maidment TD, Vent TL, Ferris WS, Wurtele DE, Acciavatti RJ, Maidment ADA, editors. Comparing the Imaging Performance of Computed Super Resolution and Magnification Tomosynthesis. SPIE Medical Imaging; 2017; Orlando, FL: SPIE.
[6] Eben JE, Vent TL, Choi CJ, Yarrabothula S, Chai L, Nolan M, et al., editors. Development of a Next Generation Tomosynthesis System. SPIE Medical Imaging; 2018; Houston, TX: SPIE.
[7] Tang X, Ning R. A cone beam filtered backprojection (CB-FBP) reconstruction algorithm for a circle-plus-two-arc orbit. Medical Physics. 2001;28(6):1042-55.
[8] Becker AE, Hernandez AM, Schwoebel P, Boone JM, editors. Multisource x-ray system for artifact reduction in dedicated breast CT. 14th International Workshop on Breast Imaging (IWBI 2018); 2018; Atlanta, GA: SPIE.
[9] Boone JM, Becker AE, Hernandez AM, James T. Dobbins I, Schwoebel P, editors. Multi-x-ray source array for stationary tomosynthesis or multi-cone angle cone beam CT. SPIE Medical Imaging; 2019; San Diego, CA: SPIE.
[10] Fischer A, Lasser T, Schrapp M, Stephan J, Noel PB. Object Specific Trajectory Optimization for Industrial X-ray Computed Tomography. Scientific Reports. 2016;6:1-9.
[11] Stayman JW, Capostagno S, Gang GJ, Siewerdsen JH. Task-driven source-detector trajectories in cone-beam computed tomography: I. Theory and methods. Journal of Medical Imaging. 2019;6(2):025002-1 - -13.
[12] Capostagno S, Stayman JW, Jacobson M, Ehtiati T, Weiss CR, Siewerdsen JH. Task-driven source-detector trajectories in cone-beam computed tomography: II. Application to neuroradiology. Journal of Medical Imaging. 2019;6(2):025004-1 - -11.
[13] Rodriguez-Ruiz A, Agasthya GA, Sechopoulos I. The compressed breast during mammography and breast tomosynthesis: in vivo shape characterization and modeling. Physics in Medicine and Biology. 2017;62:6920-37.
[14] Bakic PR, Ng S, Ringer P, Carton A-K, Conant EF, Maidment ADA, editors. Validation and Optimization of Digital Breast Tomosynthesis Reconstruction using an Anthropomorphic Software Breast Phantom. SPIE Medical Imaging; 2010; San Diego, CA: SPIE.
[15] Acciavatti RJ, Rodriguez-Ruiz A, Vent TL, Bakic PR, Reiser I, Sechopoulos I, et al., editors. Analysis of Volume Overestimation Artifacts in the Breast Outline Segmentation in Tomosynthesis. SPIE Medical Imaging; 2018; Houston, TX: SPIE.
[16] Feng SSJ, Sechopoulos I. Clinical Digital Breast Tomosynthesis System: Dosimetric Characterization. Radiology. 2012;263(1):35-42.
[17] Ferris WS, Vent TL, Maidment TD, Acciavatti RJ, Wurtele DE, Maidment ADA, editors. Geometric Calibration for a Next-Generation Digital Breast Tomosynthesis System. SPIE Medical Imaging; 2017; Orlando, FL: SPIE.
[18] Choi CJ, Vent TL, Acciavatti RJ, Maidment ADA, editors. Geometric Calibration for a Next-Generation Digital Breast Tomosynthesis System Using Virtual Line Segments. SPIE Medical Imaging; 2018; Houston, TX: SPIE.
[19] Raju PDR, Neelima G. Image Segmentation by using Histogram Thresholding. International Journal of Computer Science & Engineering Technology. 2012;2(1):776-9.
[20] Pokrajac DD, Maidment ADA, Bakic PR. Optimized generation of high resolution breast anthropomorphic software phantoms. Medical Physics. 2012;39(4):2290-302.
[21] Chui JH, Pokrajac DD, Maidment ADA, Bakic PR. Towards Breast Anatomy Simulation Using GPUs. Lecture Notes in Computer Science. 2012;7361:506-13.

[22] Bakic PR, Pokrajac DD, Caro RD, Maidment ADA. Realistic Simulation of Breast Tissue Microstructure in Software Anthropomorphic Phantoms. Lecture Notes in Computer Science. 2014;8539:348-55.
[23] Acciavatti RJ, Maidment ADA. Non-stationary model of oblique x-ray incidence in amorphous selenium detectors: I. Point spread function. Medical Physics. 2019;46(2):494-504.
[24] Acciavatti RJ, Maidment ADA. Nonstationary model of oblique x-ray incidence in amorphous selenium detectors: II. Transfer functions. Medical Physics. 2019;46(2):505-16.
[25] Ayyala RS, Chorlton M, Behrman RH, Kornguth PJ, Slanetz PJ. Digital Mammographic Artifacts on Full-Field Systems: What Are They and How Do I Fix Them? RadioGraphics. 2008;28:1999-2008.
[26] Geiser WR, Haygood TM, Santiago L, Stephens T, Thames D, Whitman GJ. Challenges in Mammography: Part I, Artifacts in Digital Mammography. American Journal of Roentgenology. 2011;197:W1023-W30.
[27] Vedantham S, Karellas A, Vijayaraghavan GR, Kopans DB. Digital Breast Tomosynthesis: State of the Art. Radiology. 2015;277(3):663-84.
[28] Acciavatti RJ, Maidment ADA, editors. Optimization of Continuous Tube Motion and Step-and-Shoot Motion in Digital Breast Tomosynthesis Systems with Patient Motion. SPIE Medical Imaging; 2012; San Diego, CA: SPIE.

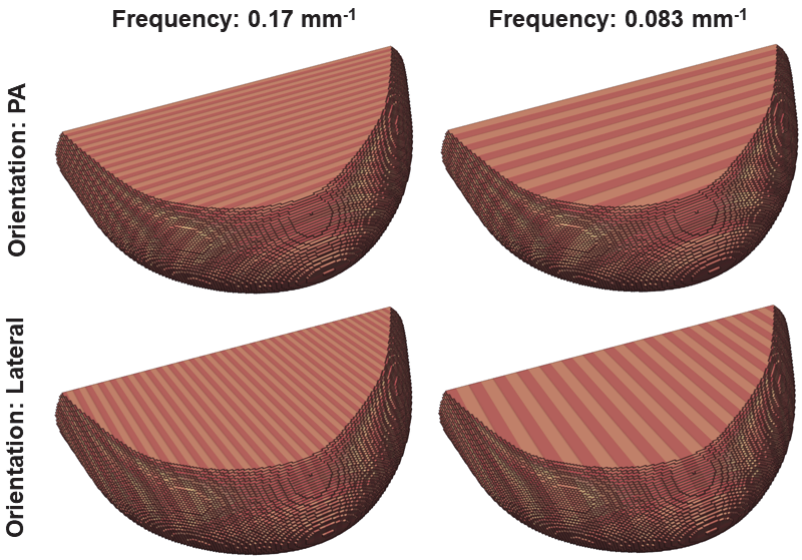

Figure 1. The two tissue types, fibroglandular and adipose, were arranged in a Defrise pattern (a square wave). We varied both the orientation and magnitude of the frequency.

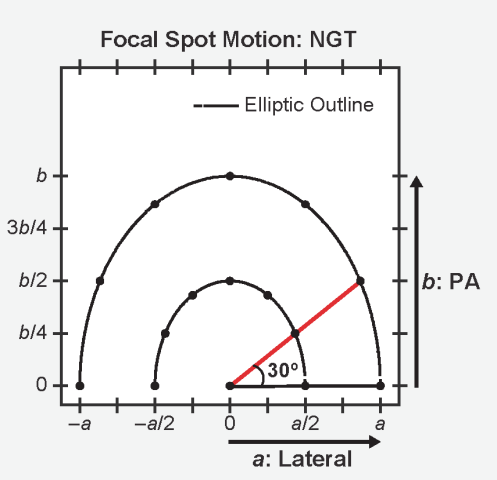

Figure 2. Acquisition geometries were simulated with source positions arranged in elliptical arcs. Parameters *a* and *b*, controlling the range of source motion in two directions, were each varied in 21 steps.

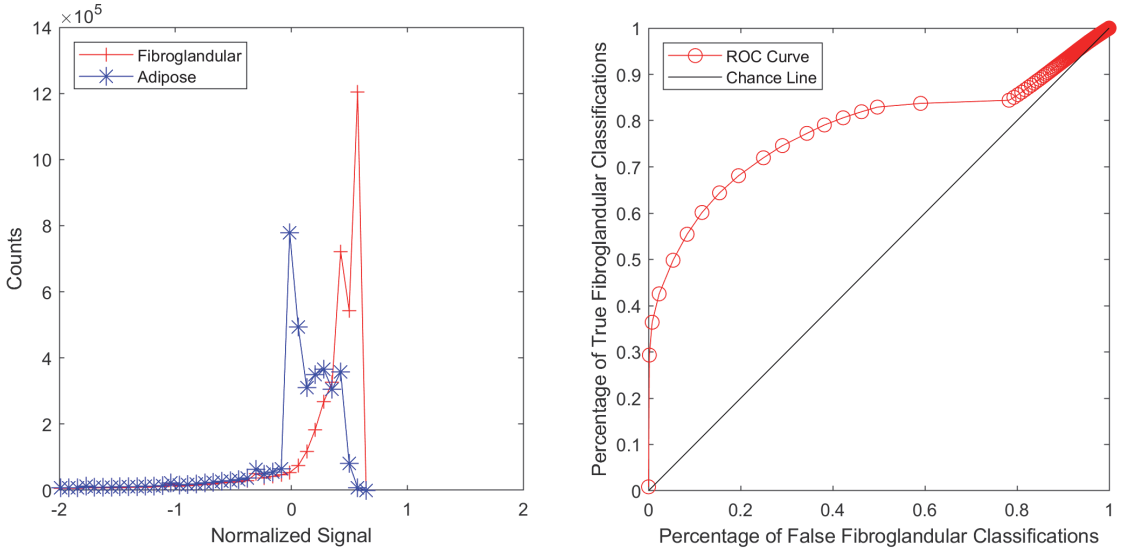

Figure 3. (a) Signal intensity was analyzed separately in each tissue type. (b) A threshold can be introduced to classify each voxel in the reconstruction as either fibroglandular or adipose tissue. Each point on the ROC curve corresponds to a different threshold. AUC is a measure of how well the two tissue types are separated.

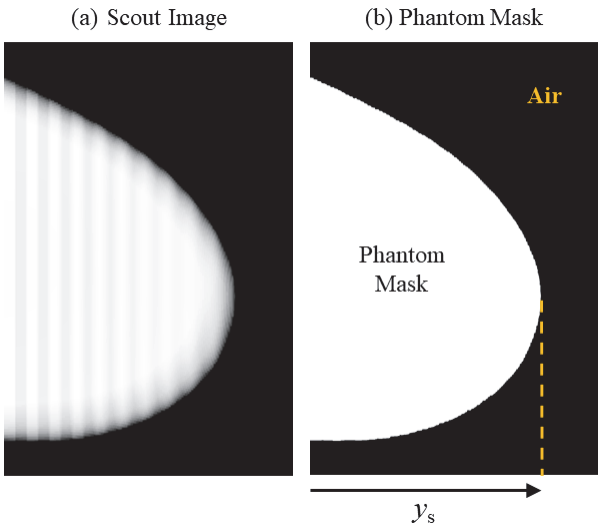

Figure 4. A scout image (a) was used to create a mask of the phantom (b). This in turn was used to estimate the PA dimension of the object.

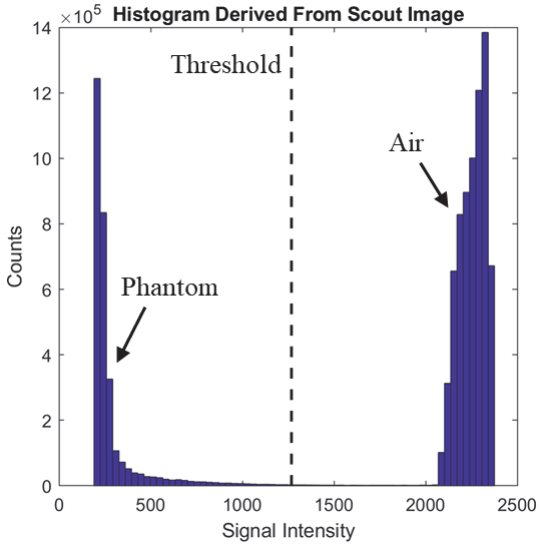

Figure 5. In the histogram derived from the scout image, we applied a threshold (dashed vertical line) to segment phantom signal from background.

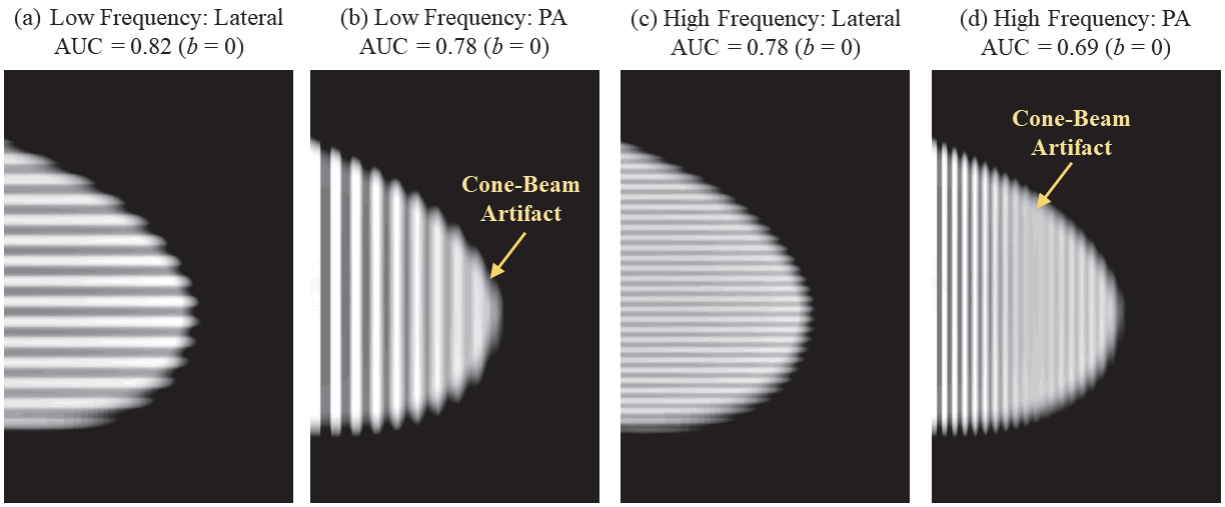

Figure 6. These reconstructions in a conventional acquisition geometry (a = 100.0 mm, b = 0) illustrate how the orientation and magnitude of the input frequency affect the presence of the cone-beam artifact.

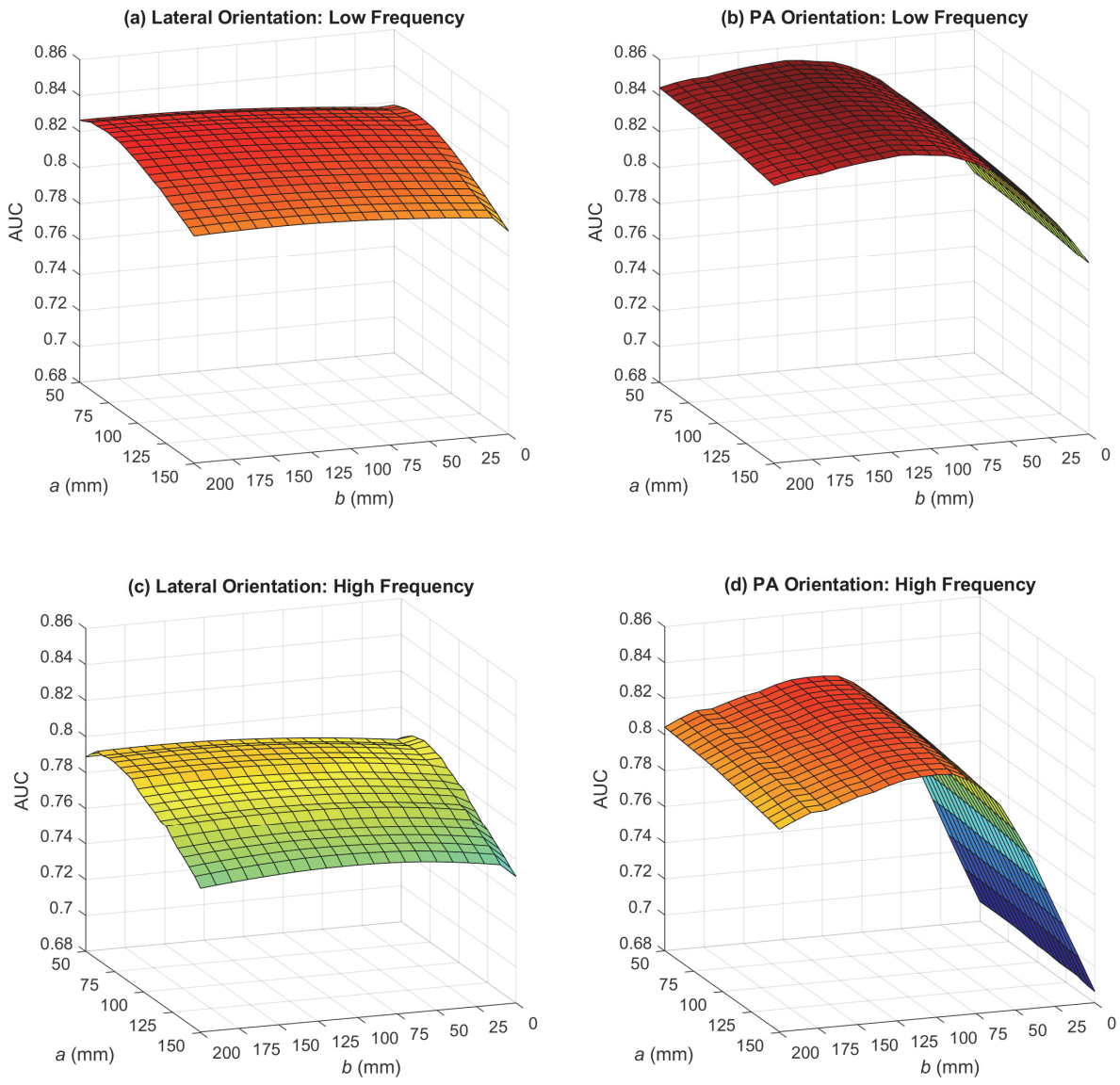

Figure 7. We illustrate how AUC is dependent on the acquisition parameters (*a* and *b*) in one phantom (CND of 12 cm). Two frequencies and two orientations of the Defrise pattern were analyzed. Similar surface plots were created for all phantoms. Each surface plot was used to quantify the total range of AUC variation (ΔAUC), a measure of how much image quality is sensitive to the acquisition geometry.

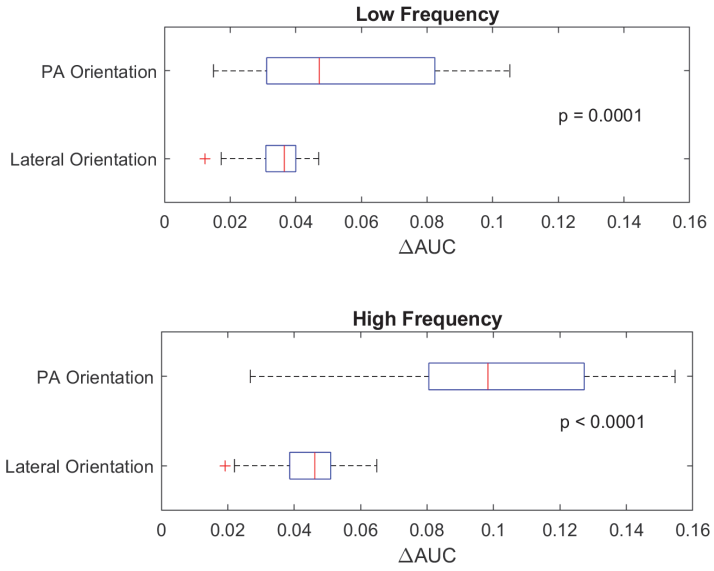

Figure 8. The quantity ΔAUC is a measure of how much image quality is sensitive to variations in the acquisition parameters. Two orientations of the Defrise pattern were analyzed. Image quality is less sensitive to the acquisition parameters if frequency is oriented laterally. Therefore, optimization of the acquisition parameters is not as critical in this orientation.

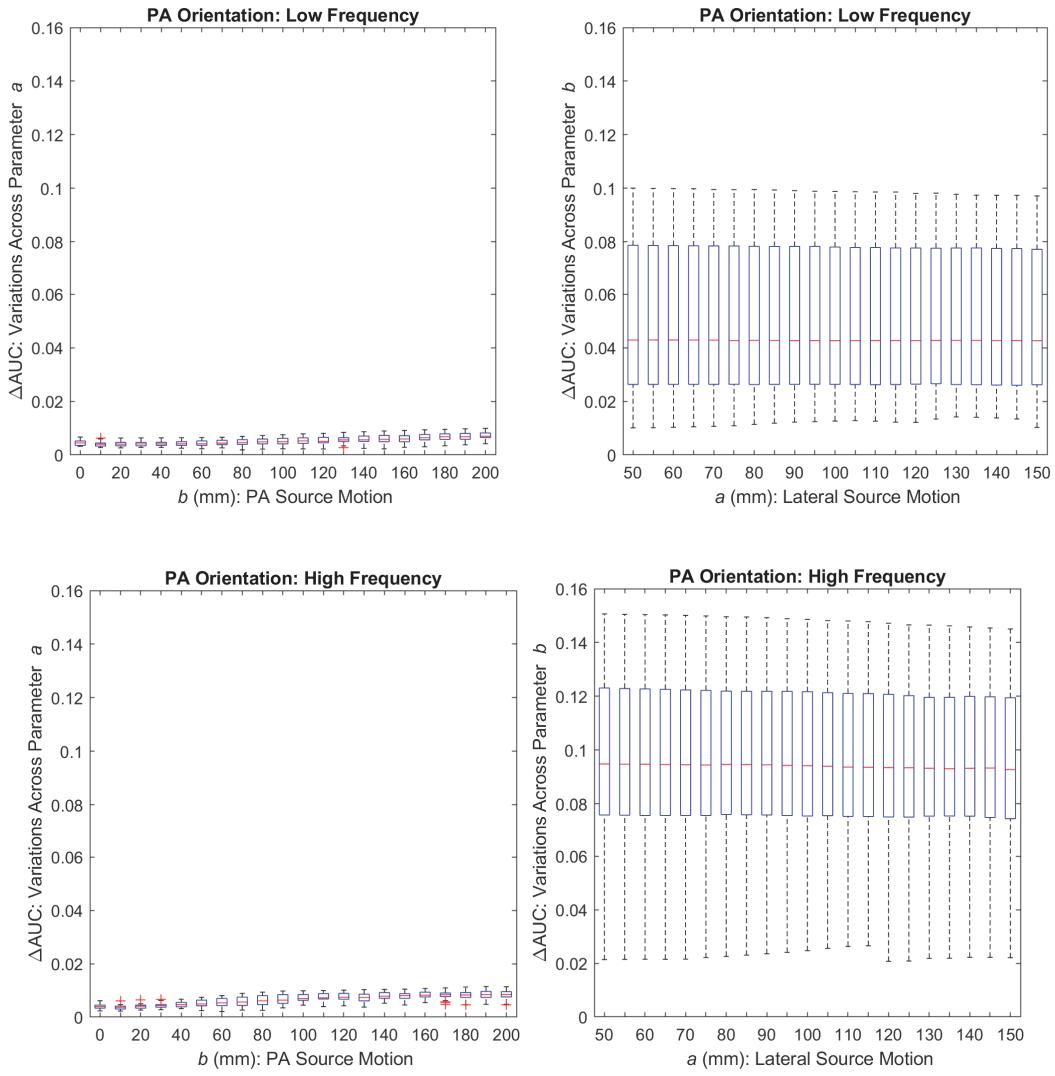

Figure 9. The AUC results were analyzed for the PA orientation of the phantom. There was minimal change in AUC under variation in parameter *a* (the lateral range of source motion), and substantial change in AUC under variation in parameter *b* (the PA range of source motion). Therefore, varying parameter *b* has a more pronounced effect on the image quality.

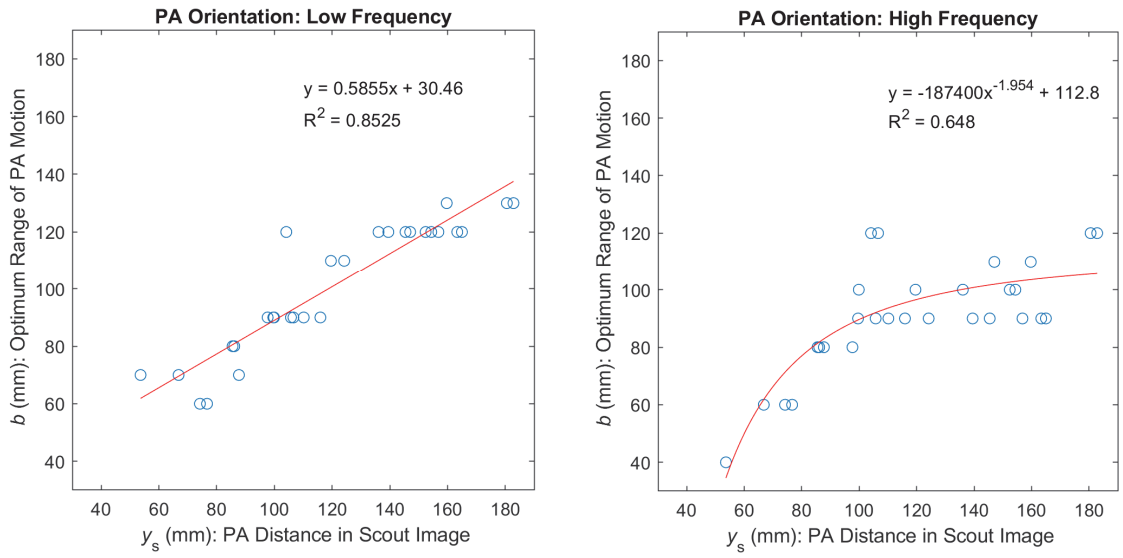

Figure 10. The acquisition parameter *b* corresponding to the highest AUC was calculated, and found to increase with the size of the phantom in the PA direction. We show that the optimum scanning motion is also dependent on frequency.

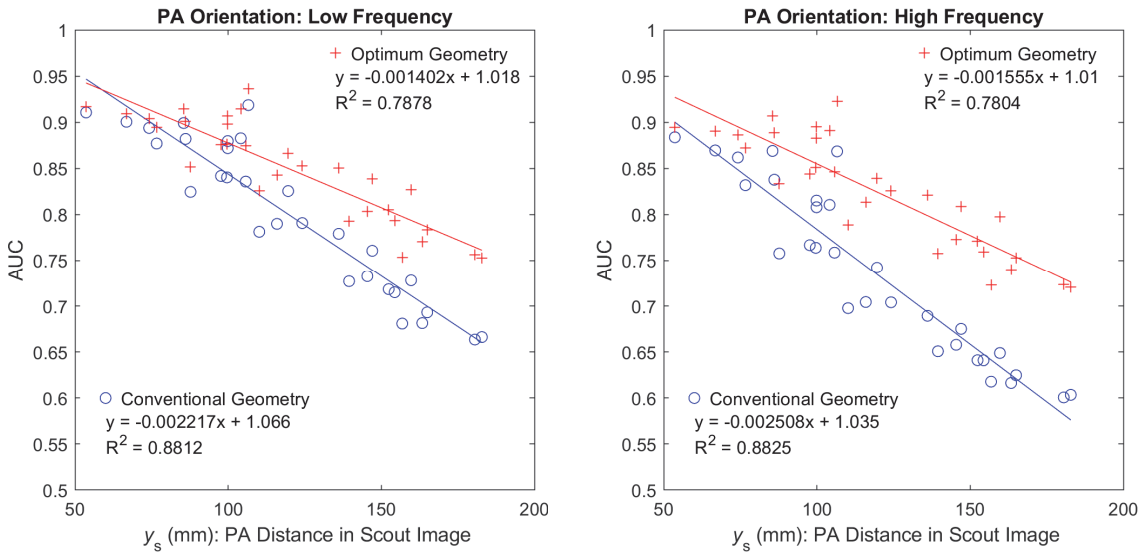

Figure 11. Image quality is poorer in phantoms with a broader extent in the PA direction, not just in the conventional geometry but also in the optimized geometry.

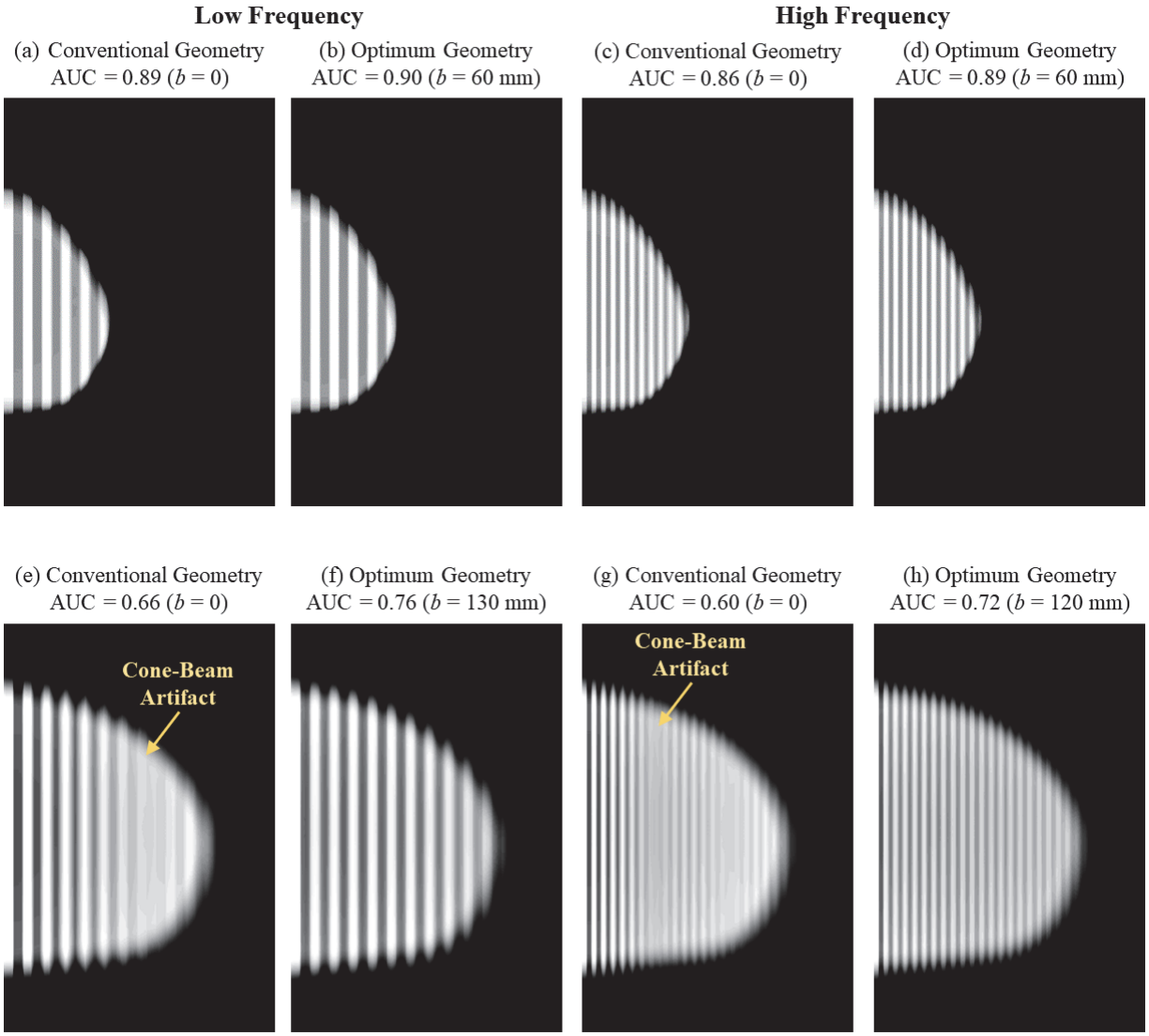

Figure 12. The cone-beam artifact is effectively absent in a phantom with a small CND (7.1 cm), and hence it is less critical to optimize the acquisition parameters (top row). By contrast, the cone-beam artifact is prominent in a larger phantom (CND of 16 cm), and PA source motion is necessary to optimize the image quality (bottom row).

Development and Evaluation of a Spatial Resolution Metric for Tomosynthesis

Trevor L. Vent, Raymond J. Acciavatti, and Andrew D. A. Maidment

Abstract—An in-plane resolution metric is presented for tomosynthesis. The radial fast Fourier transform (RFFT) metric evaluates resolution of different imaging techniques for digital breast tomosynthesis (DBT). This metric was developed to investigate alternative acquisition geometries for a next generation tomosynthesis (NGT) prototype. The Radial FFT metric uses a star pattern input to plot modulation in the frequency domain. The RFFT graph portrays all frequencies that are present in a star pattern quadrant of the image reconstruction and presents the data in a different format. In addition to the fundamental input frequency of the star pattern, the RFFT graph shows spectral leakage, square wave harmonics, and residual noise. The CTF is obtained using the RFFT graph. The CTF is analogous to the modulation transfer function (MTF), but it is not normalized to unity at the zero spatial frequency. The results verify that super-resolution is present for all frequencies that are parallel to the scanning direction of conventional DBT, and that aliasing is present for frequencies aligned perpendicular to the scanning direction. The Radial FFT metric separates the fundamental-input frequency from spectral leakage and determines the in-plane limit of spatial resolution with respect to aliased signals. The Radial FFT metric adequately compares resolution properties of 2D images and 3D image reconstructions for various x-ray imaging modes without suppressing aliased signals.

Index Terms—Digital breast tomosynthesis, super-resolution, spectral leakage, aliasing, modulation transfer function, contrast transfer function, radial fast Fourier transform.

I. INTRODUCTION

CONVENTIONAL digital breast tomosynthesis (DBT) systems acquire multiple x-ray projections over a range of angles along a linear trajectory. The collected projections are then back-projected to reconstruct a 3D image. Whereas a tomosynthesis acquisition produces a 3D dataset suitable for multiplanar reconstruction, the data are most frequently read by radiologists in a series of 2D planes arrayed parallel to the breast support. This is due, in part, to the fact that DBT provides high in-plane resolution [1]; we have shown in previous work that DBT image reconstructions are capable of super-resolution [2]–[5]. Super-sampled tomosynthesis reconstructions produce reconstructed image slices that can accurately represent spatial frequencies above the detector alias frequency (ξ). DBT is also referred to as limited-angle tomography and produces anisotropic resolution in image reconstructions. Super-resolution is achieved for frequencies that are aligned parallel to the x-ray source motion (σ), but not achieved for frequencies that are aligned perpendicular to σ [3]. Many methods to evaluate the spatial resolution of DBT systems exist. One such metric is the modulation transfer function (MTF). The importance of measuring both the 3D MTF and the in-plane MTF for tomosynthesis was presented by Zhao *et al*. [6]. The metric that we introduce in this paper is an in-plane spatial-resolution metric that is beneficial for evaluating tomosynthesis. This metric evaluates the spatial resolution without suppressing aliased signals.

A. Spatial Resolution for Tomosynthesis

The spatial resolution of tomosynthesis images depends on intrinsic system properties and the image sampling and interpolation techniques used in back projection [2], [5]. The superior resolution observed with DBT is the result of improved spatial sampling. [2]. According to the central slice theorem, the Fourier representation of a 2D x-ray projection is a single plane describing the sampled frequencies. The Fourier representation of the sampled data for a conventional tomosynthesis acquisition is a collection of 2D frequency planes that are isocentric about the axis of rotation of σ. This depiction is often conceptualized as a double-napped cone (Fig. 1).

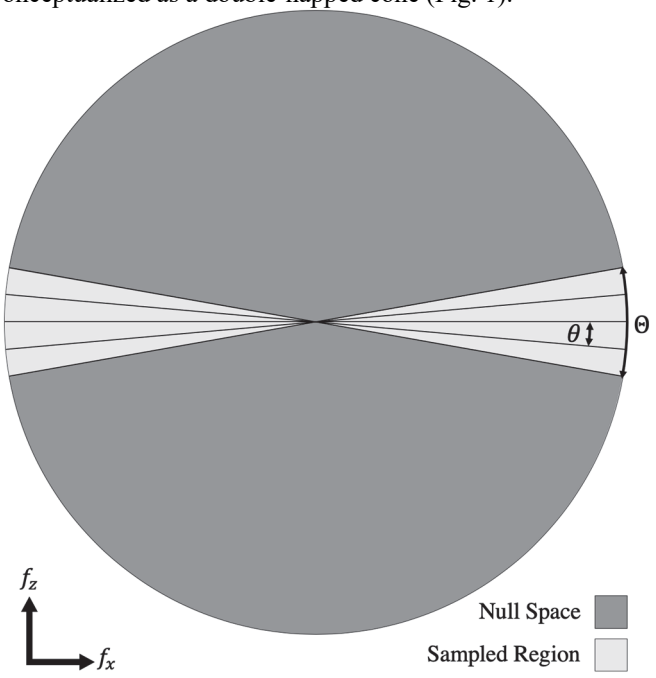

Fig. 1: Diagram of the $f_x - f_z$ plane in the Fourier domain for a simplified conventional tomosynthesis acquisition. Note that f_y is into the page and that each line in this example represents an individual x-ray projection; this example only contains 5 projection images rather than 15 for simplicity. Θ represents the entire angular range of the x-ray source and θ is the angle between projections.

The angular offset of one plane relative to another (e.g. θ, Fig. 1) is determined by the angular offset, relative to the reconstructed volume, of the x-ray source per projection in the physical domain. The parameter, θ, is inversely proportional to the sampling *density*. Higher sampling density improves the resolution of reconstructed images. If one considers the 3D

Fourier domain, a double-napped cone represents a greater sampling volume and density than a single plane.

The size and shape of the sampled volume within the Fourier domain is dependent upon the acquisition geometry [6], [7]. The capability of a tomosynthesis system to achieve super-resolution is dependent on the orientation of frequencies relative to the sampled volume within the Fourier domain. Super-resolution is achieved in σ, because for this orientation, the frequencies (f_x) are aligned parallel to source motion and circumscribed within the sampled volume of the Fourier domain entirely. The back-projection of these images can be super-sampled such that the reconstructed image grid is finer than the detector element pitch (d_{el}) [5], [8]. However, DBT acquisitions are an under-sampled dataset, because the double-napped cone does not cover the entire 3D Fourier volume. This unsampled volume is known as the null space (Fig. 1). Whereas some multiplanar reconstructions exhibit super-resolution [3], most do not and may contain image artifacts like aliasing.

B. Alias Frequency in Digital Detectors and Sampling

Digital imaging systems have an alias frequency above which objects are not correctly resolved. The alias frequency, ξ, of an imaging system is given by one half of the first zero of the Fourier transform of the system's d_{el}. The Fourier transform of an aperture is, sinc(d_{el}), and the alias frequency is given by:

$$\xi = \frac{0.5}{d_{el}} \quad (1)$$

Aliasing is predominant in 2D images for any frequency orientation above ξ.

The prominence of aliasing in 3D image reconstructions depends on the sampling techniques and the orientation of the input object. Two factors can give rise to aliasing in 3D image reconstructions, sampling pitch (λ) and sampling aperture of the detector, d_{el}. For a DBT reconstruction, aliasing is present and manifested as Moiré patterns in digital images if the λ is below the Nyquist rate (Ξ) for the given d_{el}, regardless of the object orientation. However, if we consider a conventional DBT acquisition geometry and λ is at or above Ξ for an image reconstruction, aliasing is only present for frequencies that are aligned perpendicular to x-ray source motion. In the Fourier domain, aliasing takes the form of *spectral leakage*, which is the misrepresentation of the modulation of the input frequency at an incorrect, lower or higher frequency (the shaded region in Fig. 2c). Aliasing dominates the input signal of these reconstructions because the magnitude of the spectral-leakage modulation is greater than the magnitude of the input-frequency modulation in the Fourier domain. A pre-sampled MTF calculation for any x-ray imaging device shows modulation for frequencies higher than ξ. This is evidence that super-resolution is achievable with proper sampling and reconstruction techniques. However, the pre-sampled MTF will not show that the frequencies above ξ are dominated by aliasing.

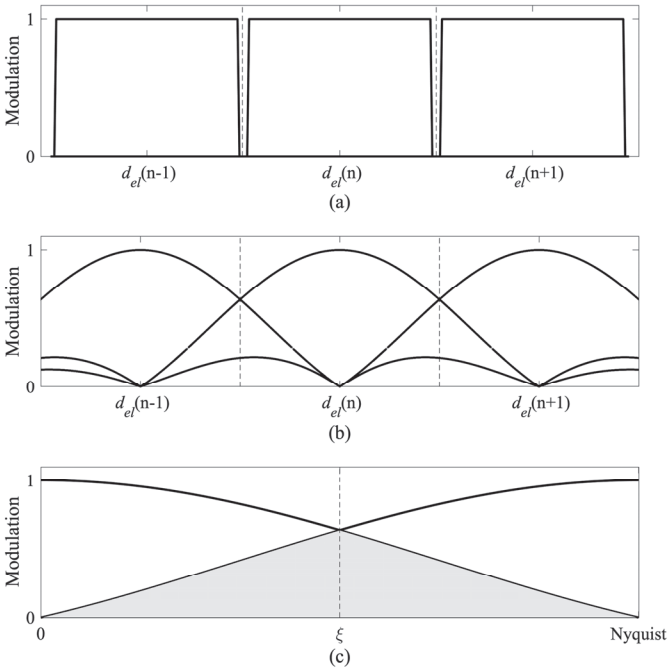

Fig. 2: A digital detector aperture function for three detector aperture samples (a), the impulse responses of the three apertures (b), and an example of the aliased signals from d_{el}(n+1) reflected back into the impulse response function for half of one detector aperture, d_{el}(n) (c).

C. Resolution Metrics

Various DBT systems are available for screening mammography, and each system is constructed with a distinct mechanical design and geometric configuration. Additionally, these systems vary in terms of the number of projections and angular range. The variation in the mechanical design and acquisition techniques of these systems necessitates a metric that can distinguish aliasing and establish a standard for comparing one system to another. IEC 62220-1 outlines a method to measure the MTF of x-ray systems using the slanted edge [9], and AAPM TG-245 proposes an alternative approach by using a tilted tungsten wire. Both of these methods suppress aliasing through super-sampling. We are seeking a resolution metric that will reveal aliasing.

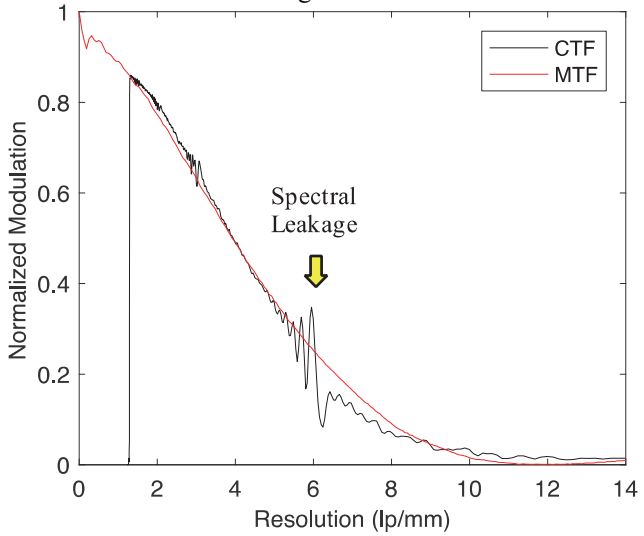

Fig. 3: The normalized modulation of the CTF and MTF are plotted as a function of spatial resolution. The distinction between the MTF and CTF is the

characteristic oscillatory behavior of the CTF plot. These oscillations are a manifestation of spectral leakage.

In this paper, we propose a radial fast-Fourier transform (RFFT) metric and the contrast transfer function (CTF) that assesses spatial-resolution without suppressing relevant information, like aliasing. The RFFT metric discerns aliasing by identifying the spectral leakage separate from the fundamental input frequencies in the Fourier domain. An example is the oscillatory behavior of the CTF graph in Fig. 3. The CTF is analogous to the MTF but is not normalized to unity at zero spatial frequency. The MTF calculation for this system was measured using the slanted edge method [7]. The slanted-edge method enforces a fixed phase shift of one line relative to another which suppresses spectral leakage through super-sampling and thus renders the MTF unable to discern aliasing.

II. Materials & Method

A. Next-generation tomosynthesis prototype

The Radial FFT metric was developed for characterizing our next-generation tomosynthesis (NGT) prototype system. The NGT system configuration is shown in Fig. 4. This prototype was developed to investigate novel acquisition geometries for DBT. Whereas a conventional DBT system scans linearly in one dimension, the NGT prototype positions the x-ray source at various locations within the source plane for a 3D acquisition, introducing σ in the posteroanterior direction. This sampling technique enhances the sampled frequencies in the Fourier domain [7]. The source-to-image distance (SID) for the NGT system is 652 mm. The range of motion for the x-ray tube is ±125 mm in x (R_x) and +180 mm in y (R_y). Given these ranges, the NGT prototype is capable of investigating myriad acquisition geometries [11]. For this work, we use a conventional DBT acquisition geometry (NGT-X) to introduce this metric.

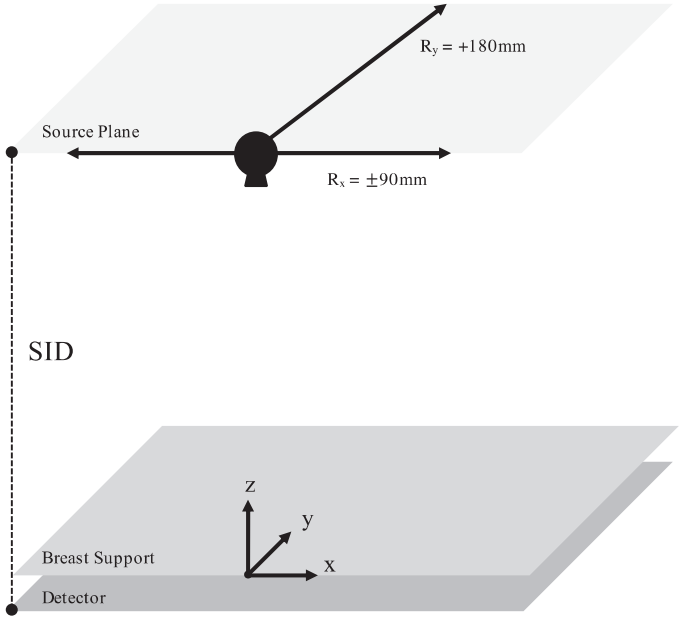

Fig. 4. The coordinate axes and the design geometry are defined for the NGT prototype. The x-y-z coordinate system defines the origin of the NGT system. It is located at the center of the of the detector along the chest-wall edge relative to the patient. The x-axis is parallel to the chest wall and is also parallel to σ for a conventional DBT acquisition.

B. Star Pattern Test Object

To obtain the CTF, we use the frequencies contained in one quadrant of a star-pattern test object as the fundamental input frequency (ν). The star pattern consists of four quadrants of 29 alternating lead and acrylic sectors at 1° spacings. The angular range of each quadrant is 29° (model 07-542-1000). The sharpness of the edge on the lead foil is a square-wave input similar to a bar-pattern test object. The Fourier transform of a square-wave of length L is a series of sinusoidal waves:

$$F(t) = \frac{4}{\pi}\sum_{m=1}^{\infty}\frac{-1^{m-1}}{2m-1}\mathrm{Cos}\left(\frac{2\pi m t}{L}\right) \quad (2)$$

The fundamental frequency (m=1) is the most accurate representation of the star pattern input frequencies and is the dominant frequency in an image reconstruction. The finite size of the focal spot and the diffraction of the x-rays blur the signal of the high frequencies, producing a sinusoidal response function (Fig. 5). As predicted by Coltman [13], square-wave harmonics are also present in image reconstructions at lower spatial frequencies of the star pattern. This is expected because the intensity profiles of the lower frequencies in a star pattern image are more square-like than the intensity profiles of higher frequencies; there is a lack of blurring at the lower spatial resolutions of the star pattern (1.27-2.5 lp/mm).

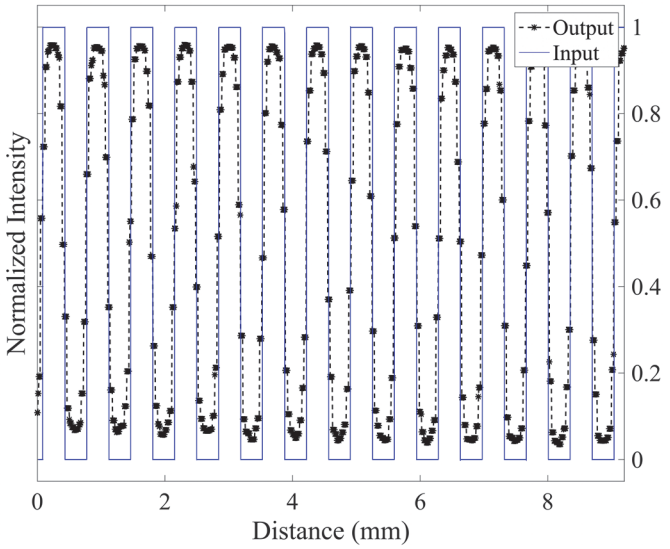

Fig. 5. The sine-wave response (Output) of the square wave (Input) at a resolution of 1.4 lp/mm in the image reconstruction of the star pattern [13].

C. Image acquisition

Images of the star pattern were acquired on the NGT prototype using various techniques. The star pattern was positioned at the origin with a ϕ of 0°. The term, ϕ, is the alignment angle of the frequencies of the star pattern relative to the detector grid. The conventional acquisition geometry of the NGT system (NGT-X) mimics the tomosynthesis acquisition of a clinical DBT system (Selenia Dimensions, Hologic, Marlborough, MA). NGT-X was used to obtain image reconstructions. NGT-X was repeated ten times by removing and repositioning the star pattern at the origin with the same ϕ between each acquisition. The central projection from each of the ten tomosynthesis acquisitions was used to obtain 2D data.

Each projection image was acquired using 28 kV, 1.5 mAs, and 0.5 mm Aluminum filtration.

The projection images were reconstructed using commercial reconstruction software (Real Time Tomography: Villanova, PA). This reconstruction software is capable of super-resolution and multiplanar reconstruction. The software can produce super-sampled reconstructed volumes with a λ of up to 10 times the detector aperture. The 3D images were reconstructed at 5 different λ values: 85.0 µm (1.0x), 56.7 µm (1.5x), 42.5 µm (2.0x), 37.0 µm (2.3x), and 28.3 µm (3.0x). The 3D images are reconstructed conventionally, with slices parallel to the x-y plane using simple back projection. The slice of the in-focus star pattern (in-plane 3D) or individual projections (2D) are used as the 3D and 2D inputs to the RFFT metric. A summary of the acquisitions and reconstruction techniques performed for this study is shown in Table I.

TABLE I
IMAGE ACQUISITIONS

Acq.	Acq. Geo.	Star Pattern Alignment (ϕ)	λ, (μm)	Samples	Technique
a			85.0 (1.0x)	1	
b			56.7 (1.5x)	1	28 kV
c	NGT-X	0°	42.5 (2.0x)	10	1.5 mAs
d			37.0 (2.3x)	1	Al Filter
e			28.3 (3.0x)	1	

Images were obtained using the NGT prototype. The same technique was used for all acquisitions. The ten 2D images were obtained from the central projection of the tomosynthesis acquisition. the NGT-X acquisition that was repeated ten times.

D. Radial Fast Fourier Transform Metric

The RFFT is calculated using one quadrant of a star pattern image as an input to create a graph of modulation in the frequency domain. This graph is referred to as the radial fast Fourier transform (RFFT) graph. The RFFT graph is the normalized modulation of all frequencies contained within a quadrant of the star pattern. It presents data in a more useful format to evaluate aliasing and super-resolution.

The center of the star pattern is determined using an image of the star pattern. The center is calculated using the perpendicular bisectors of two secant lines that are created by choosing two intersections arbitrarily between the three points located along the profile of the outer circle of the star pattern image (Fig. 6). Then, starting at the radius (r) from the center of the star pattern to the inner ring ($r_{min} \widehat{=}$ 20 lp/mm), the plot profile, $\psi(r)$, is extracted radially for the quadrant of interest. The quadrants are named by the angle in radians relative to the center (0, π/2, π, and 3π/2). Each quadrant has an angular range of 29°.

The 1D fast Fourier transform (FFT) is computed for this profile. The 1D FFT of $\psi(r)$ computes the modulation of each frequency–aliased or not–within the quadrant. The radius is then incremented by one pixel and the process is repeated to the outer ring of the star pattern ($r_{max} \widehat{=}$ 1.27 lp/mm). An example of one FFT calculation at a radius of 8 lp/mm is shown in Fig. 6.

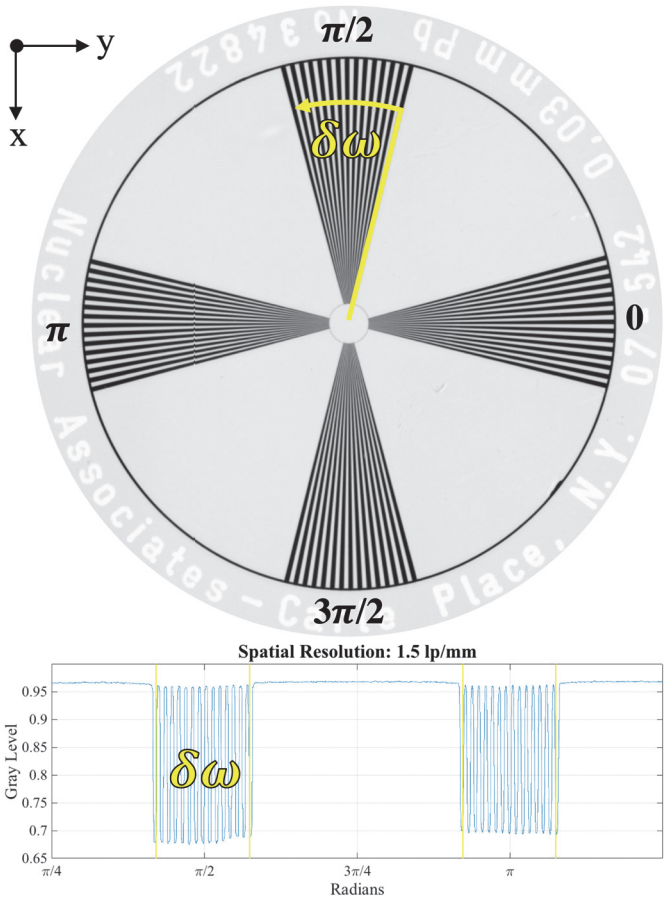

Fig. 6. The profile extraction of the 0-radian quadrant for f_y at a resolution of 1.5 lp/mm. $\delta\omega$ represents the range of the quadrant at all radii. The plot profile, $\psi(r)$, is shown in blue and the quadrant is named by the angle of the unit circle in radians.

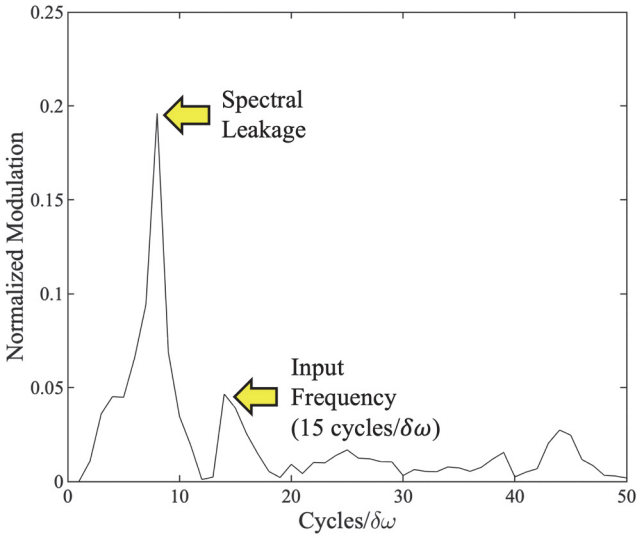

Fig. 7. Example of the 1D FFT at a radius of 8 lp/mm. The modulation of the aliased signal is well above that of the input frequency for this example.

The waveform of each quadrant was sampled using Fourier interpolation with four increments at each radius: 512, 1024, 1536, and 2048. These four conditions and oversampling factors (Γ) for the range of frequencies of the star pattern are summarized in Table II. The value of Γ was determined by the sample size (N) over the number of pixels per $\psi(r)$ for r_{min} and r_{max} and an a 37μm λ:

$$\Gamma(r) = \frac{N}{pixels/\psi(r)} \quad (3)$$

TABLE II
RFFT SAMPLING RATES FOR $\delta\omega$

Condition	SAMPLE RATE (N)	Oversampling Factors, Γ(1.27 – 20 lp/mm)
A	512	1.6 – 25
B	1024	3.2 – 50
C	1536	4.8 – 75
D	2048	6.4 – 100

The four conditions of sampling used to determine optimal sampling rate for RFFT calculations. The values of Γ correspond to a reconstructed pixel pitch of 37 μm. The oversampling factor increases with resolution, and the N is the same for each $\delta\omega$.

The angle at which the star pattern input frequencies are oriented across the reconstruction grid varies from one edge of the quadrant to the other. When ϕ=0, the largest angle of orientation for the frequencies is approximately 15° relative to the reconstruction grid (Fig. 8). For comparison, the MTF should be computed using an edge that is aligned at 2.5° (relative to the detector grid) with an ROI of at least 10 cm to achieve sufficient sampling [14]–[16]. The radial sampling of the star pattern has a similar effect and is observed as the various different vertical positions of the star points in Fig. 5.

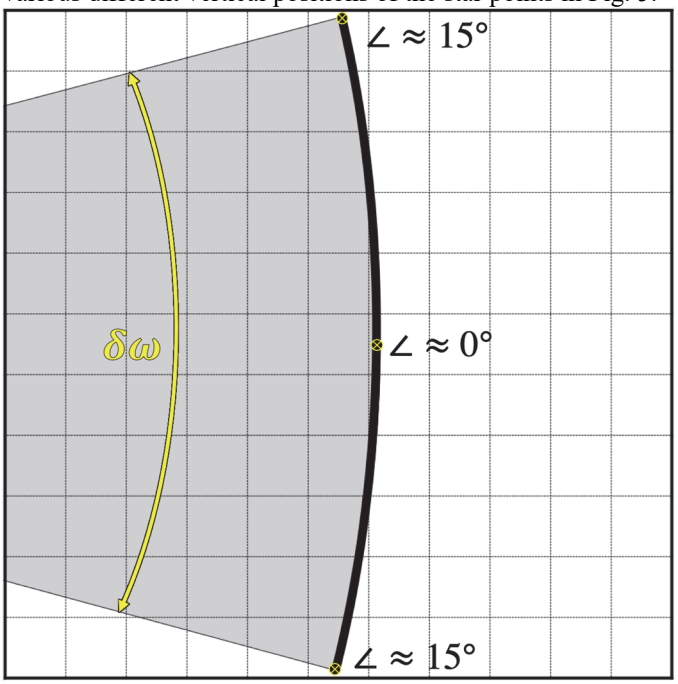

Fig. 8: Angular variation of the plot profile over the range, $\delta\omega$.

The maximum modulation of the input frequency, ν, is normalized to the value of the pre-sampled MTF at 1.27 lp/mm, and the 1D FFT profiles are plotted as a function of resolution (lp/mm) and period (cycles/δω) to create the RFFT graph (Fig. 9). The most prominent spine in the graph is the signal of the input frequency, which is located at 15 cycles per quadrant (cycles/δω). Spectral leakage that arises from the sampling aperture is also prominent at various other cycles, creating a spine of frequencies that intersects ν at ξ. Spectral leakage that arises from λ creates a spine that intersects the ν at λ. When present with a greater magnitude than the input frequencies, aliased signals dominate the input signals in image reconstructions. The least prominent spine in the plot occurs at 45 cycles/δω and represents the modulation for a square wave harmonic of the star pattern (m=3). The input of the star pattern would produce an exact square wave response function if there were no intrinsic blurring of the system. The waveform is sinusoidal in the plot profile but maintains square-wave characteristics for resolutions lower than 2.5 lp/mm. This follows the findings of Coltman for the sine-wave response function given a square-wave input [13]. Image noise contributes to the rough texture observed in the other areas of the graph. The RFFT graph produces a super-sampled Fourier transform of a quadrant in the star pattern. In contrast to the pre-sampled MTF, the RFFT identifies aliasing as spectral leakage in digital x-ray images.

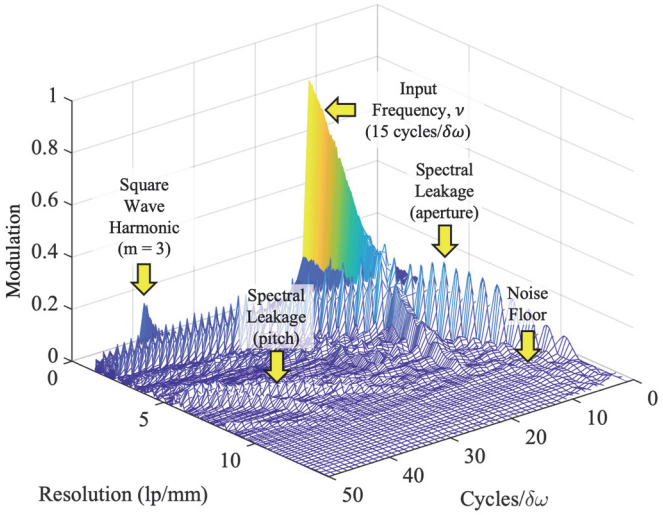

Fig. 9. An example of the Radial FFT graph for y-direction frequencies of a star pattern. The spine of the fundamental frequency (ν) occurs at a period of 15 Cycles/$\delta\omega$. The spine of spectral leakage intersects the fundamental frequency at a resolution of 5.88 lp/mm (ξ). The spine of the square wave harmonic for m = 3 occurs at 45 cycles/$\delta\omega$.

E. Contrast Transfer Function

The CTF graph is the normalized modulation of ν, obtained from the RFFT graph, as a function of resolution. The CTF is commensurate to the square-wave response function that is calculated from the sine-wave output of the star pattern [13]. The CTF is used to discern the aliasing-dependent limit of spatial resolution (LSR) and is plotted against the pre-sampled MTF (see Fig. 3).

III. RESULTS

A. Evaluation of Sampling Rate for RFFT

The RFFT was computed at the four different sampling rates using the π/2-radian quadrant (f_y) of one of the images from acquisition **a**. The differences in the RFFT graph are indiscernible via visual inspection; thus, only the two spectra that show the greatest absolute differences are used as examples (N= 512 and 2048) in Fig. 10a-b. Also presented in Fig. 10c is a graph that shows the differences between the two examples. The maximum absolute difference at any point of any of the conditions tested is 0.018, and the average absolute difference

is 0.0011 between the four conditions.

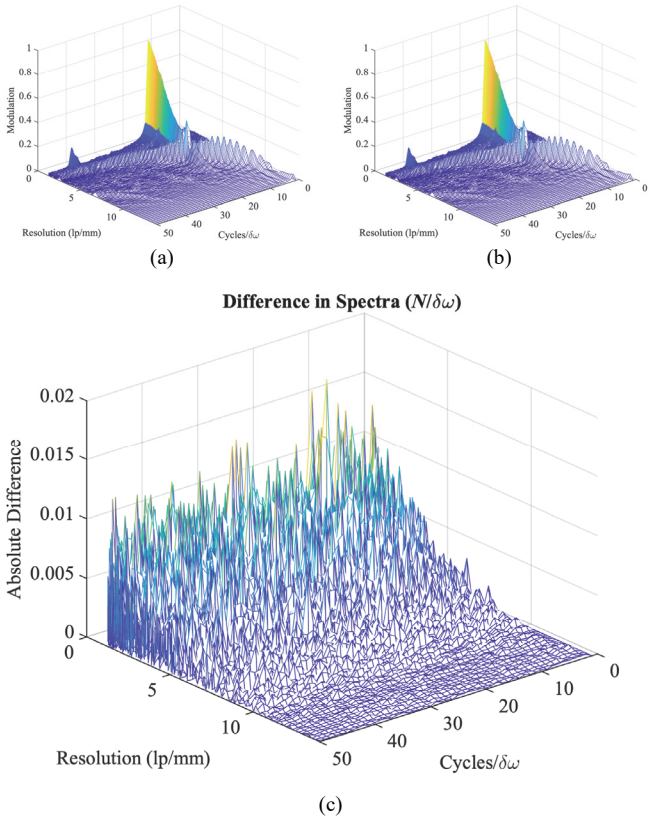

Fig. 10: Sampling rates: (a) 512, (b) 2048, and their difference (c) used to determine optimal sampling for the RFFT.

B. 2D RFFT for NGT System

The RFFT was computed for the ten 2D projection images using images obtained from acquisition **c**. The range of Γ at this pixel size (85μm) is approximately 11 – 175. Fig. 11 shows the RFFT graph for f_x as an example. The average spectra of the ten 2D projection images is shown for f_x (Fig. 12a) and for f_y (Fig. 12b). The spectral leakage of d_{el} intersects ν at the resolution of d_{el}, and λ intersects at the Nyquist rate of the detector.

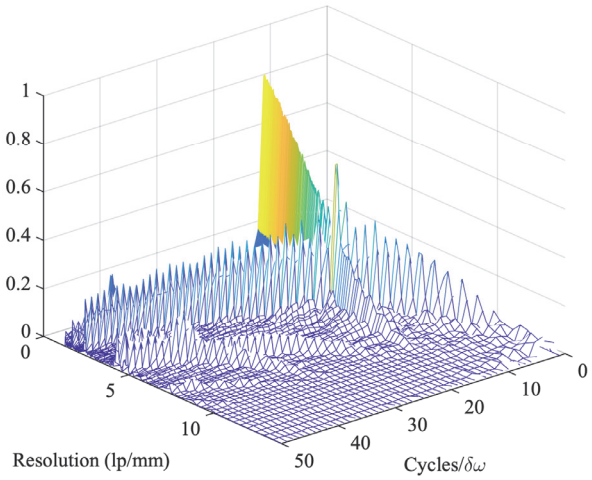

Fig. 11: RFFT graph of a single 2D projection image.

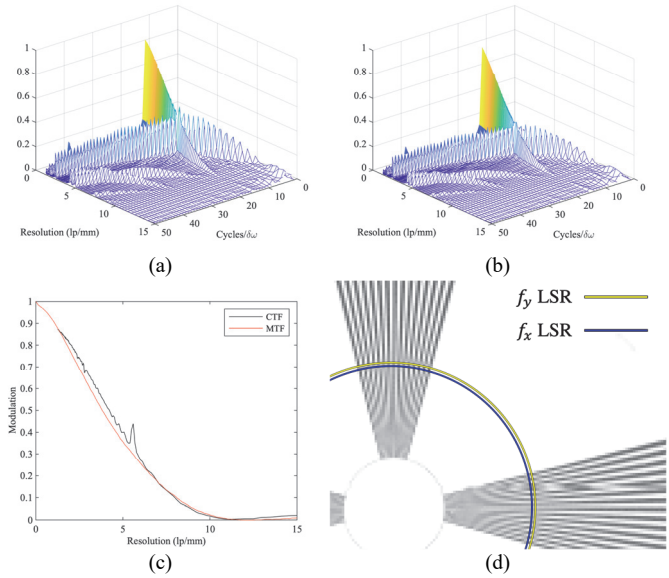

Fig. 12: The results for the average 2D spectra include the RFFT graphs for f_y (a), f_x (b), the CTF graph for f_y (c), and the image indicating the LSR for f_y and f_x (d).

C. 3D RFFT for Various Reconstruction Pitch Values

The RFFT was computed using images that were obtained from the five reconstruction λ values of NGT-X described in Table I using acquisitions **a**-**e**. The five RFFT and CTF graphs are summarized in Fig. 13 for their respective reconstruction λ values. The spectral leakage that arises due to the λ intersects ν at the resolution corresponding to the λ for each graph. Similarly, residual spectral leakage is seen at the resolution corresponding to d_{el}.

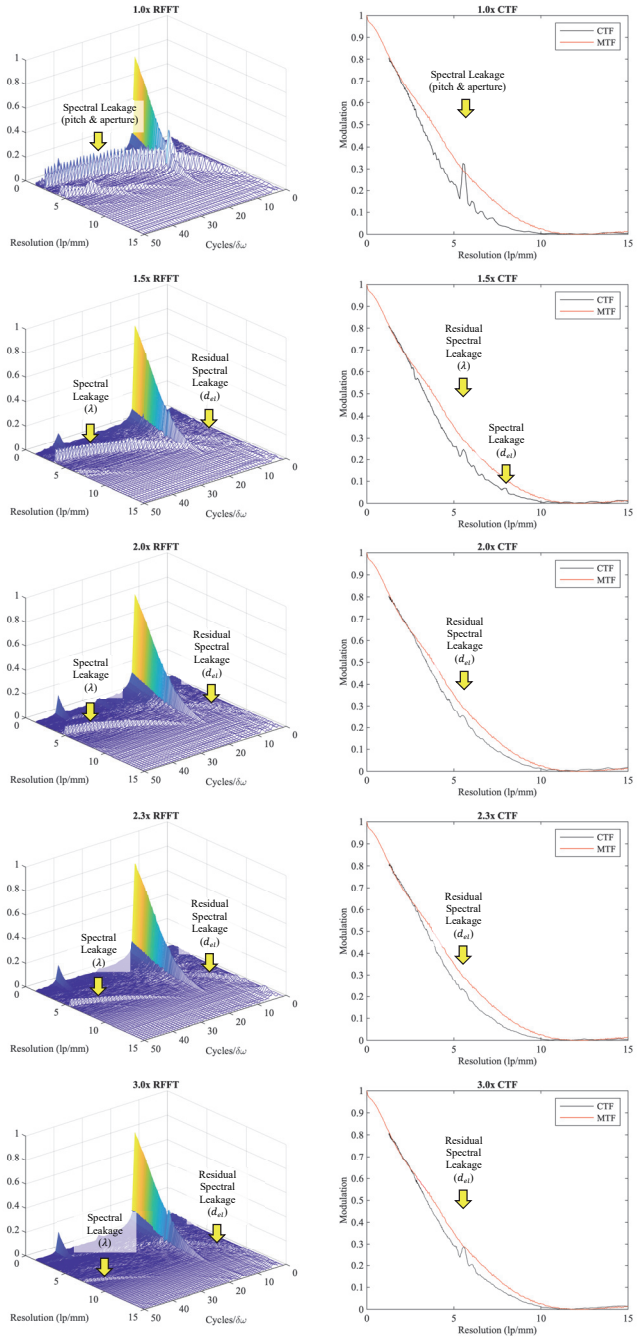

Fig. 13: These graphs were created using f_x of NGT-X. The RFFT (left column) and CTF vs. pre-sampled MTF (right column) graphs for the five λ values from Table I are shown. The two forms of spectral leakage, aperture (d_{el}) and pitch (λ) are indicated. Note that the aperture spectral leakage is only residual.

D. Comparing f_x with f_y for Conventional DBT

The results for NGT-X are represented in Fig. 14 and Fig. 15 for the 0- and π/2-radian quadrants of the star pattern, respectively. Images for NGT-X were obtained from acquisition **c**; these graphs represent the average of the ten spectra. The average spectra are less noisy than the individual spectra realizations above, and the details within the RFFT and CTF graphs are accentuated. For figures 14 and 15: (a) is the RFFT graph, (b) is a plot of the CTF and corresponding pre-sampled MTF, and (c) are cropped images of the in-plane reconstructions for the quadrants being analyzed. The blue arcs in (c) indicate the LSR, measured at 5% modulation.

The 0-radian quadrant, f_x, of NGT-X shows evidence of super-resolution and residual aliasing artifacts (Fig. 14a-b). It is important to note that f_x is parallel to the x-ray source motion for NGT-X. The RFFT graph (Fig. 14a) shows the spine of ν, the spine of the square-wave harmonic, and spines of residual spectral leakage arising from ξ and d_{el}. The prominence of spectral leakage is diminished, and super-resolution is observed in the image reconstruction. The fundamental frequency is essentially the only frequency with significant modulation. As a result, the image reconstruction accurately portrays ν for modulation above ξ. The CTF Fig. 14b is normalized at 1.27 lp/mm using the modulation of the MTF at the same resolution. Like the pre-sampled MTF, the CTF shows modulation up to the Nyquist frequency of the detector. The image in Fig. 14c shows the 0-radian quadrant of the reconstructed star pattern, and the blue line indicates the LSR measured at 5% modulation.

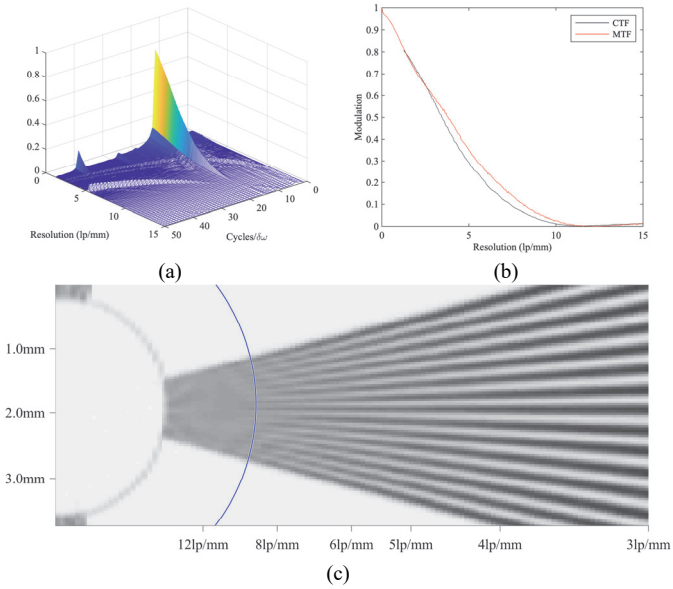

Fig. 14. Results for NGT-X f_x in the 0-radian quadrant of the star pattern. The RFFT graph (a), CTF plot (b), and image with the LSR (c) are shown. The input frequency, ν, and square wave harmonic are the only dominant signals in (a). The LSR is evident in the CTF plot near 9 lp/mm where modulation is 5%.

The π/2-radian quadrant contains f_y, which are aligned perpendicular to x-ray source motion for NGT-X. The results for this orientation are represented in Fig. 15. The RFFT graph (Fig. 15a) shows the same spines of the fundamental frequency and the square-wave harmonic as before. In contrast to f_x (Fig. 14a) however, spectral leakage, arising from d_{el}, is prominent for f_y. The spine of spectral leakage has higher modulation for frequencies above and below, ξ (the intersection at ν). The CTF (Fig. 15b) shows characteristic oscillatory behavior at the same location and is determined as the LSR, due to aliasing. The image (Fig. 15c) shows Moiré patterns for frequencies above and below ξ. The oscillatory behavior in the CTF and the Moiré patterns in the image reconstructions repeat according to the detector's pixels (n), described by (3):

$$M(n) = \frac{\xi}{n} \tag{3}$$

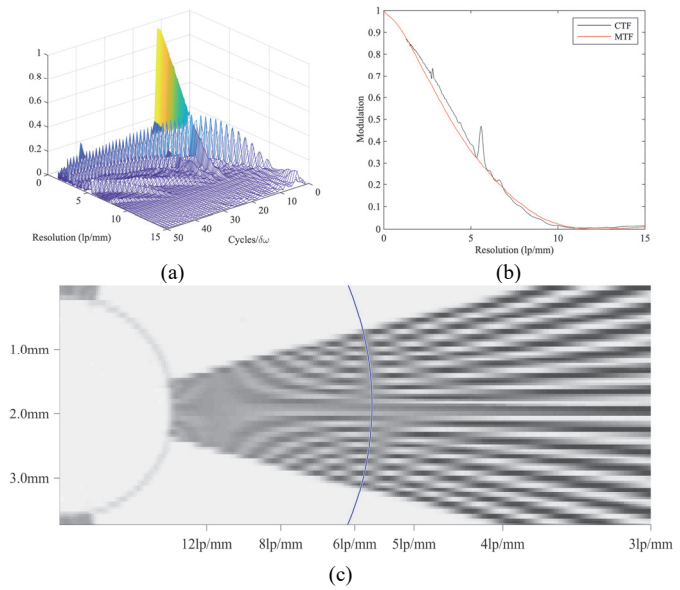

Fig. 15. Results for f_y of NGT-X. The RFFT graph (a) is similar to Fig. 14a, but shows significant spectral leakage. The spectral leakage intersects ν at ξ. This result is reflected in the CTF plot (b). Image (c) shows ξ as the LSR.

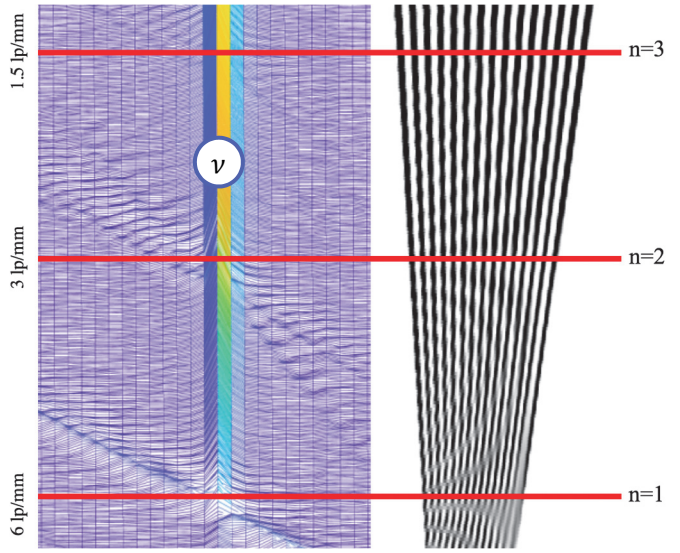

Fig. 16. Depiction of the RFFT graph from an aerial perspective alongside the corresponding star pattern quadrant with repeating Moiré patterns. The integer value n corresponds to (3). The repeating oscillations are observed in Fig. 15b.

The repetition of the Moiré patterns and how they correspond to the RFFT graph are depicted in Fig. 16 by viewing the RFFT graph from an aerial perspective next to its corresponding quadrant in the image reconstruction. This figure portrays ν vertically from top to bottom. The spectral leakage appears as the diagonal ripples that intersect the fundamental frequency at three locations. This first occurs near 6 lp/mm, which is 1/2 cycles per pixel (n =1). Residual peaks of spectral leakage then repeat at integer values of n: 3 lp/mm (1/4 cycles per pixel, n=2) and at 1.5 lp/mm (1/6 cycles per pixel, n=3).

IV. Discussion

The RFFT metric has been shown to identify aliasing in the form of spectral leakage for the two factors, d_{el} and λ, of a digital x-ray image. It can also distinguish differences between acquisition geometries. For these reasons, it is particularly useful for tomosynthesis. It is independent of orientation because of the radial implementation; therefore, no correction is required for non-zero values of ϕ. The results suggest that this method can be adapted for star pattern test objects with different resolution properties.

A. Determination of Sampling Rate for RFFT

The sample size (N) that was used in the RFFT calculation was sufficient for the images that we analyzed. If λ were to increase, it is possible that N would also need to increase. The absolute difference between condition A and D decreases as the resolution increases. Condition A is below Ξ at the lowest resolution of the star pattern. The absolute difference between any of the conditions with Γ values above 2.0 was as low as 10^{-15}. This supports the notion that the RFFT should not be computed for any Γ below Ξ.

B. 2D RFFT for NGT System

The average spectra of the 2D projections does not show a significant noise floor in the same manner as the individual projection. Aliasing is evident in the form of spectral leakage that arises from d_{el}, but the spectral leakage that arises from λ intersects ν at Ξ. The aperture spectral leakage is greater for f_y than for f_x. This may be due to the non-isometric focal spot size of the x-ray source.

C. 3D RFFT for Various Reconstruction Pitch Values

The various reconstruction sizes provide insight into proper sampling techniques for tomosynthesis image reconstructions. In order to achieve super-resolution, λ needs to be at least or greater than Ξ. The λ of 37μm appears to have the least prominent residual spectral leakage in Fig. 13. This suggests that it is advantageous to sample a tomosynthesis reconstruction at a λ that is not an integer multiple of d_{el}, like 42.5 μm (2.0x) or 28.3 μm (3.0x).

I. Conclusion

In this work, we demonstrate the Radial FFT metric using two frequency orientations for a 2D image and a 3D image reconstruction slice. The Radial FFT metric successfully compared resolution properties of all conditions. It separates the frequencies of spectral leakage (arising from d_{el} and λ) from fundamental input frequencies in 2D images and 3D image reconstructions. The Radial FFT metric produces the CTF of an in-plane image reconstruction without suppressing spectral leakage through super-sampling. The CTF is a more detailed representation of in-plane resolution properties and imaging artifacts for tomosynthesis than the corresponding pre-sampled MTF. The conceptual change in viewpoint, from the spatial-frequency domain to the Fourier domain, provides additional details of image quality: aliasing, square-wave response, and limiting spatial-resolution. The Radial FFT metric will be used to evaluate resolution properties for all acquisition geometries of the NGT prototype. The tools and instructions for this metric were created using MATLAB, and are made available online

at: [].

REFERENCES

[1] E. F. Conant, “Clinical Implementation of Digital Breast Tomosynthesis,” *Radiol. Clin. North Am.*, vol. 52, no. 3, pp. 499–518, 2014.

[2] R. J. Acciavatti and A. D. A. Maidment, “Observation of super-resolution in digital breast tomosynthesis,” Med. Phys., vol. 39, no. 12, pp. 7518–7539, 2012.

[3] T. L. Vent, R. J. Acciavatti, Y. J. Kwon, and A. D. A. Maidment, “Quantification of resolution in multiplanar reconstructions for digital breast tomosynthesis,” in Medical Imaging 2016: Physics of Medical Imaging, 2016, vol. 9783, p. 978303.

[4] C. J. Choi, T. L. Vent, A. D. A. Maidment, and R. J. Acciavatti, “Geometric calibration for a next-generation digital breast tomosynthesis system using virtual line segments,” Med. Imaging 2018 Phys. Med. Imaging, no. March, p. 12, 2018.

[5] T. D. Maidment, T. L. Vent, W. S. Ferris, D. E. Wurtele, R. J. Acciavatti, and A. D. A. Maidment, “Comparing the imaging performance of computed super resolution and magnification tomosynthesis,” in Medical Imaging 2017: Physics of Medical Imaging, 2017, vol. 10132, p. 1013222.

[6] R. J. Acciavatti and A. D. A. Maidment, “Oblique reconstructions in tomosynthesis. II. Super-resolution,” Med. Phys., vol. 40, no. 11, pp. 1–19, 2013.

[7] T. L. Vent, B. L. Lepore, and A. D. A. Maidment, “Evaluating the imaging performance of a next-generation digital breast tomosynthesis prototype,” Med. Imaging 2019 Phys. Med. Imaging, no. March, p. 19, 2019.

[8] J. Kuo, P. A. Ringer, S. G. Fallows, P. R. Bakic, A. D. A. Maidment, and S. Ng, “Dynamic reconstruction and rendering of 3D tomosynthesis images,” vol. 796116, no. March 2011, p. 796116, 2011.

[9] M. IEC, “IEC 62220-1-2:2007,” IEC. [Online]. Available: https://webstore.iec.ch/publication/6598. [Accessed: 12-Feb-2019].

[10] J. E. Eben, T. L. Vent, C. J. Choi, S. Yarrabothula, L. Chai, M. Nolan, E. Kobe, R. J. Acciavatti, and A. D. A. Maidment, “Development of a next generation tomosynthesis system,” in Progress in Biomedical Optics and Imaging - Proceedings of SPIE, 2018, vol. 10573.

[11] B. Barufaldi, T. L. Vent, E. P. Wileyto, A. D. A. Maidment, and R. J. Acciavatti, “Personalization of x-ray tube motion in digital breast tomosynthesis using virtual Defrise phantoms,” Med. Imaging 2019 Phys. Med. Imaging, no. March, p. 10, 2019.

[12] W. S. Ferris, T. L. Vent, T. D. Maidment, R. J. Acciavatti, D. E. Wurtele, and A. D. A. Maidment, “Geometric calibration for a next-generation digital breast tomosynthesis system,” in Medical Imaging 2017: Physics of Medical Imaging, 2017, vol. 10132, p. 101324C.

[13] J. W. Coltman, “The Specification of Imaging Properties by Response to a Sine Wave Input,” J. Opt. Soc. Am., vol. 44, no. 6, p. 468, 1954.

[14] E. Samei, M. J. Flynn, and D. A. Reimann, “A method for measuring the presampled MTF of digital radiographic systems using an edge test device A method for measuring the presampled MTF of digital radiographic systems using an edge test device a…,” Med. Phys. Med. Phys, vol. 25, no. 913, pp. 102–113, 1998.

[15] H. Fujita, K. Ueda, J. Morishita, T. Fuiikawa, A. Ohtsuka, and T. Sai, “Basic imaging properties of a computed radiographic system with photostimulable phosphors,” Med. Phys., vol. 16, no. 1, pp. 52–59, 1989.

[16] S. N. Friedman and I. A. Cunningham, “Normalization of the modulation transfer function: The open-field approach,” Med. Phys., vol. 35, no. 10, pp. 4443–4449, 2008.

Proposing Rapid Source Pulsing for Improved Super-Resolution in Digital Breast Tomosynthesis

Raymond J. Acciavatti[1], Trevor L. Vent[1], Bruno Barufaldi[1], E. Paul Wileyto[2],
Peter B. Noël[1], Andrew D. A. Maidment[1]
[1]University of Pennsylvania, Department of Radiology, 3400 Spruce Street, Philadelphia PA 19104
[2]University of Pennsylvania, Department of Epidemiology, Biostatistics, & Informatics,
423 Guardian Drive, Philadelphia, PA 19104
E-mail: {Raymond.Acciavatti | Trevor.Vent | Bruno.Barufaldi | epw |
Peter.Noel | Andrew.Maidment}@pennmedicine.upenn.edu

ABSTRACT

Our previous work showed that digital breast tomosynthesis (DBT) systems are capable of super-resolution, or subpixel resolution relative to the detector. Using a bar pattern phantom, it is possible to demonstrate that there are anisotropies in super-resolution throughout the reconstruction. These anisotropies are lessened in acquisition geometries with narrow spacing between source positions. This paper demonstrates that by re-arranging the source positions in the scan, the anisotropies can be minimized even further. To this end, a theoretical model of the reconstruction of a high-frequency sinusoidal test object was developed from first principles. We modeled the effect of clustering additional source positions around each conventional source position in fine increments (submillimeter). This design can be implemented by rapidly pulsing the source during a continuous sweep of the x-ray tube. It is shown that it is not possible to eliminate the anisotropies in a conventional DBT system with uniformly-spaced source positions, even if the increments of spacing are narrower than those used clinically. However, super-resolution can be achieved everywhere if the source positions are re-arranged in clusters with submillimeter spacing. Our previous work investigated a different approach for optimizing super-resolution through the use of detector motion perpendicular to the breast support. The advantage of introducing rapid source pulsing is that detector motion is no longer required; this mitigates the need for a thick detector housing, which may be cumbersome for patient positioning.

Keywords: Digital Breast Tomosynthesis, Mammography, Super-Resolution, Aliasing, Fourier Transform, Digital Imaging, Image Quality, Image Reconstruction.

1. INTRODUCTION

1.1 Review of Previous Work

Our previous work showed that it is possible to improve the visualization of subtle findings in digital breast tomosynthesis (DBT), such as calcifications, based on the principle of super-resolution.[1,2] This can be demonstrated with a bar pattern phantom. By preparing a DBT reconstruction with finer pixelation than the detector, we found that test frequencies exceeding the alias frequency of the detector can be resolved.

We have also shown that super-resolution in DBT is not achieved uniformly throughout the image.[2,3] There are anisotropies in regularly-spaced increments (z), corresponding to various slices in the reconstruction. These anisotropies can be visualized with a clinical DBT system by using a goniometry stand to angle a bar pattern phantom in an oblique plane. In our previous work, the reconstruction plane was tilted to match this angle.[3] This setup allowed for assessment of image resolution over a continuous range of z-coordinates (distance perpendicular to the breast support).

With theoretical modeling, we also analyzed how the number of anisotropies is dependent on the angular range of the scan. In a wide-range DBT scan, there are more anisotropies in a given volume.[3] This idea can be illustrated with an oblique reconstruction of the bar pattern phantom described previously (Figures 1-2). For these experiments, we used the Selenia Dimensions system (Hologic Inc., Bedford, MA, USA) with 15 projections, and we considered a test frequency of 5.0 mm^{-1}, since this exceeds the alias frequency (3.6 mm^{-1}) of the Hologic detector with 0.140 mm pixelation. Reconstructions were created with different subsets of projections, varying in terms of the spacing between

Medical Imaging 2020: Physics of Medical Imaging, edited by Guang-Hong Chen, Hilde Bosmans, Proc. of SPIE
Vol. 11312, 113125G · © 2020 SPIE · CCC code: 1605-7422/20/$21 · doi: 10.1117/12.2542551

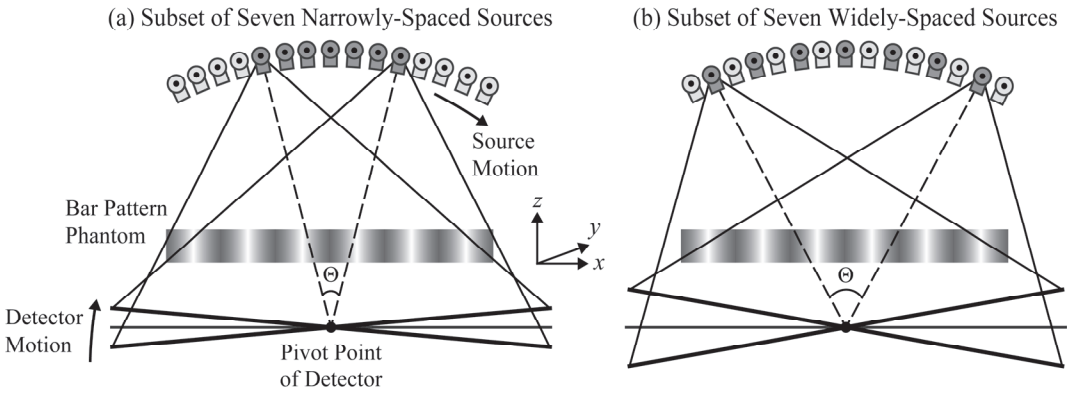

Figure 1. Shown are two different subsets of seven projections (dark grey), varying in terms of spacing between source positions.

source positions. The subset of seven projections with 1.07° spacing was analyzed as a surrogate for a narrow-range DBT scan [Figure 1(a)], while the subset of seven projections with 2.14° spacing was analyzed as a surrogate for a wide-range DBT scan [Figure 1(b)].

The reconstructions were prepared with Piccolo™ (Real Time Tomography, LLC, Villanova, PA), a software that allows the user to tilt the reconstruction plane to match the plane of the bar pattern phantom.[4] Super-resolution is not achieved everywhere; the aliasing artifacts are denoted by the arrows (Figure 2). There are more anisotropies in the acquisition with the wider angular range. More specifically, in the *z* direction, there is 6 mm spacing between anisotropies in the scan with 1.07° spacing between projections [Figure 2(a)], and there is 3 mm spacing between anisotropies in the scan with 2.14° spacing between projections [Figure 2(b)].

1.2 Overview of Anti-Aliasing Strategies

This paper explores how many of the anti-aliasing strategies that guided the evolution of computed tomography (CT) scanners can be applied to the design of DBT systems. One such strategy is focal spot wobble.[5] This strategy has been used in some third-generation CT scanners. After the gantry has rotated by half of a pixel, the x-ray source position is translated back half of a pixel, so that pairs of rays are created with the same source position but where the detector location differs by half the detector's width. This effectively doubles the sampling rate and provides anti-aliasing. This paper demonstrates that a similar strategy can be applied to DBT; however, here the detector position is stationary and the x-ray source is moved by approximately half a detector element referenced to the mid-plane of the breast. Specifically, we show that introducing fine (submillimeter) motions of the source between projections results in an improvement in resolution, and aliasing artifacts are eliminated. Anisotropies are no longer present throughout the reconstruction.

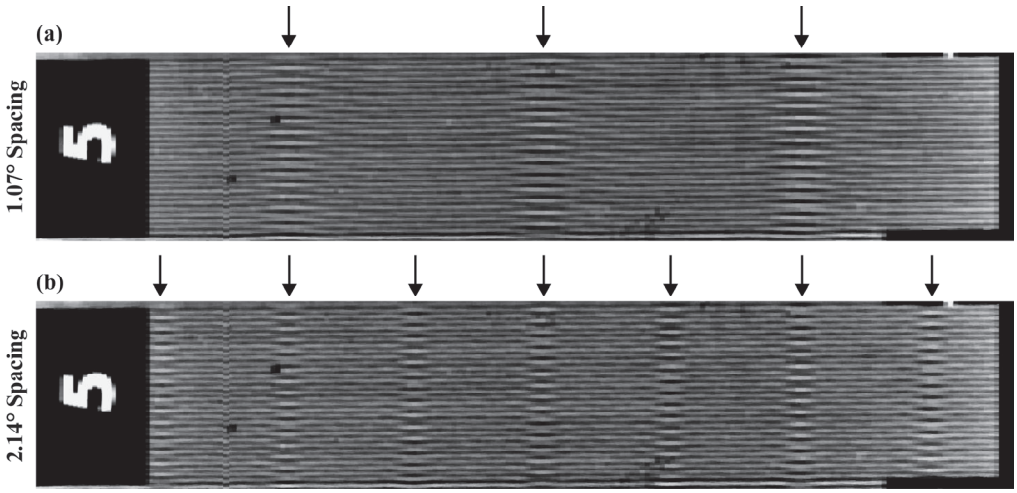

Figure 2. There are fewer aliasing artifacts (denoted by the arrows) in the scan with narrowly-spaced source positions.

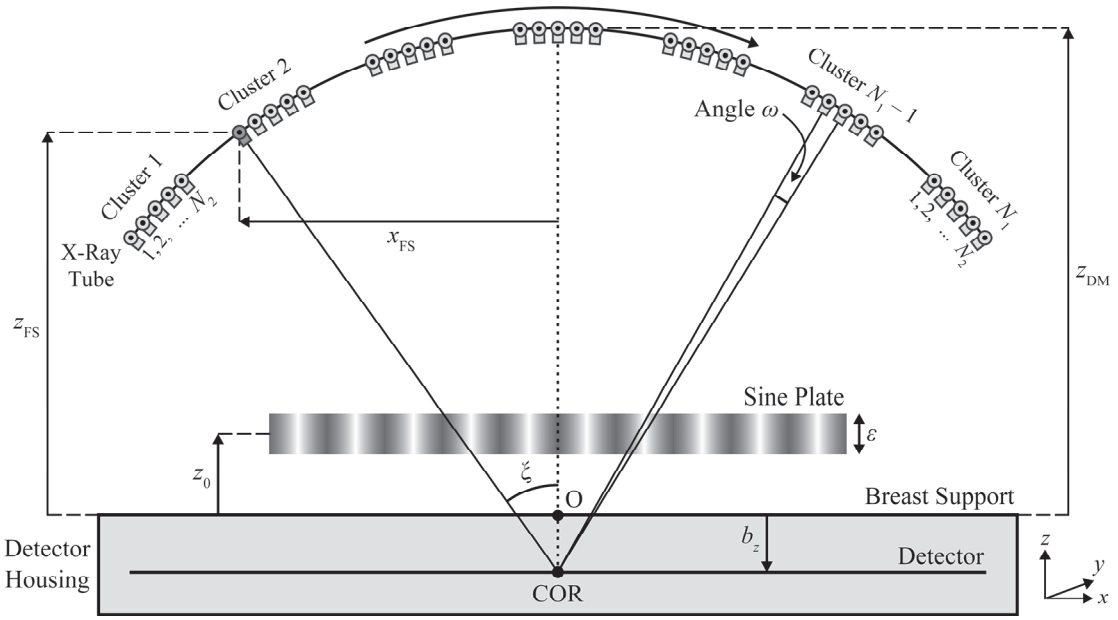

Figure 3. A DBT system design with clustered source positions is modeled. The parameter N_1 controls the number of clusters, while the parameter N_2 controls the number of source positions per cluster. In this example, $N_1 = 7$ and $N_2 = 5$.

Another strategy for improving resolution and hence reducing aliasing in CT is to increase the number of projections. The minimum number of projections needed to avoid aliasing can be understood from the formula

$$N_{\min} = \frac{4\pi R \nu_M}{1 - \sin(\psi / 2)}, \tag{1}$$

where ν_M is frequency, ψ is fan angle, and R is the radius over which the frequency ν_M can be resolved without aliasing, assuming source rotation over a 360° arc.[6] This paper demonstrates that in DBT, there is also a resolution gain achieved by increasing the number of projections. Although the DBT system is modeled with a larger number of projections than those used clinically, the radiation dose per projection can be reduced so that the total dose of the scan is unchanged.

2. METHODS

2.1 Simulated Acquisition Geometry

In clinical DBT systems, the source rotates in a circular arc in the chest-wall plane, and the projection images are acquired at a constant angular spacing.[7,8] In this paper, we re-arrange the source positions in clusters (Figure 3). Within each cluster, there is very fine (submillimeter) spacing between source positions; this spacing is denoted by the angle ω. We assume that there are N_1 clusters and N_2 positions per cluster. Hence the total number of projections (N_t) is given by the product

$$N_t = N_1 \times N_2 . \tag{2}$$

The center-of-rotation (COR) of the source motion is treated as the midpoint of the detector. The detector is taken to be stationary during the scan, unlike the Selenia Dimensions system (Figure 1). The source coordinate (x_{FS}, y_{FS}, z_{FS}) at an arbitrary point in the arc can be written in terms of the projection angle ξ.

$$x_{FS} = (z_{DM} - b_z)\sin\xi , \quad y_{FS} = 0 , \quad z_{FS} = (z_{DM} - b_z)\cos\xi + b_z \tag{3}$$

The origin of this coordinate system (point O) is the midpoint of the breast support directly above the COR (at distance b_z). Also, z_{DM} denotes the z-coordinate of the central source position; the subscript "DM" emphasizes that this source position is the same as the one used in digital mammography, the conventional 2D modality for breast cancer screening. The y-coordinate of the source (not shown in Figure 3) is zero for all projections, since there is no source motion perpendicular to the chest-wall plane (into the plane of the page).

Table 1. The simulation parameters for the test object and acquisition geometry are summarized below.

Parameter	Value
Distance z_{DM}: Breast Support to Source	625.0 mm
Distance b_z: Breast Support to Detector	–25.0 mm
N_t: Total Number of Projections	60
Increment ω: Angular Spacing	0.05°
Detector Pixel Size	0.085 mm × 0.085 mm
Thickness (ε) of Test Object	0.50 mm
Frequency of Test Object	8.0 mm^{-1}
Fourier Sampling: J_{FT}	1,000
x''_{min}: Lower Endpoint of Fourier Transform	–3.125 mm
x''_{max}: Upper Endpoint of Fourier Transform	3.125 mm

Going from left to right in Figure 3, each source position can be numbered with an integer (n) between 1 and N_t. Assuming that there is equal spacing between clusters, it can be shown that

$$\xi = \frac{\left(2n' - N_1 - 1\right)\left[\Theta - \omega\left(N_2 - 1\right)\right]}{2\left(N_1 - 1\right)} + \left(n'' - \frac{N_2 + 1}{2}\right)\omega\,, \tag{4}$$

where Θ denotes the total angular range of the scan (Figure 1) and where

$$n' = 1 + \left\lfloor \frac{n-1}{N_2} \right\rfloor, \quad n'' = n - N_2 \left\lfloor \frac{n-1}{N_2} \right\rfloor, \quad \lfloor v_1 \rfloor \equiv \max\left\{v_2 \in \mathbb{Z} : v_2 \le v_1\right\}. \tag{5}$$

In Eq. (5), the symbol $\lfloor\ \rfloor$ denotes the floor function.

2.2 Theoretical Model of Super-Resolution

In our previous work, we modeled the reconstruction of a sine plate to analyze super-resolution (Figure 3).[3] This object is a thin rectangular prism (thickness ε) with a sinusoidal attenuation coefficient, μ. In this paper, the simple backprojection (SBP) reconstruction of this object is analyzed in an acquisition geometry based off the "next-generation" tomosynthesis (NGT) system, a DBT system constructed for research use at the University of Pennsylvania (Table 1).[9]

For analysis of super-resolution, a test frequency of 8.0 mm^{-1} is chosen, since this frequency is higher than the alias frequency of the detector (5.9 mm^{-1}) used in the NGT system. To determine how well the input frequency is resolved, the Fourier transform of the reconstruction (μ_{SBP}) is calculated with the midpoint formula for integration

$$\mathcal{F}_1\mu_{SBP} \approx \left(\frac{x''_{max} - x''_{min}}{J_{FT}}\right)\sum_{j_{FT}=1}^{J_{FT}} \mu_{SBP} e^{-2\pi i f_x'' x''}\Big|_{x''=x''_{min}+(x''_{max}-x''_{min})\left(\frac{j_{FT}-1/2}{J_{FT}}\right)}, \tag{6}$$

where x'' is position measured in the x direction relative to the point of interest, x''_{min} and x''_{max} are the integration limits, and J_{FT} is the number of samples.

The r-factor, a metric proposed in our previous work, is calculated to summarize the results in Fourier space.[2,3] To illustrate this metric in the conventional acquisition geometry ($\Theta = 20°$, $N_t = 15$), reconstructions at two z-coordinates in the chest-wall plane are shown (Figure 4). At the coordinate demonstrating super-resolution [Figure 4(a)-(b)], the Fourier transform has a major peak at the input frequency, 8.0 mm^{-1}. By contrast, at the coordinate exhibiting aliasing [Figure 4(c)-(d)], the major peak is at a lower frequency (4.3 mm^{-1}). The r-factor is the ratio of the amplitude of the highest peak less than the alias frequency (5.9 mm^{-1}) to the amplitude at the input frequency (8.0 mm^{-1}); *i.e.*, the ratio of the amplitudes A_1 to A_2.

$$r\text{-Factor} = \frac{A_1}{A_2} \tag{7}$$

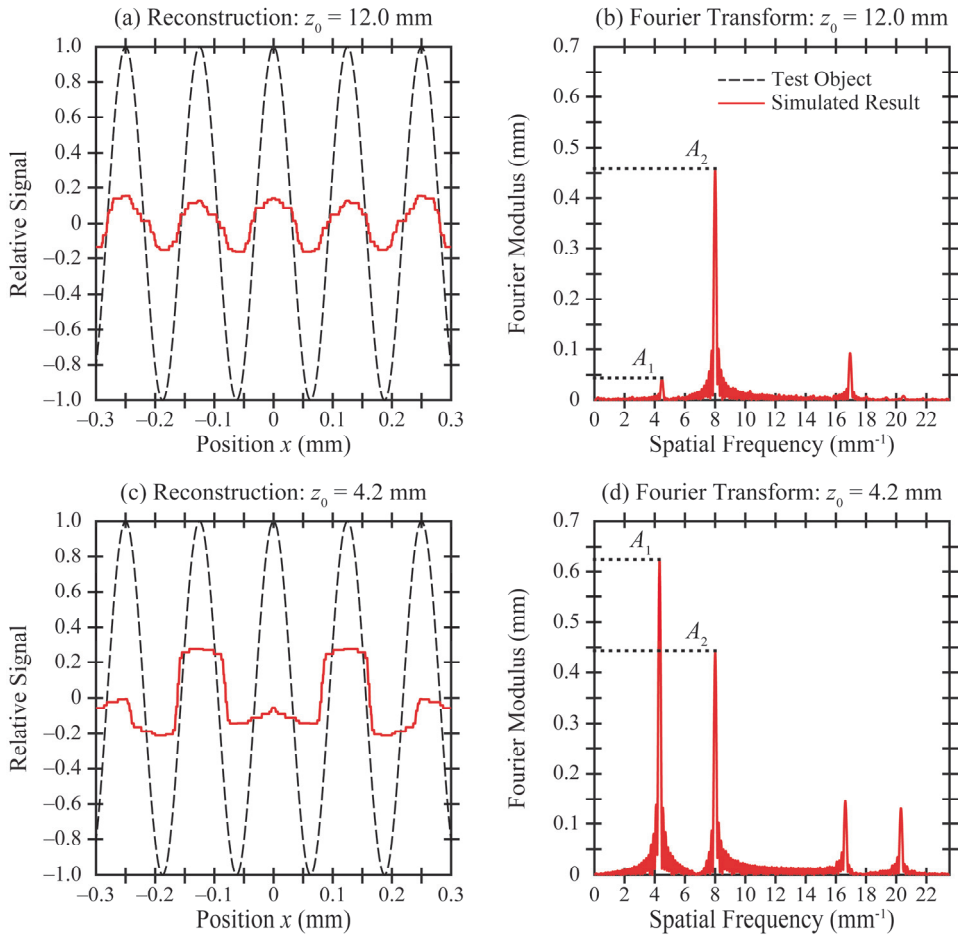

Figure 4. In the conventional acquisition geometry ($\Theta = 20°$, $N_t = 15$), the ability to achieve super-resolution is dependent on the z_0-coordinate of the object. Two z_0-coordinates are shown here as examples. In order for super-resolution to be achieved with high quality, the ratio of amplitudes A_1 to A_2 (r-factor) in Fourier space should be as small as possible.

In these two examples, the r-factor is 0.096 at the position demonstrating super-resolution [Figure 4(b)], and is 1.4 at the position exhibiting aliasing [Figure 4(d)]. In order for super-resolution to be achieved with high quality, the r-factor should be as small as possible (approaching zero). For the purpose of this paper, we set this threshold as: r-factor < 1/3. That is, the amplitude A_2 should be at least three times higher than the amplitude A_1.

2.3 Statistical Calculations

To quantify the variation in the r-factor throughout the reconstruction volume, 1,000 randomly-sampled points are analyzed in a volume-of-interest (VOI). The VOI is a rectangular prism with dimensions 200.0 × 100.0 × 50.0 (in mm) and 0.020 mm spacing between points in each direction; the VOI is taken to be centered on the point (0, 50.0, 25.0) (in mm). From the histogram obtained from 1,000 points [Figure 5(a)], the proportion of points for which r-factor < 1/3 is calculated.

Next, the VOI is analyzed with bootstrapping. From the histogram of 200 re-samplings of the proportion of points with high-quality super-resolution, the middle 95% is used to calculate a 95% confidence interval. For example, in the acquisition geometry described previously, the 95% confidence interval for this proportion ranges between 0.607 and 0.665 [Figure 5(b)].

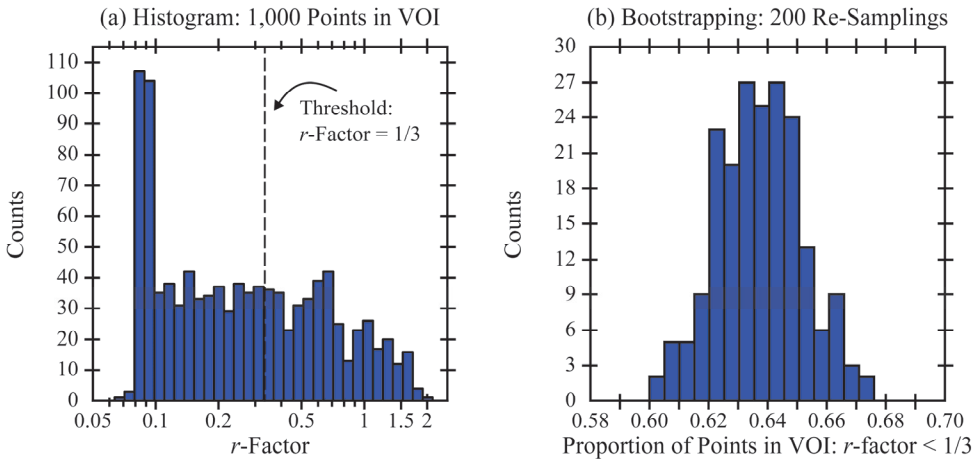

Figure 5. (a) In the conventional acquisition geometry ($\Theta = 20°$, $N_t = 15$), the *r*-factor varies between 0.067 and 1.92 in the histogram of 1,000 randomly-sampled points in the VOI. (b) The proportion of points in the VOI with high-quality super-resolution is calculated by introducing a threshold (*r*-factor < 1/3). Based on 200 bootstrapped re-samplings of this proportion, the 95% confidence interval varies between 0.607 and 0.665.

3. RESULTS

3.1 Super-Resolution in the Next-Generation System Design

First, an acquisition geometry with a 30° scanning range and 60 projections is simulated (Figure 6). In a conventional system with uniformly-spaced source positions ($N_2 = 1$), there are sharp peaks in the *r*-factor in the range $z = 0$ to 50.0 mm [Figure 6(a)]. These peaks correspond to the positions at which super-resolution is not achievable. In our previous work, we showed that increasing the number of projections is beneficial in terms of minimizing the number of anisotropies.[3] Even with the use of 60 projections (well above the number used clinically), the anisotropies are unavoidable in the conventional acquisition geometry.

The anisotropies can be suppressed by re-designing the acquisition geometry with clustered source positions [Figures 6(b)-(f)]. It is beneficial to cluster as many source positions together as possible; *i.e.*, to increase the value of N_2. This decreases the maximum amplitude of the *r*-factor; it ensures that the *r*-factor is well below unity at every position.

3.2 Statistical Calculations

Next, the VOI is analyzed in terms of the proportion of points with high-quality super-resolution (Figure 7). In the case of the conventional acquisition geometry ($N_2 = 1$), the proportion is highest in a narrow-range DBT scan ($\Theta = 10°$). As the angular range increases to 30°, the proportion is degraded. This illustrates the drawback of wide-range DBT; fewer points in the VOI achieve super-resolution with high quality.

As the value of N_2 increases, the proportion of points with high-quality super-resolution approaches unity, and there is effectively no difference between the three scanning ranges (10°, 20°, and 30°). This demonstrates that a wide-range DBT scan can indeed be optimized for super-resolution.

4. DISCUSSION AND CONCLUSION

In DBT, there are benefits and drawbacks to the use of a wide angular range. For example, we previously considered the task of segmenting the 3D breast outline in the reconstruction; this is determined based on the detector pixels that fall outside the shadow of the breast in each projection.[10] This task is optimized with a wide-range DBT scan. Additionally, previous work has shown that there are improvements in resolving the spacing between objects in the *z* direction, which can benefit masses.[11,12]

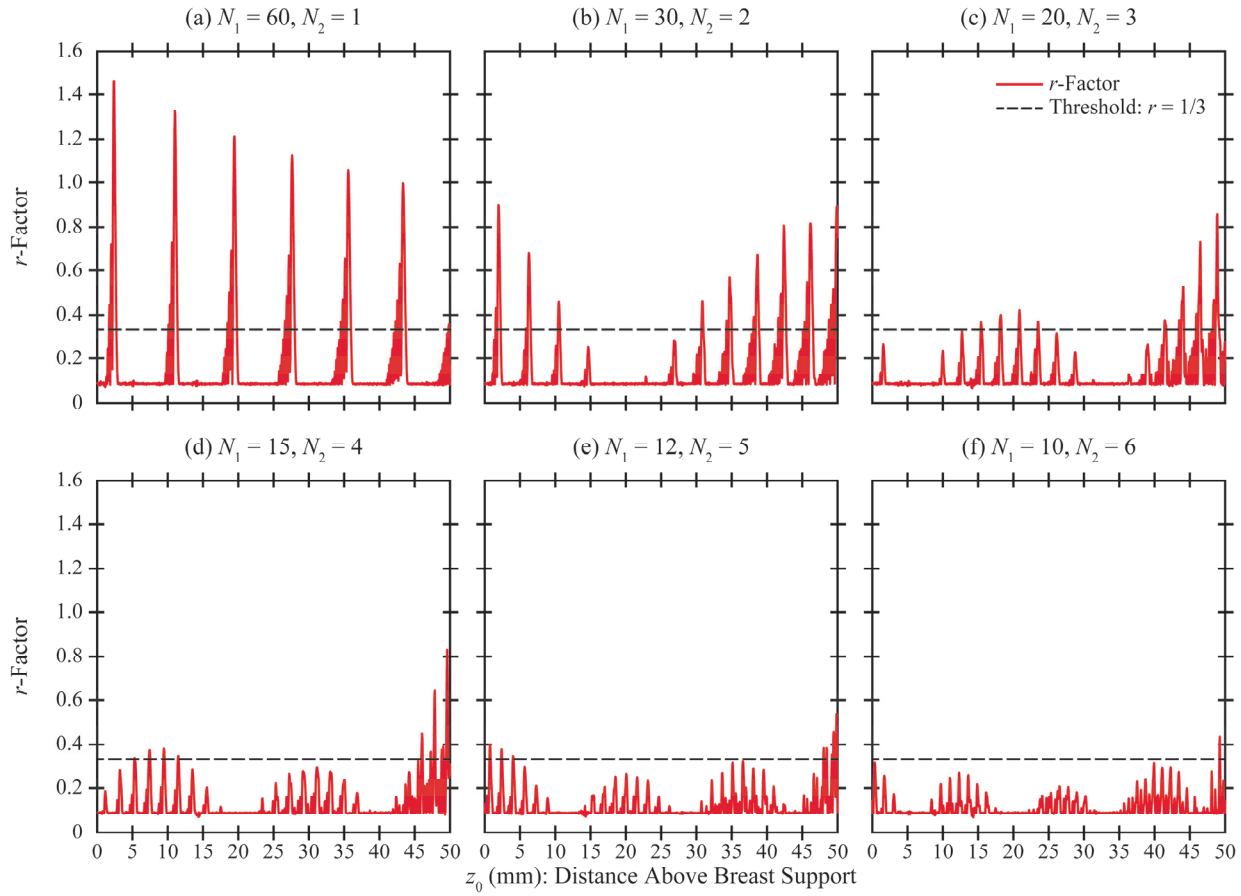

Figure 6. As N_2 increases, the maximum amplitude of the *r*-factor decreases. Therefore, in order for super-resolution to be achieved uniformly throughout the image with high quality, the source positions should be clustered together as much as possible (in this example, with 0.05° spacing).

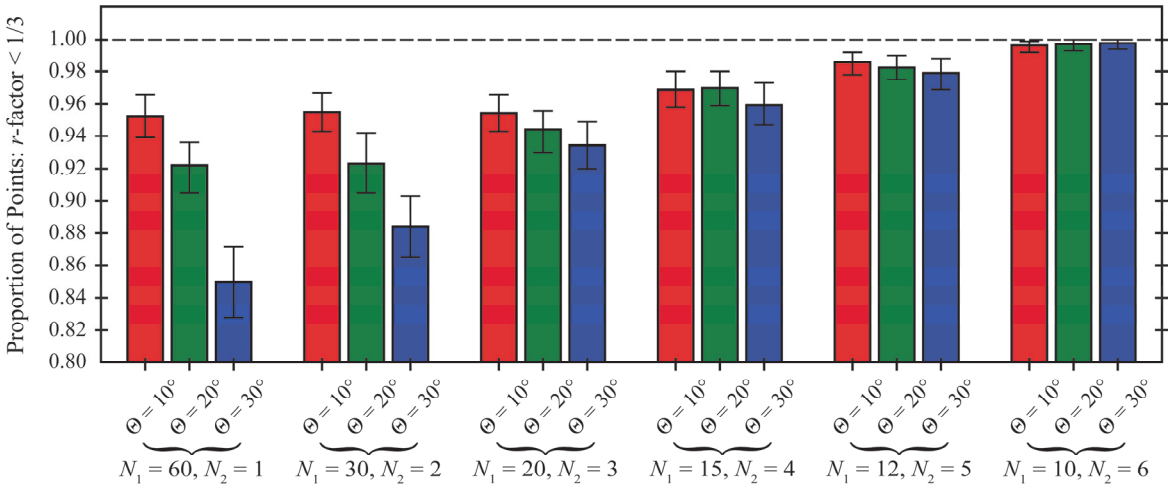

Figure 7. As N_2 increases, there are more points in the VOI at which super-resolution is achieved with high quality (*r*-factor < 1/3). The error bars denote 95% confidence intervals for the proportion.

Despite these benefits, there are other tasks, such as imaging calcifications, for which a narrow angular range is advantageous. For example, according to the study by Chan *et al*., the detectability and conspicuity of calcifications are poorer at large scan angles.[13] In this paper, we consider the task of achieving super-resolution; this task is complementary to imaging calcifications, which are high-frequency structures. In a wide-range DBT scan, we show that there is closer spacing between anisotropies, and hence there are more positions at which super-resolution is not feasible (Figures 1-2).

By increasing the number of projections, there are fewer anisotropies in a given volume.[3] However, even with the use of 60 projections (well above the number that would typically be used clinically), it is not possible to eliminate the anisotropies entirely [Figure 6(a)]. With theoretical modeling, we demonstrate the advantage of re-arranging the source positions in clusters in submillimeter increments ($\omega = 0.05°$), as could be achieved by rapidly pulsing the source during a continuous sweep of the x-ray tube. With this design, the anisotropies are eliminated. In order for this design to be implemented in practice, the detector would need to be capable of a high frame rate, and the radiation dose per projection would need to be reduced so that the total dose of the scan is unchanged.

Our previous work considered a different design for eliminating these anisotropies; specifically, the use of detector motion in the *z* direction (perpendicular to the breast support).[3] However, the trade-off of detector motion is that it may require a thicker detector housing, which is potentially cumbersome for patient positioning. By re-designing the source motion in the manner described in this paper, detector motion is no longer necessary to optimize super-resolution.

In future work, there are areas in which this theoretical model can be expanded. This paper presumes that there are no sources of detector blurring. However, previous works have shown that, in a divergent x-ray beam geometry, there is resolution loss due to non-normal x-ray incidence, and that this effect is pronounced at broad projection angles.[14-22] Future work should also analyze the effect of focal spot blurring during a continuous sweep of the x-ray tube[23,24]; this could potentially reduce the modulation of the sinusoidal waveform (Figure 4).

5. ACKNOWLEDGEMENT

We thank Johnny Kuo, Susan Ng, and Peter Ringer of Real Time Tomography (RTT) for technical assistance with Piccolo™. Andrew D. A. Maidment is a shareholder of RTT, and is a member of the scientific advisory board. Support was provided by the following grants: W81XWH-18-1-0082 from the Department of Defense Breast Cancer Research Program, IRSA 1016451 from the Burroughs Wellcome Fund, 1R01CA196528 from the National Institute of Health, and IIR13264610 from Susan G. Komen®. In addition, equipment support was provided by Analogic Inc., Barco NV, and RTT. The content is solely the responsibility of the authors and does not necessarily represent the official views of the funding agencies.

6. REFERENCES

1. Acciavatti RJ, Maidment ADA. Investigating the Potential for Super-Resolution in Digital Breast Tomosynthesis. Paper presented at: SPIE Medical Imaging2011; Lake Buena Vista, FL.
2. Acciavatti RJ, Maidment ADA. Observation of super-resolution in digital breast tomosynthesis. *Medical Physics.* 2012;39(12):7518-7539.
3. Acciavatti RJ, Wileyto EP, Maidment ADA. Modeling Acquisition Geometries with Improved Super-Resolution in Digital Breast Tomosynthesis. Paper presented at: SPIE Medical Imaging2016; San Diego, CA.
4. Kuo J, Ringer PA, Fallows SG, Bakic PR, Maidment ADA, Ng S. Dynamic Reconstruction and Rendering of 3D Tomosynthesis Images. Paper presented at: SPIE Medical Imaging2011; Lake Buena Vista, FL.
5. Hsieh J, Gard MA, Gravelle S. A Reconstruction Technique for Focal Spot Wobbling. Paper presented at: SPIE Medical Imaging1992; Newport Beach, CA.
6. Joseph PM, Schulz RA. View sampling requirements in fan beam computed tomography. *Medical Physics.* 1980;7(6):692-702.
7. Sechopoulos I. A review of breast tomosynthesis. Part I. The image acquisition process. *Medical Physics.* 2013;40(1):014301-014301 to 014301-014312.
8. Sechopoulos I. A review of breast tomosynthesis. Part II. Image reconstruction, processing and analysis, and advanced applications. *Medical Physics.* 2013;40(1):014302-014301 to 014302-014317.

9. Eben JE, Vent TL, Choi CJ, et al. Development of a Next Generation Tomosynthesis System. Paper presented at: SPIE Medical Imaging2018; Houston, TX.

10. Acciavatti RJ, Rodriguez-Ruiz A, Vent TL, et al. Analysis of Volume Overestimation Artifacts in the Breast Outline Segmentation in Tomosynthesis. Paper presented at: SPIE Medical Imaging2018; Houston, TX.

11. Mertelmeier T, Ludwig J, Zhao B, Zhao W. Optimization of Tomosynthesis Acquisition Parameters: Angular Range and Number of Projections. *Lecture Notes in Computer Science.* 2008;5116:220-227.

12. Zhao B, Zhao W. Three-dimensional linear system analysis for breast tomosynthesis. *Medical Physics.* 2008;35(12):5219-5232.

13. Chan H-P, Goodsitt MM, Helvie MA, et al. Digital Breast Tomosynthesis: Observer Performance of Clustered Microcalcification Detection on Breast Phantom Images Acquired with an Experimental System Using Variable Scan Angles, Angular Increments, and Number of Projections Views. *Radiology.* 2014;273(3):675-685.

14. Que W, Rowlands JA. X-ray imaging using amorphous selenium: Inherent spatial resolution. *Medical Physics.* 1995;22(4):365-374.

15. Hajdok G, Cunningham IA. Penalty on the detective quantum efficiency from off-axis incident x rays. Paper presented at: Medical Imaging 2004: Physics of Medical Imaging2004; San Diego, CA.

16. Mainprize JG, Bloomquist AK, Kempston MP, Yaffe MJ. Resolution at oblique incidence angles of a flat panel imager for breast tomosynthesis. *Medical Physics.* 2006;33(9):3159-3164.

17. Acciavatti RJ, Maidment ADA. Calculation of OTF, NPS, and DQE for Oblique X-Ray Incidence on Turbid Granular Phosphors. *Lecture Notes in Computer Science.* 2010;6136:436-443.

18. Hu Y-H, Scaduto DA, Zhao W. The Effect of Amorphous Selenium Thickness on Imaging Performance of Contrast Enhanced Digital Breast Tomosynthesis. *Lecture Notes in Computer Science.* 2012;7361:9-16.

19. Hu Y-H, Zhao W. The effect of amorphous selenium detector thickness on dual-energy digital breast imaging. *Medical Physics.* 2014;41(11):111904-111901 - 111904-111910.

20. Scaduto DA, Tousignant O, Zhao W. Experimental characterization of a direct conversion amorphous selenium detector with thicker conversion layer for dual-energy contrast-enhanced breast imaging. *Medical Physics.* 2017;44(8):3965-3977.

21. Acciavatti RJ, Maidment ADA. Non-stationary model of oblique x-ray incidence in amorphous selenium detectors: I. Point spread function. *Medical Physics.* 2019;46(2):494-504.

22. Acciavatti RJ, Maidment ADA. Nonstationary model of oblique x-ray incidence in amorphous selenium detectors: II. Transfer functions. *Medical Physics.* 2019;46(2):505-516.

23. Acciavatti RJ, Maidment ADA. Optimization of Continuous Tube Motion and Step-and-Shoot Motion in Digital Breast Tomosynthesis Systems with Patient Motion. Paper presented at: SPIE Medical Imaging2012; San Diego, CA.

24. Shaheen E, Marshall N, Bosmans H. Investigation of the effect of tube motion in breast tomosynthesis: continuous or step and shoot? Paper presented at: SPIE Medical Imaging2011; Lake Buena Vista, FL.

Robust Radiomic Feature Selection in Digital Mammography: Understanding the Effect of Imaging Acquisition Physics Using Phantom and Clinical Data Analysis

Raymond J. Acciavatti[1], Eric A. Cohen[1], Omid Haji Maghsoudi[1], Aimilia Gastounioti[1], Lauren Pantalone[1], Meng-Kang Hsieh[1], Emily F. Conant[1], Christopher G. Scott[2], Stacey J. Winham[2], Karla Kerlikowske[3], Celine Vachon[2], Andrew D. A. Maidment[1], Despina Kontos[1]
[1]University of Pennsylvania, Department of Radiology, 3400 Spruce Street, Philadelphia PA 19104
[2]Mayo Clinic, 200 First Street SW, Rochester MN 55905
[3]UCSF Women's Health Clinical Research Center, 550 16th Street, San Francisco CA 94143
E-mail: {Raymond.Acciavatti | Andrew.Maidment | Despina.Kontos}@pennmedicine.upenn.edu

ABSTRACT

Studies have shown that combining calculations of radiomic features with estimates of mammographic density results in an even better assessment of breast cancer risk than density alone. However, to ensure that risk assessment calculations are consistent across different imaging acquisition settings, it is important to identify features that are not overly sensitive to changes in these settings. In this study, digital mammography (DM) images of an anthropomorphic phantom ("Rachel", Gammex 169, Madison, WI) were acquired at various technique settings. We varied kV and mAs, which control contrast and noise, respectively. DM images in women with negative screening exams were also analyzed. Radiomic features were calculated in the raw ("FOR PROCESSING") DM images; i.e., grey-level histogram, co-occurrence, run length, fractal dimension, Gabor Wavelet, local binary pattern, Laws, and co-occurrence Laws features. For each feature, the range of variation across technique settings in phantom images was calculated. This range was scaled against the range of variation in the clinical distribution (specifically, the range corresponding to the middle 90% of the distribution). In order for a radiomic feature to be considered robust, this metric of imaging acquisition variation (IAV) should be as small as possible (approaching zero). An IAV threshold of 0.25 was proposed for the purpose of this study. Out of 341 features, 284 features (83%) met the threshold IAV $\leq$ 0.25. In conclusion, we have developed a method to identify robust radiomic features in DM.

Keywords: Radiomics, Digital Mammography, Robustness, Anthropomorphic Phantom, Risk Assessment, Breast Cancer.

1. INTRODUCTION

In digital mammography (DM), estimates of breast density can be complemented with radiomic feature calculations to provide an even better assessment of breast cancer risk than density alone.[1] The number of features used in these calculations is constantly growing, as new features continue to be introduced. However, having more features is not necessarily beneficial if many of the features are highly correlated with each other. Two examples of techniques that can be used to identify the uncorrelated features include cluster analysis and principal component analysis.[2-10]

In addition to these two techniques, previous works have also shown that features can be selected based on their robustness to imaging acquisition parameters. The goal is to identify features that are not overly sensitive to small variations in contrast, noise, and image sharpness. Instead, it is important to select features that capture underlying breast parenchymal patterns, which could be suggestive of breast cancer risk. One way to identify robust features is to consider their variation across vendors. In the work by Keller *et al*., robust features were identified by acquiring images of an anthropomorphic phantom with three DM systems.[11] Each image was *Z*-score normalized, and feature distributions across vendors were analyzed with equivalence tests. Keller *et al*. showed that histogram and structural features, such as fractal dimension, tended to be robust across vendors.

Medical Imaging 2020: Computer-Aided Diagnosis, edited by Horst K. Hahn, Maciej A. Mazurowski, Proc. of SPIE Vol. 11314, 113140W · © 2020 SPIE
CCC code: 1605-7422/20/$21 · doi: 10.1117/12.2549163

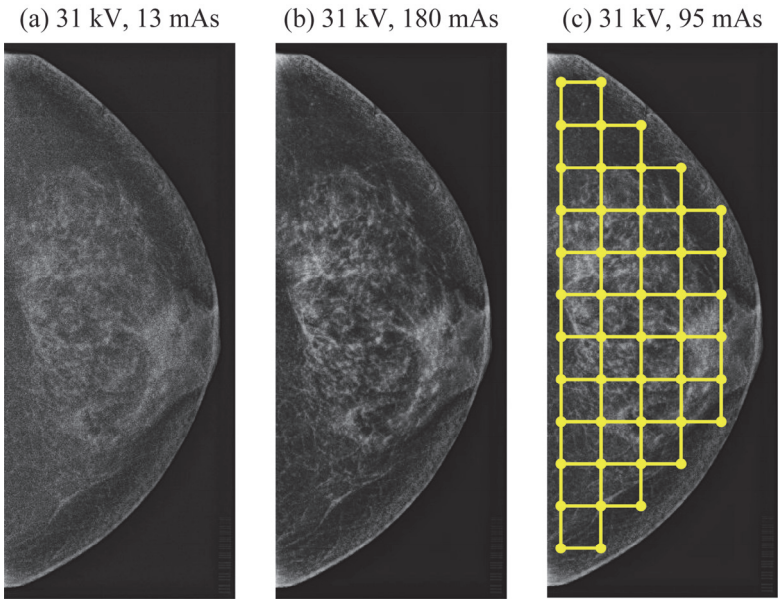

Figure 1. Increasing mAs reduces noise. The auto-time image in (c) illustrates the lattice used for radiomic feature calculations.

Alternatively, robust features can be identified based on clinical data; for example, more recently Mendel *et al*. analyzed data obtained from women imaged at different time points with different DM vendors.[12] Based on calculations of correlations across vendors, features describing spatial patterns were found to be robust; in accord with the work of Keller *et al*.[11], fractal dimension was included among the robust features. In a follow-up study, this analysis was applied in combination with hierarchical clustering to identify features that were both robust and non-redundant.[10]

In this paper, DM images of an anthropomorphic phantom are calculated at various technique settings (kV and mAs), and 341 radiomic features are analyzed in terms of their sensitivity to these settings. These two settings control the contrast and noise, respectively. Our method for identifying robust features is unique in that we analyze phantom data in combination with clinical data. Specifically, we measure how much the variation across technique settings scales against the variation seen in a negative screening population. In order for a feature to be considered robust, the variation across technique settings should be small. We propose a criterion for selecting robust features based on an analysis of sensitivity to changes in the technique settings.

2. METHODS

2.1 Phantom Image Acquisitions

DM images of an anthropomorphic phantom[13] ("Rachel", Gammex 169, Madison, WI) were acquired using a Selenia Dimensions system (Hologic Inc., Bedford, MA) with a W/Rh target-filter combination and cranial-caudal (CC) views (Figure 1). Multiple images were acquired at different technique settings. First, kV was varied (27 to 35 in increments of 1 kV) with mAs at each kV determined by auto-timing (Figure 2). Second, kV was fixed at 31 and mAs was varied from 13 to 180 mAs. The mAs increments were all varied approximately by a factor of $2^{1/2}$ based on the closest mAs setting supported by the system. Two images were acquired at each technique setting. The phantom was in the same position for all acquisitions.

2.2 Overview of Clinical Data Set

In addition, raw ("FOR PROCESSING") DM images of 1,000 women with negative screening exams between 9/1/14 and 12/31/14 were analyzed. These included 46% African American and 44% Caucasian women (in the remaining 10% of patients, ethnicity was unknown). The images were acquired at the Hospital of the University of Pennsylvania using Selenia Dimensions systems. This research was approved by the Institutional Review Board at the University of Pennsylvania and was compliant with the Health Insurance Portability and Accountability Act (HIPAA). Because the phantom is representative of a CC view, the clinical image analysis was restricted to CC views.

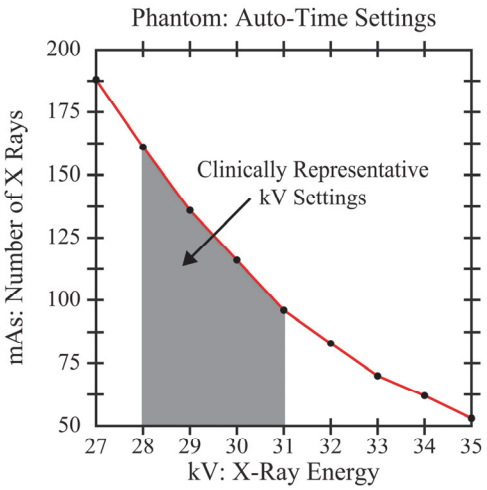

Figure 2. The mAs controls the number of x-ray photons. At high kV, there is greater x-ray penetration and hence mAs is reduced.

2.3 Radiomic Feature Extraction

The first step in radiomic feature extraction was to segment the breast area from background with LIBRA (Laboratory for Breast Radiodensity Assessment), an automated software tool.[14] From the raw ("FOR PROCESSING") DM images, 341 radiomic features were calculated. This included eight families of features: grey-level histogram, *i.e.*, 12 statistics derived from the histogram of the image; co-occurrence, *i.e.*, 7 measures of spatial relationships among grey levels; run length, *i.e.*, 7 measures of texture coarseness; fractal dimension, *i.e.*, 2 measures of self-similarity; local binary pattern (LBP), *i.e.*, 36 measures of intensity variation comparing a central pixel against its neighbors; Laws, *i.e.*, 125 grey-level histogram features derived from the convolution of the image with a 5 × 5 kernel; Co-occurrence Laws, *i.e.*, 120 co-occurrence features derived from the convolution of the image with a 5 × 5 kernel; and Gabor Wavelet, *i.e.*, 32 features measuring image details at different scales and orientations.[15-19]

From the raw ("FOR PROCESSING") DM images, these 341 features were calculated by partitioning the segmented breast area into a regular grid (lattice) of square windows [Figure 1(c)]. For a given feature, the feature value was calculated within every window, and then these values were averaged over all windows to provide a single image-wise value for that feature. The use of a lattice for calculating texture features is motivated by previous work which demonstrated that that this approach yields higher area under the curve (AUC) in receiver-operating-characteristic (ROC) experiments in case-control classification than the use of a single region-of-interest (ROI), such as a central or retroareolar ROI.[1]

All radiomic feature calculations were done with a 6.3 mm window size. This value was chosen based on previous work, which analyzed the effect of varying the window size (between 6.3 and 25.5 mm). Zheng *et al*. showed that ROC performance in case-control classification is optimized by the use of a 6.3 mm window size.[1]

2.4 Robustness Analysis

Previous work has shown that radiomic features are dependent on breast thickness under compression.[20] For this reason, we focused specifically on the subset of clinical data with comparable thickness (± 10 mm) to the phantom (50.0 mm thick). For a given feature, the range of values obtained in this subset of the clinical data was *Z*-score normalized, and the same normalization was applied to the phantom.

Table 1. In the phantom acquisitions, there were six settings within the range seen clinically in women with 40-60 mm thickness.

kV	Clinical mAs Range	Phantom mAs Settings
28	[56, 228]	160
29	[63, 277]	140
30	[81, 386]	120
31	[102, 311]	120, 140, 180

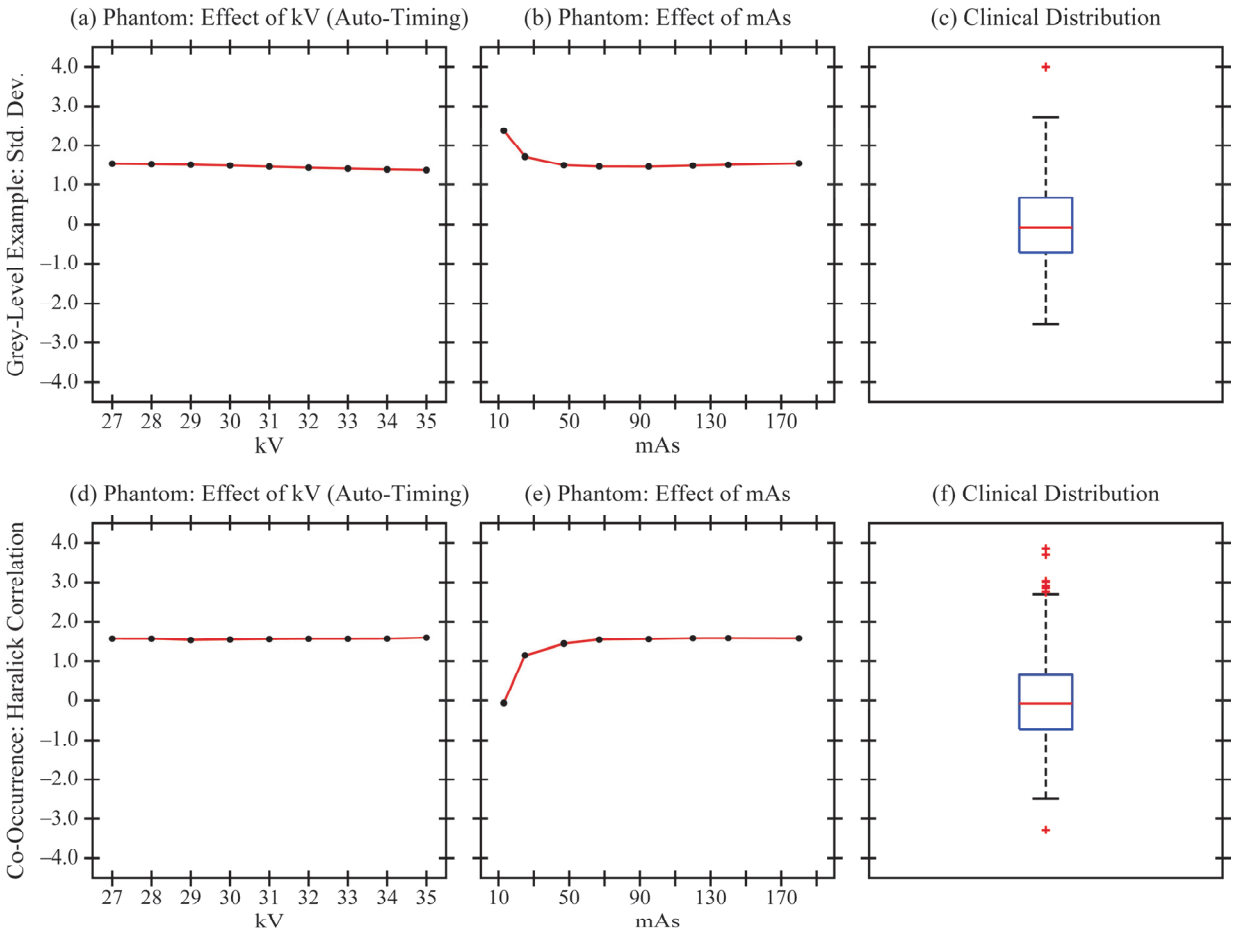

Figure 3. In robust features, the variation across kV and mAs settings is small compared against the range of the clinical distribution.

We initially analyzed how each feature varied as a function of kV and mAs in the phantom acquisitions (Figures 3-4). However, to develop a robustness metric for feature selection, we subsequently restricted the technique settings in the phantom acquisitions to those consistent with women with 40-60 mm thickness (± 10 mm relative to the phantom). This included six combinations of kV and mAs (Table 1). Since each technique setting was repeated twice, there were 12 acquisitions in this analysis. Restricting the technique settings in this manner ensured that measures of robustness did not include extreme settings which would not be representative of those used clinically.

Denoting $P_j = \{p_{ij}\}_{i=1}^{12}$ as the set of feature values in 12 phantom acquisitions for the j^{th} feature, the imaging acquisition variation (IAV) was then defined as

$$\text{IAV} = \frac{\max P_j - \min P_j}{c_{95,j} - c_{5,j}}, \qquad j \in [1,341], \tag{1}$$

where $c_{95,j}$ and $c_{5,j}$ denote the 95th and 5th percentile of the clinical distribution for the j^{th} feature, respectively. In Eq. (1), the range of variation across technique settings is scaled against the spread in the clinical distribution. Since the tails of the clinical distribution could be sensitive to outliers, we measure the spread in terms of the middle 90% of this distribution. In a robust feature, the range of values across technique settings, in a single phantom, should be small compared to the range of values in a population having broadly varying parenchymal patterns.

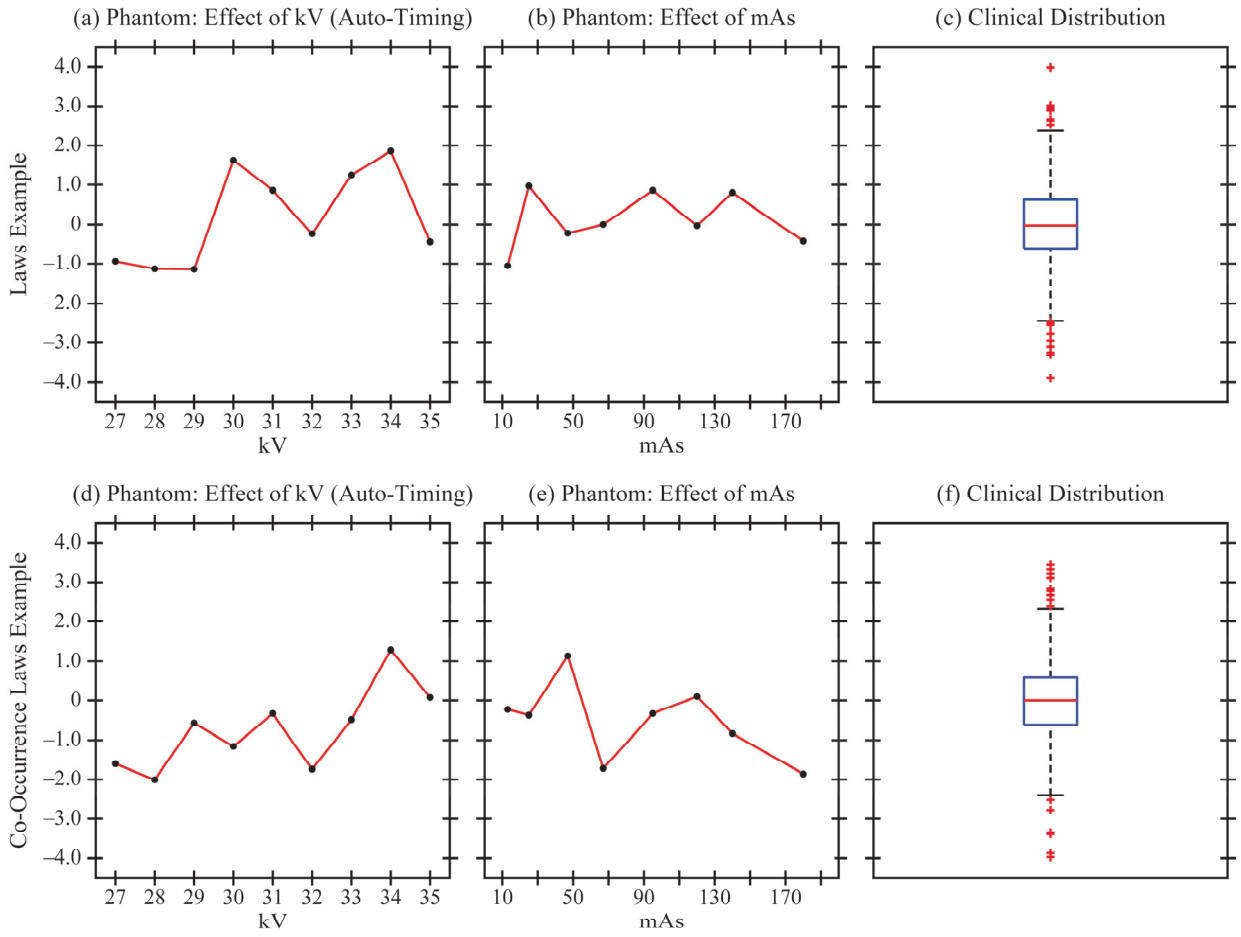

Figure 4. Unlike the robust features shown in Figure 3, the variation across kV and mAs settings is much larger in these Laws and co-occurrence Laws features. Also, the trends versus kV and mAs are not monotonic. For these reasons, the two features shown here are examples of nonrobust features.

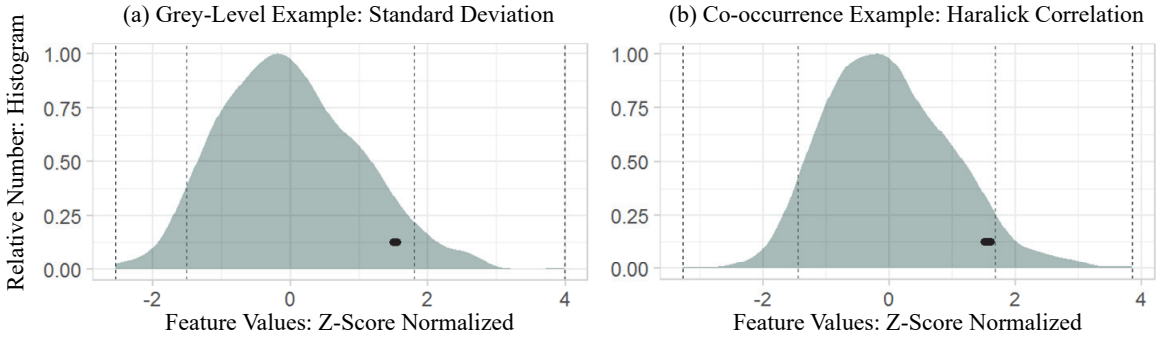

Figure 5. For each feature, the data points obtained from the phantom at different technique settings were compared against the clinical distribution, yielding a measure of imaging acquisition variation (IAV). The data points show little variation relative to the clinical distribution, and hence these are two examples of robust features. The 5th and 95th percentiles of the clinical distribution are denoted by the thin dashed vertical lines.

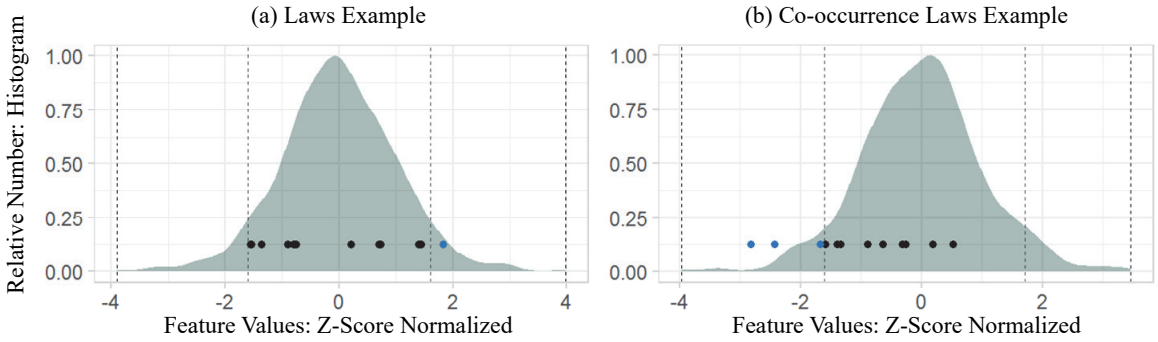

Figure 6. The 12 data points, corresponding to various phantom acquisitions, vary much more broadly than Figure 5. Also, some data points (in blue) extend beyond the 5th or 95th percentile of the clinical distribution (thin dashed vertical lines).

3. RESULTS

3.1 Effect of Varying kV and mAs in Phantom Acquisitions

First, we analyzed the full range of kV and mAs settings in the phantom acquisitions (Figures 3-4). Since the phantom was imaged twice at each setting, we averaged the results at each setting for the purpose of these plots. Two examples of features that are robust to changes in technique settings are shown in Figure 3: a grey-level feature (standard deviation) and a co-occurrence feature (Haralick correlation). The range of variation is small compared against the clinical distribution. By contrast, two examples of features that are sensitive to changes in acquisition settings are shown in Figure 4: Laws and co-occurrence Laws features. In Figure 4, the trends versus kV and mAs are not monotonic.

3.2 Calculation of Robustness Scores for Each Feature

To calculate IAV for each feature, the 12 values derived from phantom acquisitions were analyzed in conjunction with the clinical distribution. In robust features, the 12 data points are clustered within a small range of values compared against the clinical distribution (Figure 5). For the grey-level and co-occurrence features described previously as examples of robust features, the IAV scores are 0.0183 and 0.0309, respectively (approaching zero).

By contrast, some features vary much more broadly with kV and mAs, and thus are much more sensitive to small changes in noise and contrast. These features have higher IAV scores, specifically 1.05 and 1.01 for the Laws and co-occurrence Laws features described previously as examples of nonrobust features (Figure 6).

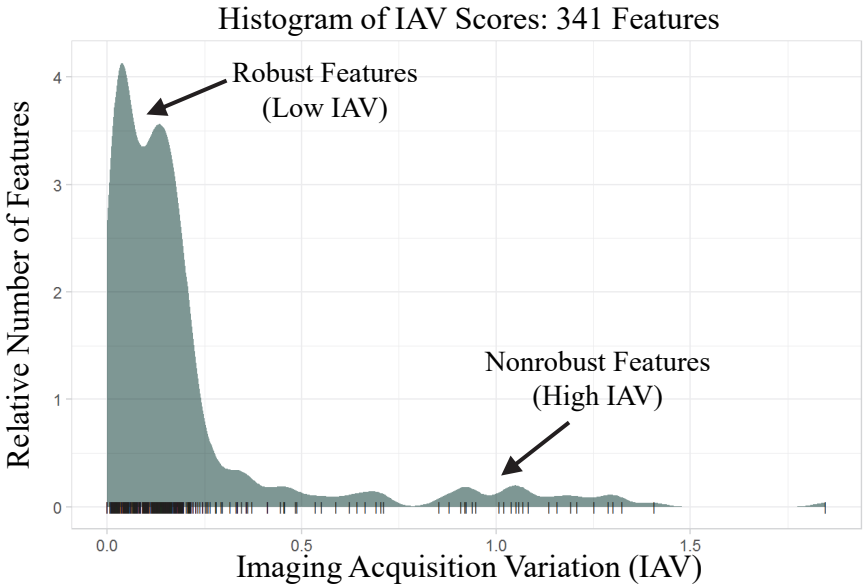

Figure 7. Imaging acquisition variation (IAV) scores determined by Eq. (1) can be used to identify robust features.

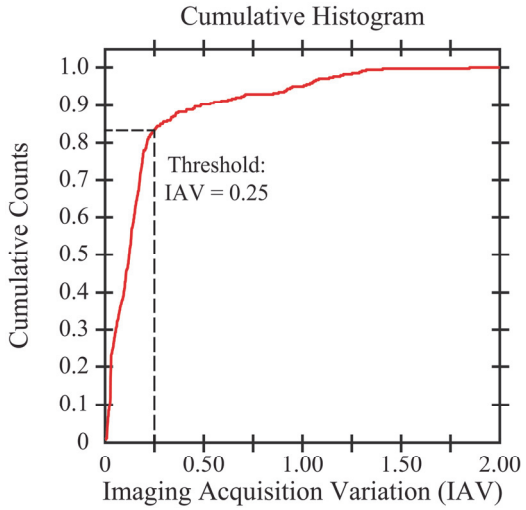

Figure 8. In the cumulative histogram of IAV scores, the curve rises sharply up to an IAV of 0.25. At this threshold, 284 features out of 341 (83%) are considered robust (IAV ≤ 0.25).

Results for all 341 features can be summarized in terms of the histogram of IAV scores (Figure 7). Most IAV scores are clustered around zero, corresponding to robust features. There is an extended tail corresponding to features with high IAV scores. The maximum IAV score is 1.85.

A threshold for identifying robust features can be introduced based on the cumulative histogram of IAV scores (Figure 8). The cumulative histogram peaks sharply up to an IAV of 0.25. Above this value, the curvature starts to change. This curvature suggests that an IAV score of 0.25 can be used as a threshold for identifying robust features. Out of 341 features, 284 features (83%) meet the threshold IAV ≤ 0.25.

3.3 Analysis of Eight Feature Families

Next, the IAV scores were analyzed separately in each of the eight feature families (Figure 9). In five families out of eight, all features met the threshold IAV ≤ 0.25; namely, grey-level histogram, co-occurrence, run length, Gabor Wavelet, and fractal dimension. The three remaining feature families included a combination of robust and nonrobust features. Specifically, 81% of LBP features (29 out of 36), 73% of Laws features (91 out of 125), and 87% of co-occurrence Laws features (104 out of 120) can be considered robust.

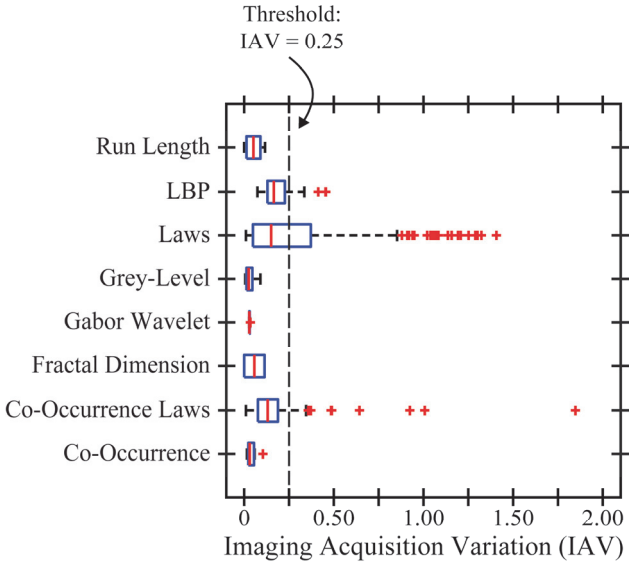

Figure 9. The features that fail to meet the threshold for robustness (IAV ≤ 0.25) come from three families: LBP, Laws, and co-occurrence Laws.

4. DISCUSSION AND CONCLUSION

Although it is not possible to acquire x-ray images of a patient with numerous technique settings, it is indeed possible to perform these experiments with an anthropomorphic phantom. The phantom used in this study was based off an actual woman's mammogram[13], and hence these x-ray experiments were equivalent to imaging the same woman under various technique settings. Since the underlying texture of the phantom was fixed, robust features were identified under the assumption that variation across technique settings should be small.

In a previous study, Mendel *et al*. identified robust features based on a data set of women imaged separately with two DM vendors.[12] They showed, for example, that measures of fractal dimension are robust. The results of this study are consistent with that finding (Figure 9). Our approach for identifying robust features is unique in that we analyze phantom and clinical data in combination; this allows the effect of imaging acquisition physics to be measured relative to the spread of values in a clinical population.

In our future work, we will investigate whether features selected based on a robustness criterion offer better ROC performance in case-control classification with an independent data set. Another point of future investigation is to study the effect of image processing on the robustness of the features. For the purpose of this study, only raw ("FOR PROCESSING") DM images were analyzed.

5. ACKNOWLEDGEMENT

Support was provided by the following grants: R01CA207084 and U54CA163313 from the National Institute of Health, W81XWH-18-1-0082 from the Department of Defense Breast Cancer Research Program, and PDF17479714 from Susan G. Komen®. The content is solely the responsibility of the authors and does not necessarily represent the official views of the funding agencies.

ADAM receives research support from Hologic Inc., Barco NV, and Analogic Corporation. Also, ADAM is a shareholder and member of the scientific advisory board of Real Time Tomography, LLC. EFC receives grant support and is part of the advisory panel of Hologic Inc. EFC also receives grant support and is part of the advisory panel of iCAD Inc.

6. REFERENCES

1. Zheng Y, Keller BM, Ray S, et al. Parenchymal texture analysis in digital mammography: A fully automated pipeline for breast cancer risk assessment. *Medical Physics.* 2015;42(7):4149-4160.
2. Balagurunathan Y, Kumar V, Gu Y, et al. Test–Retest Reproducibility Analysis of Lung CT Image Features. *Journal of Digital Imaging.* 2014;27:805-823.
3. Zhang Y, Oikonomou A, Wong A, Haider MA, Khalvati F. Radiomics-based Prognosis Analysis for Non-Small Cell Lung Cancer. *Scientific Reports.* 2017;7:46349.
4. Parmar C, Grossmann P, Bussink J, Lambin P, Aerts HJWL. Machine Learning methods for Quantitative Radiomic Biomarkers. *Scientific Reports.* 2015;5:13087.
5. Rizzo S, Botta F, Raimondi S, et al. Radiomics of high-grade serous ovarian cancer: association between quantitative CT features, residual tumour and disease progression within 12 months. *European Radiology.* 2018;28(11):4849-4859.
6. Huynh E, Coroller TP, Narayan V, et al. Associations of Radiomic Data Extracted from Static and Respiratory-Gated CT Scans with Disease Recurrence in Lung Cancer Patients Treated with SBRT. *PLoS One.* 2017;12(1):e0169172.
7. Wilkinson L, Friendly M. The History of the Cluster Heat Map. *The American Statistician.* 2009;63(2):179-184.
8. Rizzo S, Botta F, Raimondi S, et al. Radiomics: the facts and the challenges of image analysis. *European Radiology Experimental.* 2018;2:36.
9. Yousefi B, Jahani N, LaRiviere MJ, et al. Correlative Hierarchical Clustering-based Low-Rank dimensionality reduction of radiomics-driven phenotype in Non-Small Cell Lung Cancer. Paper presented at: SPIE Medical Imaging2019; San Diego, CA.

10. Robinson K, Li H, Lan L, Schacht D, Giger M. Radiomics robustness assessment and classification evaluation: A two-stage method demonstrated on multivendor FFDM. *Medical Physics.* 2019;46(5):2145-2156.

11. Keller BM, Oustimov A, Wang Y, et al. Parenchymal texture analysis in digital mammography: robust texture feature identification and equivalence across devices. *Journal of Medical Imaging.* 2015;2(2):024501-024501 - 024501-024513.

12. Mendel KR, Li H, Lan L, et al. Quantitative texture analysis: robustness of radiomics across two digital mammography manufacturers' systems. *Journal of Medical Imaging.* 2018;5(1):011002-011001 - 011002-011009.

13. Yaffe MJ, Johns PC, Nishikawa RM, Mawdsley GE, Caldwell CB. Anthropomorphic radiologic phantoms. *Radiology.* 1986;158(2):550-552.

14. Keller BM, Nathan DL, Wang Y, et al. Estimation of breast percent density in raw and processed full field digital mammography images via adaptive fuzzy c-means clustering and support vector machine segmentation. *Medical Physics.* 2012;39(8):4903-4917.

15. Haralick RM, Shanmugam K, Dinstein IH. Textural Features for Image Classification. *IEEE Transactions on Systems, Man, and Cybernetics.* 1973;SMC-3(6):610-621.

16. Galloway MM. Texture analysis using gray level run lengths. *Computer Graphics and Image Processing.* 1975;4(2):172-179.

17. Chu A, Sehgal CM, Greenleaf JF. Use of gray value distribution of run lengths for texture analysis. *Pattern Recognition Letters.* 1990;11(6):415-419.

18. Ojala T, Pietikäinen M, Mäenpää T. Multiresolution Gray-Scale and Rotation Invariant Texture Classification with Local Binary Patterns. *IEEE Transactions on Pattern Analysis and Machine Intelligence.* 2002;24(7):971-987.

19. Manduca A, Carston MJ, Heine JJ, et al. Texture Features from Mammographic Images and Risk of Breast Cancer. *Cancer Epidemiology, Biomarkers & Prevention.* 2009;18(3):837-845.

20. Acciavatti RJ, Hsieh M-K, Gastounioti A, et al. Validation of the Textural Realism of a 3D Anthropomorphic Phantom for Digital Breast Tomosynthesis. Paper presented at: 14th International Workshop on Breast Imaging (IWBI 2018)2018; Atlanta, GA.

Determining the Optimal Angular Range of the X-Ray Source Motion in Tomosynthesis Using Virtual Clinical Trials

Bruno Barufaldi*, Trevor L. Vent, Raymond J. Acciavatti, Predrag R. Bakic, Peter B. Noël, Emily F. Conant, and Andrew D. A. Maidment

Department of Radiology, University of Pennsylvania, Philadelphia, United States.
*Bruno.Barufaldi@uphs.upenn.edu

ABSTRACT

The limited angle and limited number of projections in digital breast tomosynthesis (DBT) produce under-sampled datasets that may compromise calcification detection. Small breast lesions, such as microcalcifications, may not be discernible without sufficient sampling in the reconstructed DBT images. We propose a virtual clinical trial (VCT) method to evaluate the calcification detection in DBT using computer simulations of breast phantoms, images, and virtual readers. We used multiple-reader multiple-case (MRMC) receiver operating characteristic (ROC) analyses to evaluate the performance of channelized Hotelling observers (CHOs) in calcification detection. The angular motion path of the x-ray source was varied to simulate different DBT acquisition geometries. We simulated continuous and step-and-shoot x-ray source motion and three angular motion paths: ±7.5°, ±15°, and ±25°. The detection of calcifications is affected by the angular motion path, particularly for the ±25° angular range, combined with continuous tube motion, larger detector element sizes (0.14 mm) and larger reconstructed voxel sizes (0.10 mm). When an angular range of ±25° is compared to ±7.5°, the difference in the area under the curve (AUC) is -0.030 (*d'* ratio=0.633) and -0.067 (*d'* ratio=0.584), for one- and two- voxel calcifications (0.1 mm³ and 0.2 mm³), respectively. There is no significant difference in calcification detection using images acquired with ±7.5° and ±15°. The results provide insight on the impact of angular range for calcification detection, an ongoing limitation of tomosynthesis.

Keywords: virtual clinical trial; multiple-reader, multiple-case; digital breast tomosynthesis.

1. INTRODUCTION

Digital breast tomosynthesis (DBT) is a limited-angle tomographic technique that provides high-resolution 3D image reconstructions of the breast. DBT has shown substantial improvements in the detectability and characterization of subtle, soft-tissue lesions.[1–3] Conversely however, previous studies have shown that DBT is not superior to full-field digital mammography (FFDM) for calcification detection.[4–6]

The detectability of calcifications is dependent on the DBT acquisition parameters (e.g., scan angle, x-ray source motion, number of projections, detector element size, and reconstructed pixel size).[7–9] The optimal combination of the acquisition parameters in DBT is still the subject of further investigation.[7]

Virtual clinical trials (VCT) can be used for the evaluation and optimization of imaging systems by performing simulations of the human anatomy, image acquisition, and image interpretation.[10–12] We have conducted VCTs to investigate the limit of breast lesion detection and to evaluate promising imaging designs, avoiding the pursuit of inefficient DBT acquisition parameters.[8,13] Bakic *et al.* have shown that VCT simulations exhibit a mean area under the curve (AUC) improvement of 0.10 for masses and only 0.03 for calcifications when comparing the performance of DBT with FFDM for breast lesion detection.[14] We also showed that the limit of calcification detection is affected by reconstructed voxel size, x-ray source motion, and detector element size, especially for small calcifications.[8]

In this work, we present a simulation method for determining the most suitable angular range of x-ray source motion for calcification detection in DBT. Voxelized calcifications of 100, 200, and 300 µm³ were inserted into software breast phantoms. Fifteen DBT projections (i.e., equal filtration, kV, and mAs) of the breast phantoms with and without lesions were synthesized assuming a clinical acquisition geometry. We simulated the angular range of the x-ray source in DBT using projections of the breast phantoms over a ±7.5°, ±15°, and ±25° angles. We also simulated the detector element size (0.140 mm and 0.085 mm) and reconstructed voxel size (0.100 mm and 0.085 mm). Virtual readers were used to evaluate the calcification detection using one-shot multiple-reader, multiple-case (MRMC) receiver operator curve (ROC) analyses.

Medical Imaging 2020: Physics of Medical Imaging, edited by Guang-Hong Chen, Hilde Bosmans, Proc. of SPIE
Vol. 11312, 113120I · © 2020 SPIE · CCC code: 1605-7422/20/$21 · doi: 10.1117/12.2549600

2. MATERIALS & METHODS

2.1. Virtual Patient Accrual

An open-source VCT framework (OpenVCT) was developed to simulate the accrual of virtual patients.[10] Anthropomorphic breast phantoms were simulated using a recursive partitioning algorithm optimized to reduce computational complexity.[15,16] The recursive partitioning algorithm was implemented using GPU programming to support a large number of breast simulations in reasonable time. In total, 80 uncompressed breast phantoms (volume=700 mL and thickness=126.6 mm) were simulated by combining coarse- and fine-breast tissue models into phantoms,[16] with volumetric breast densities that varied from 10% to 50%.

Medio-lateral (ML) breast compression was simulated using customized finite element (FE) meshes.[17] We simulated the mechanical properties of breast tissue compression using neo-Hookean models, with Poisson ratio of 0.49, and Young's modulus of 12.750 kPa. These compression parameters reduce the phantom thickness by 50% (thickness=63.3 mm).[11]

Single calcifications were simulated as polycubes containing one to three cubes with a voxel size of 100 μm^3.[16] The contrast of the simulated calcifications was controlled by varying the voxel composition, defined by a weighting factor (WF). The WF represents the fraction of hydroxyapatite (i.e., material composition) of the calcifications. In total, 42 calcifications were embedded into each compressed breast phantom. The method for inserting lesions was published previously.[8] The calcifications were positioned 20 mm apart in the plane parallel to detector at the level of the nipple.

2.2. Acquisition Geometry Simulation

DBT projections of phantoms with and without lesions were synthesized assuming different DBT acquisition geometries (Table 1). The DBT projections are simulated using the Siddon algorithm for x-ray tracing.[18] This algorithm describes a 3D dataset, arranged as three sets of orthogonal planes that facilitate the tracing of a ray from the source, through a volume, onto each detector element. The radiological path length is determined by the sum of the length traveled by this ray in each voxel, multiplied by the relative electron density of the voxel. This process is repeated for each ray trajectory, and the intensity of the rays in a detector element determine the pixel value for the projection image.

The x-ray acquisitions were simulated using continuous tube motion, and the angular range of the x-ray source was simulated using ±7.5°, ±15°, and ±25° (Figure 1). Reconstructed DBT slices were produced using a commercially available software library.[19,20]

Table 1. Summary of DBT acquisition geometries simulated.

DBT System	(A)	(B)
X-Ray Imaging		
Anode Material (a.u)	Tungsten	
Filter Material (a.u)	Aluminum	
Filter Thickness (mm)	0.7	
Angular Range (°)	[±7.5, ±15, ±25]	
Number of Projections (#)	15	
Tube Motion (a.u)	Continuous	Step-and-Shoot
Detector		
Detection Material (a.u.)	a-Se	
Detector Element Size (mm)	0.140 × 0.140	0.085 × 0.085
Number of Elements (#)	2048 × 1664	3584 × 2816
Detector Size (mm)	286.72 × 232.96	304.64 × 239.36
Source-to-Image Distance (mm)	700.0	652.0
Reconstruction		
Voxel Size (mm)	0.100	0.085

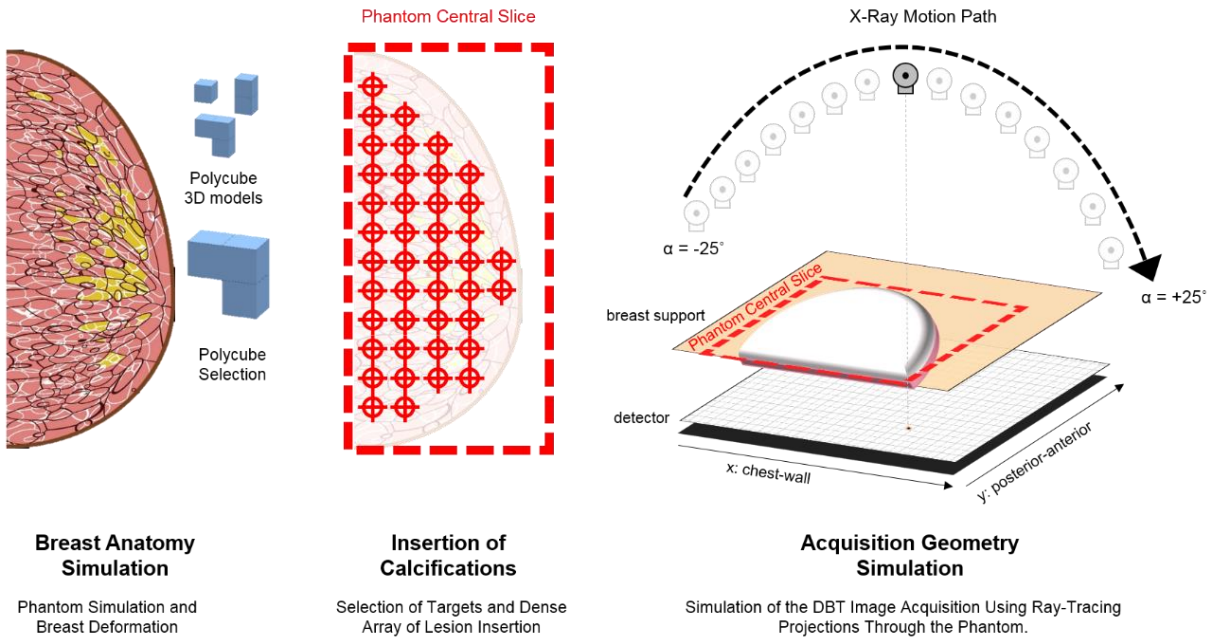

Figure 1. Method used for inserting dense grid of calcifications in the breast phantoms and for simulating the DBT acquisition geometry using angular motion path of the x-ray source.

2.3. Virtual Reader Simulation

We used channelized Hotelling observers (CHOs) to simulate virtual readers.[21,22] The CHOs were designed using 15 Laguerre-Gauss channels and, spread of 22 and 26, for images simulated using the DBT acquisition geometries (A) and (B), respectively. For each image reconstructed at the central phantom slice, we cropped ROIs centered about each calcification. The ROIs were cropped using 150×150 and 175×175 pixels for images simulated using the DBT acquisition geometries (A) and (B), respectively. For each CHO, training and testing image sets for each acquisition geometry included 252 ROIs with simulated calcifications and 252 calcification-free ROIs.

The ROIs were divided into "calcification-free" and "calcification" cohorts. The ROIs were also divided into independent training and testing ROI sets. Each reader was trained with an independent training set, but tested with a common ROI set. The ROIs used for training and testing were selected randomly for each reader.

2.4. Statistical Analyses

We measured the performance of calcification detection using ROC analyses provided by the MeVIC software (Barco NV, Kortrijk, Belgium).[23] The MeVIC software includes a module that estimates one-shot MRMC statistics.[24,25] We calculated the area under the curve (AUC) and *d'* statistics for every DBT acquisition geometry.

The non-parametric Kruskal-Wallis (K-W) test by rank and Mann-Whitney-Wilcoxon (MWW) test were used to estimate differences in mean AUCs of five readers. We analyzed significant differences in the pairwise comparison of continuous variables for every DBT acquisition geometries. The scores of each reader was pooled to calculate empirical ROC curves that represent a cumulative ROC analysis of five readers.

3. RESULTS & DISCUSSION

The AUCs of the pooled ROC improve with greater number of calcification voxels and reduce with lower fraction of hydroxyapatite (Table 2). The acquisition geometry and tube motion also affect the AUCs. For acquisition geometry A (continuous tube motion), images acquired with ±7.5° and ±25° show a significant difference in the detection of one- and two-voxel calcifications (P<0.001 and P<0.05). There is no significant difference in the detection of these calcifications (P=0.86 and P=0.22) using images acquired with ±7.5° and ±25° for DBT acquisition geometry B (step-and-shoot) suggesting that tube motion is an important contributor to calcification detection. Similarly, there is no significant

difference in three-voxel calcifications for any condition, nor for any calcification size using images acquired with ±7.5° and ±15° for both DBT acquisition geometries A and B.

AUC varies from 0.5 (i.e., random guessing) to 1.0 (i.e., relationship between disease and normal found with 100% certainty). Using the AUC values, we calculated *d'* that represents the effective signal-to-noise ratio perceived by the observer. Note that *d'* also improves with greater number of calcification voxels and reduces with lower fraction of hydroxyapatite (Table 3).

Table 2. Summary of AUC stratified by number of voxels, x-ray source angle and weight factor (WF).

(A)									
	1-Voxel Polycube			**2-Voxel Polycube**			**3-Voxel Polycube**		
	X-ray Source Angle			**X-ray Source Angle**			**X-ray Source Angle**		
WF	**7.5**	**15**	**25**	**7.5**	**15**	**25**	**7.5**	**15**	**25**
1.0	0.832	0.808	0.800	-	-	-	-	-	-
0.9	0.800	0.778	0.739	0.950	0.945	0.887	0.981	0.984	0.963
0.8	0.736	0.700	0.696	0.910	0.912	0.832	0.973	0.970	0.933
0.7	0.688	0.696	0.629	0.852	0.855	0.754	0.934	0.930	0.908
0.6	0.626	0.604	0.586	0.730	0.751	0.692	0.863	0.836	0.841
0.5	0.568	0.567	0.553	0.673	0.655	0.620	0.742	0.761	0.754
0.4	-	-	-	0.565	0.545	0.535	0.669	0.637	0.618
0.3	-	-	-	-	-	-	0.519	0.546	0.536
(B)									
1.0	0.932	0.948	0.938	-	-	-	-	-	-
0.9	0.917	0.912	0.906	0.984	0.978	0.973	0.997	0.998	0.998
0.8	0.901	0.894	0.877	0.978	0.962	0.966	0.998	0.996	0.996
0.7	0.857	0.873	0.857	0.961	0.955	0.950	0.999	0.994	0.989
0.6	0.827	0.843	0.819	0.942	0.943	0.921	0.992	0.982	0.986
0.5	0.774	0.793	0.789	0.908	0.898	0.866	0.983	0.975	0.960
0.4	0.727	0.718	0.703	0.862	0.846	0.837	0.962	0.945	0.945
0.3	0.640	0.661	0.646	0.794	0.780	0.768	0.890	0.873	0.895
0.2	0.570	0.586	0.593	0.699	0.680	0.669	0.750	0.775	0.789
0.1	-	-	-	0.538	0.539	0.516	0.579	0.594	0.611

Table 3. Summary of *d'* stratified by number of voxels, x-ray source angle and weight factor (WF).

(A)									
	1-Voxel Polycube			**2-Voxel Polycube**			**3-Voxel Polycube**		
	X-ray Source Angle			**X-ray Source Angle**			**X-ray Source Angle**		
WF	**7.5**	**15**	**25**	**7.5**	**15**	**25**	**7.5**	**15**	**25**
1.0	1.36	1.23	1.19	-	-	-	-	-	-
0.9	1.19	1.08	0.90	2.32	2.25	1.71	2.95	3.03	2.54
0.8	0.89	0.74	0.73	1.90	1.91	1.36	2.73	2.65	2.12
0.7	0.69	0.73	0.47	1.48	1.50	0.97	2.13	2.09	1.88
0.6	0.45	0.37	0.31	0.87	0.96	0.71	1.55	1.38	1.41
0.5	0.24	0.24	0.19	0.63	0.57	0.43	0.92	1.00	0.97
0.4	-	-	-	0.23	0.16	0.12	0.62	0.50	0.43
0.3	-	-	-	-	-	-	0.07	0.16	0.13
(B)									
1.0	2.11	2.30	2.17	-	-	-	-	-	-
0.9	1.96	1.91	1.86	3.03	2.84	2.73	3.94	4.08	4.10
0.8	1.82	1.76	1.64	2.85	2.51	2.58	4.17	3.75	3.71
0.7	1.51	1.61	1.51	2.48	2.39	2.33	4.27	3.58	3.24
0.6	1.33	1.43	1.29	2.23	2.24	2.00	3.38	2.98	3.10
0.5	1.06	1.15	1.13	1.88	1.80	1.57	2.98	2.78	2.48
0.4	0.85	0.81	0.75	1.54	1.44	1.39	2.51	2.26	2.26
0.3	0.51	0.59	0.53	1.16	1.09	1.03	1.73	1.62	1.77
0.2	0.25	0.31	0.33	0.74	0.66	0.62	0.95	1.07	1.14
0.1	-	-	-	0.13	0.14	0.06	0.28	0.34	0.40

Overall, for DBT acquisition geometry A there is a significant difference in calcification detection for images acquired with ±7.5° and ±25° (P<0.048), but no difference in calcification detection for images acquired with ±7.5° and 15° (P=0.70). There is no significant difference in calcification detection for images acquired using DBT acquisition geometry B with ±7.5° and ±15° (P=0.77), and ±7.5° and ±25° (P=0.43). The pooled AUC of 5 readers and *d'* of stratified calcification size and angular motion path of the x-ray source is shown in Figure 2 and Figure 3, respectively.

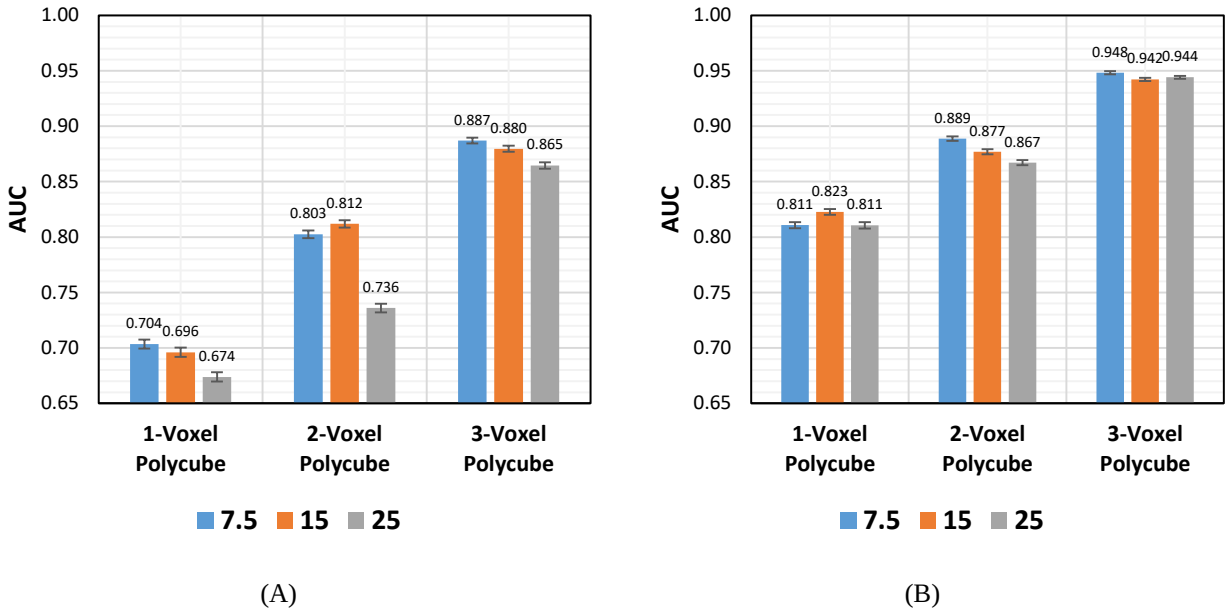

(A) (B)

Figure 2. AUC analyses of five readers for calcification detection (from 1- to 3-voxel polycube), stratified by angular range of the x-ray source.

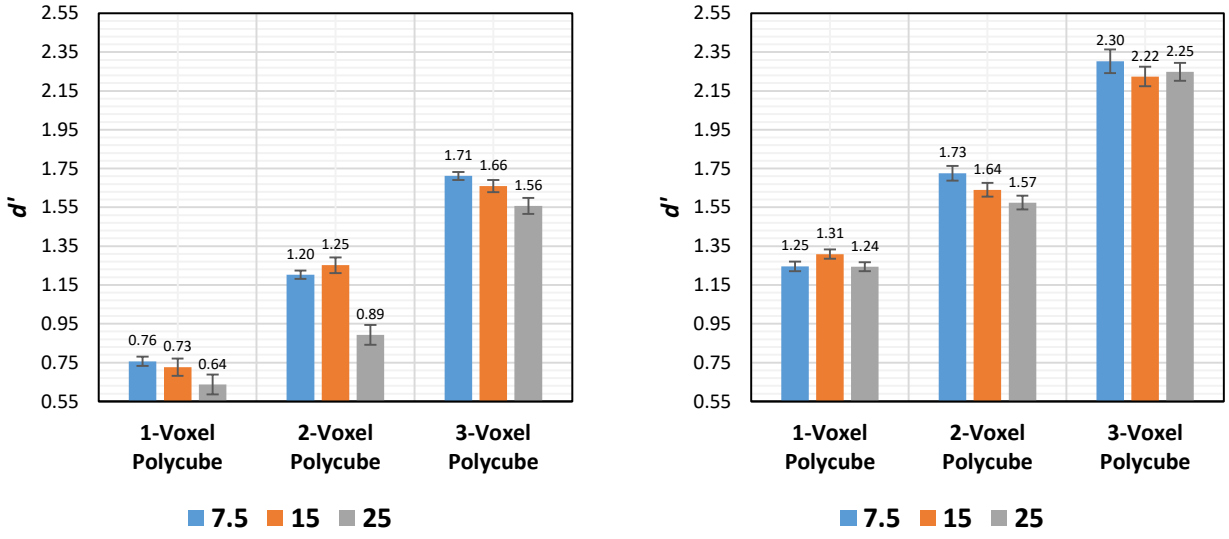

(A) (B)

Figure 3. *d'* analyses of five readers for calcification detection (from 1- to 3-voxel polycube), stratified by angular range of the x-ray source.

The detection of calcifications is affected by angular motion path of the x-ray source, in particular for wide angle. Our results indicate that ±25° source motion reduces substantially the calcification detection when the DBT acquisition geometry is combined with larger detector element sizes (0.140 mm) and continuous x-ray source motion. The impact in calcification detection is greater for two-voxel calcifications (0.200 mm^3). The detection of calcifications is not significantly affected by angular motion path when the DBT acquisition geometry is combined with step-and-shoot source motion and smaller detector element sizes (0.085 mm).

4. CONCLUSION

We simulated the detectability of calcifications in DBT using two DBT imaging geometries (A and B) and three angular ranges of the x-ray source motion: ±7.5°, ±15°, and ±25°. The impact on calcification detection is more prominent for small calcifications and/or lower fraction of hydroxyapatite in composition. The performance in calcification detection is degraded when the DBT acquisition geometry is combined with wide-angle path (±25°), continuous source motion, and larger detector element size (0.14 mm).

These results are preliminary; however, we believe they provide guidance on how to improve the detectability of calcifications, which is an ongoing problem in tomosynthesis. We are also investigating the experimental validation of this study using a DBT prototype fabricated in our laboratory[26], which is capable of customizable acquisition geometries for DBT.

ACKNOWLEDGEMENTS

Funding for the research is supported by the following grants: NIH R01 CA154444, NIH R01 EB018958, Komen IIR-13262248, BWF IRSA 1016451, and DoD W81XWH-18-1-0082.

REFERENCES

[1] Kopans, D. B., "Basic Physics and Doubts about Relationship between Mammographically Determined Tissue Density and Breast Cancer Risk," Radiology **246**(2), 1–6 (2008).

[2] Conant, E. F., "Clinical Implementation of Digital Breast Tomosynthesis," Radiol. Clin. North Am. **52**(3), 499–518 (2014).

[3] Vedantham, S., Karellas, A., Vijayaraghavan, G. R. and Kopans, D. B., "Digital Breast Tomosynthesis: State of the Art," Radiology **277**(3), 663–684 (2015).

[4] Rafferty, E. A., Park, J. M., Philpotts, L. E., Poplack, S. P. and Sumkin, J. H., "Digital Mammography and Breast Tomosynthesis Compared with Digital Mammography Alone: Results of a Multicenter, multireader trial," Radiology **266**(1), 104–113 (2013).

[5] Rafferty, E. A., Park, J. M., Philpotts, L. E., Poplack, S. P., Sumkin, J. H., Halpern, E. F. and Niklason, L. T., "Diagnostic accuracy and recall rates for digital mammography and digital mammography combined with one-view and two-view tomosynthesis: Results of an enriched reader study," Am. J. Roentgenol. **202**(2), 273–281 (2014).

[6] Zuckerman, S. P., Conant, E. F., Keller, B. M., Maidment, A. D. A., Barufaldi, B., Weinstein, S. P., Synnestvedt, M. and Mcdonald, E., "Implementation of Synthesized Two-dimensional Mammography in a Population-based Digital Breast Tomosynthesis Screening," Radiol. J. **000**(0), 1–7 (2016).

[7] Elangovan, P., Mackenzie, A., Dance, D. R., Young, K. C., Cooke, V., Wilkinson, L., Given-Wilson, R. M., Wallis, M. G. and Wells, K., "Design and validation of realistic breast models for use in multiple alternative forced choice virtual clinical trials," Phys. Med. Biol. (2017).

[8] Barufaldi, B., Bakic, P. R. and Maidment, A. D. A., "Multiple-reader, multiple-case ROC analysis for determining the limit of calcification detection in tomosynthesis," SPIE Med. Imaging 2019 Phys. od Med. Imaging **10948**(March), 22 (2019).

[9] Chan, H.-P., Goodsitt, M. M., Helvie, M. A., Zelakiewicz, S., Schmitz, A., Noroozian, M., Paramagul, C., Roubidoux, M. A., Nees, A. V., Neal, C. H., Carson, P., Lu, Y., Hadjiiski, L. and Wei, J., "Digital Breast Tomosynthesis: Observer Performance of Clustered Microcalcification Detection on Breast Phantom Images Acquired with an Experimental System Using Variable Scan Angles, Angular Increments, and Number of Projection Views," Radiology **273**(3), 675–685 (2014).

[10] Barufaldi, B., Bakic, P. R., Higginbotham, D. and Maidment, A. D. A., "OpenVCT: a GPU-accelerated virtual clinical trial pipeline for mammography and digital breast tomosynthesis," SPIE Med. Imaging 2018 **1057358**(March), 1–8, Houston, TX (2018).

[11] Barufaldi, B., Bakic, P. R., Pokrajac, D. D., Lago, M. A. and Maidment, A. D. A., "Developing populations of software breast phantoms for virtual clinical trials," 14th Int. Work. Breast Imaging (IWBI 2018)(July), 73 (2018).
[12] Badano, A., Graff, C. G., Badal, A., Sharma, D., Zeng, R., Samuelson, F. W., Glick, S. J. and Myers, K. J., "Evaluation of Digital Breast Tomosynthesis as Replacement of Full-Field Digital Mammography Using an In Silico Imaging Trial," JAMA Netw. Open **1**(7), 1–12 (2018).
[13] Vent, T. L., Barufaldi, B. and Maidment, A. D. A., "Simulation and experimental validation of high-resolution test objects for evaluating a next-generation digital breast tomosynthesis prototype," SPIE Med. Imaging 2019(March), 21 (2019).
[14] Bakic, P. R., Barufaldi, B., Higginbotham, D., Weinstein, S. P., Avanaki, A., Espig, K., Xthona, A., Kimpe, T. and Maidment, A. D. A., "Virtual clinical trial of lesion detection in digital mammography and digital breast tomosynthesis," SPIE Med. Imaging 2018 **1057306**(March), 1–13 (2018).
[15] Pokrajac, D. D., Maidment, A. D. A. and Bakic, P. R., "Optimized generation of high resolution breast anthropomorphic software phantoms," Med. Phys. **39**(4), 2290 (2012).
[16] Bakic, P. R., Barufaldi, B., Pokrajac, D., Weinstein, S. P. and Maidment, A. D., "Optimized simulation of breast anatomy for virtual clinical trials," 14th Int. Work. Breast Imaging (IWBI 2018)(July), 73 (2018).
[17] Lago, M. A., Maidment, A. D. A. and Bakic, P. R., "Modelling of mammographic compression of anthropomorphic software breast phantom using FEBio," Int'l Symp. Comput. Methods Biomech. Biomed. Eng., Salt Lake City, UT (2013).
[18] Siddon, R. L., "Fast calculation of the exact radiological path for a three dimensional CT array," Med. Phys. **12**(2), 252–255 (1985).
[19] Kuo, J., Ringer, P. A., Fallows, S. G., Bakic, P. R., Maidment, A. D. A. and Ng, S., "Dynamic reconstruction and rendering of 3D tomosynthesis images," SPIE Med. Imaging **796116**(March 2011), 796116-796116–11, Orlando, FL (2011).
[20] Chui, J. H., Pokrajac, D. D., Maidment, A. A. D. A. and Bakic, P. R., "Roadmap for efficient parallelization of breast anatomy simulation," SPIE Med. Imaging **8313**, 83134T (2012).
[21] Abbey, C. K. and Barrett, H. H., "Human- and model-observer performance in ramp-spectrum noise: effects of regularization and object variability," J. Opt. Soc. Am. A (2001).
[22] Park, S., Zhang, G. and Myers, K. J., "Comparison of Channel Methods and Observer Models for the Task-Based Assessment of Multi-Projection Imaging in the Presence of Structured Anatomical Noise," IEEE Trans. Med. Imaging **35**(6), 1431–1442 (2016).
[23] Marchessoux, C., Kimpe, T. and Bert, T., "A virtual image chain for perceived and clinical image quality of medical display," IEEE/OSA J. Disp. Technol. **4**(4), 356–368 (2008).
[24] Gallas, B. D. and Barrett, H. H., "Validating the use of channels to estimate the ideal linear observer.," J. Opt. Soc. Am. A. Opt. Image Sci. Vis. **20**(9), 1725–1738 (2003).
[25] Gallas, B. D., "One-shot estimate of MRMC variance: AUC," Acad. Radiol. **13**(3), 353–362 (2006).
[26] Acciavatti, R. J., Barufaldi, B., Vent, T. L., Wileyto, E. P. and Maidment, A. D. A., "Personalization of x-ray tube motion in digital breast tomosynthesis using virtual Defrise phantoms," Med. Imaging 2019 Phys. Med. Imaging(March), 10 (2019).

Calculation of Radiomic Features to Validate the Textural Realism of Physical Anthropomorphic Phantoms for Digital Mammography

Raymond J. Acciavatti[1], Eric A. Cohen[1], Omid Haji Maghsoudi[1], Aimilia Gastounioti[1], Lauren Pantalone[1], Meng-Kang Hsieh[1], Bruno Barufaldi[1], Predrag R. Bakic[1], Jinbo Chen[2], Emily F. Conant[1], Despina Kontos[1], Andrew D. A. Maidment[1]
[1]University of Pennsylvania, Department of Radiology, 3400 Spruce Street, Philadelphia PA 19104
[2]University of Pennsylvania, Department of Epidemiology, Biostatistics, & Informatics, 423 Guardian Drive, Philadelphia, PA 19104
E-mail: {Raymond.Acciavatti | Andrew.Maidment}@pennmedicine.upenn.edu

ABSTRACT

In this paper, radiomic features are used to validate the textural realism of two anthropomorphic phantoms for digital mammography. One phantom was based off a computational breast model; it was 3D printed by CIRS (Computerized Imaging Reference Systems, Inc., Norfolk, VA) under license from the University of Pennsylvania. We investigate how the textural realism of this phantom compares against a phantom derived from an actual patient's mammogram ("Rachel", Gammex 169, Madison, WI). Images of each phantom were acquired at three kV in 1 kV increments using auto-time technique settings. Acquisitions at each technique setting were repeated twice, resulting in six images per phantom. In the raw ("FOR PROCESSING") images, 341 features were calculated; *i.e.*, gray-level histogram, co-occurrence, run length, fractal dimension, Gabor Wavelet, local binary pattern, Laws, and co-occurrence Laws features. Features were also calculated in a negative screening population. For each feature, the middle 95% of the clinical distribution was used to evaluate the textural realism of each phantom. A feature was considered realistic if all six measurements in the phantom were within the middle 95% of the clinical distribution. Otherwise, a feature was considered unrealistic. More features were actually found to be realistic by this definition in the CIRS phantom (305 out of 341 features or 89.44%) than in the phantom derived from a specific patient's mammogram (261 out of 341 features or 76.54%). We conclude that the texture is realistic overall in both phantoms.

Keywords: Radiomics, digital mammography, anthropomorphic phantom, x-ray imaging, image acquisition.

1. INTRODUCTION

Breast density has consistently been shown to be an independent predictor of breast cancer risk.[1,2] Recent studies have demonstrated that combining radiomic texture features with mammographic density results in an even better assessment of breast cancer risk.[3,4] This paper explores a different application for radiomic texture feature calculations; namely, evaluating how closely the breast parenchymal patterns in an anthropomorphic phantom match a clinical population.

In our previous work, we developed a computational model of the breast in which multiple compartments of dense tissue are grown from seed points in voxel phantoms.[5,6] The user can vary parameters controlling the size and shape of the phantom, as well as the percent density and spatial arrangement of dense tissue.[7] A key advantage of this model is that a population of virtual phantoms[8] can be simulated quickly on a graphics processing unit (GPU).

A physical phantom based off this model was 3D printed by CIRS (Computerized Imaging Reference Systems, Inc., Norfolk, VA) under license from the University of Pennsylvania. The CIRS phantom models a 50 mm thick breast under compression (450 mL by volume) with a volumetric density of 17%.[9] The phantom can be used in both 2D digital mammography (DM) and 3D digital breast tomosynthesis (DBT). The phantom was 3D printed in sections (slabs), allowing clusters of calcium oxalate to be inserted within the thickness of the phantom; these are surrogates for calcification clusters.[10]

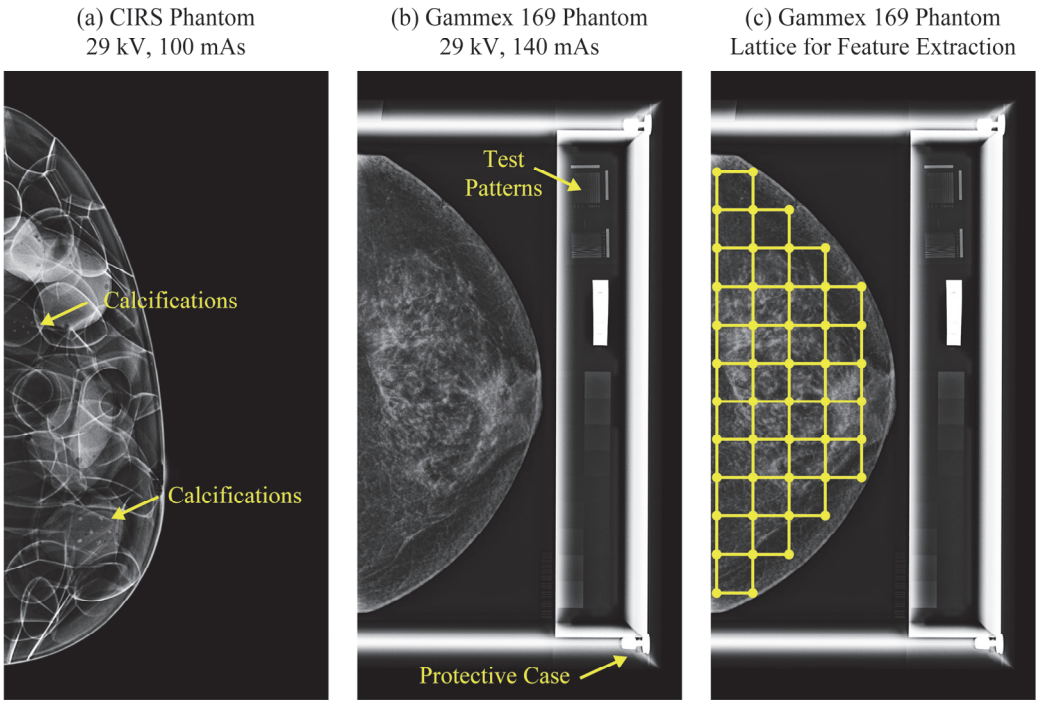

Figure 1. (a) The CIRS phantom was 3D printed from a computational breast model. (b) The Gammex 169 phantom was derived from an actual patient's mammogram. There are test patterns adjacent to the phantom; these were not analyzed for the purpose of this study. (c) The breast area was partitioned into a lattice of square windows (6.3 mm × 6.3 mm) for calculation of radiomic features. Although these calculations were done in raw DM images, processed DM images are shown.

In a previous study, Cockmartin *et al*. calculated power spectra in 2D and 3D images of the CIRS phantom, and showed that the power-law coefficients were in agreement with the values derived from a clinical population.[9] In radiomics, there are a multitude of additional features that can be used to validate the texture of a phantom. In this paper, 341 radiomic features are calculated in the CIRS phantom and compared against a clinical population. We also investigate how the texture of the CIRS phantom compares against a phantom derived from an actual patient's mammogram[11] ("Rachel, Gammex 169, Madison, WI), which by nature is expected to be highly realistic. For the purpose of this paper, all radiomics calculations are done exclusively for DM, since the Gammex 169 phantom was developed specifically for DM and not DBT.

2. METHODS

2.1 X-Ray Acquisitions of Phantoms

DM images of the two phantoms (CIRS and Gammex 169) were acquired with a Selenia Dimensions system (Hologic Inc., Bedford, MA) with a W/Rh target-filter combination (Figure 1). Images were acquired over a number of different kV and mAs combinations; the auto-timing curves illustrating the effect of kV are shown in Figure 2. A subset of these technique settings was chosen for the purpose of validating the texture of the phantoms. We based the choice of acquisition settings off of data tables for the automatic exposure control settings for a breast with comparable thickness (50 mm) to the phantoms; the appropriate kV is 29 kV for a W/Rh target-filter combination. Additional kV settings in ± 1 kV increments relative to 29 kV were also analyzed. These images were acquired in "Manual" mode at mAs settings designed to match the auto-timing curves. Since the system supports a discrete set of mAs values in "Manual" mode, the closest mAs settings were chosen (Table 1). Two cranial-caudal (CC) images were acquired at each technique setting; these were used for reproducibility analysis. Hence there were six acquisitions per phantom.

Table 1. DM technique settings for each phantom are summarized below. The target-filter combination was W/Rh.

	mAs Setting (28 kV)	**mAs Setting (29 kV)**	**mAs Setting (30 kV)**
CIRS Phantom	120 mAs	100 mAs	95 mAs
Gammex 169 Phantom	160 mAs	140 mAs	120 mAs

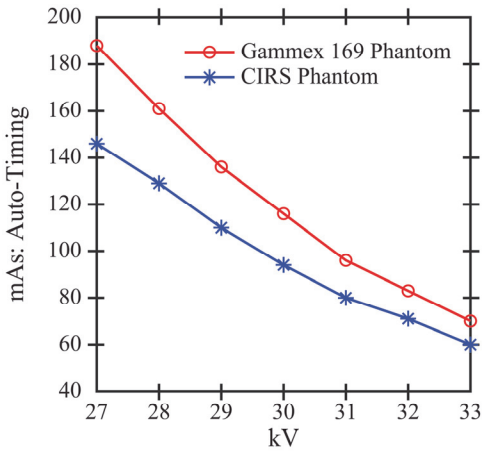

Figure 2. DM images of the two phantoms were acquired at auto-timed technique settings. As the kV increases, there is greater x-ray penetration and hence the mAs (relative number of x-ray photons) is reduced.

2.2 Overview of Clinical Data Set

DM images (CC views) were also analyzed from 1,000 women with negative screening exams at the University of Pennsylvania (Table 2). The images were acquired with Selenia Dimensions systems between 9/1/2014 and 12/31/2014. This research was approved by the Institutional Review Board at the University of Pennsylvania and was compliant with the Health Insurance Portability and Accountability Act. Since previous work demonstrated that radiomic features are dependent on breast thickness under compression[12], we compared the phantom data against the subset of clinical data with comparable thickness (±10 mm relative to a 50 mm thick phantom).

2.3 Calculation of Radiomic Texture Features

Radiomic features were calculated in raw ("FOR PROCESSING") DM images. As the first step in these calculations, the breast outline was segmented with LIBRA (Laboratory for Individualized Breast Radiodensity Assessment), a software tool.[13] Next, the breast area was partitioned into a regular lattice of square windows [Figure 1(c)]. Each feature was calculated separately in each window. These values were in turn averaged across all windows, resulting in a single image-wise value for each feature. A total of 341 features were calculated; *i.e.*, 12 gray-level histogram, 7 co-occurrence, 7 run length, 2 fractal dimension, 32 Gabor Wavelet, 36 local binary pattern, 125 Laws, and 120 co-occurrence Laws features.[14-18]

The window size used in the lattice for these feature calculations was 6.3 mm. A previous work by Zheng *et al.* considered the effect of varying the window size between 6.3 mm and 25.5 mm.[3] They found that the smallest window size (6.3 mm) yields the highest area under the receiver-operating-characteristic curve in case-control classification calculations.

Table 2. Demographic information derived from the data set of 1,000 women with negative screening exams is summarized below.

Age	< 40 y	29 (2.9 %)
	40-49 y	255 (25.5%)
	50-59 y	292 (29.2%)
	60-69 y	279 (27.9 %)
	≥ 70 y	145 (14.5%)
BI-RADS® Density	Type a	114 (11.4%)
	Type b	553 (55.3%)
	Type c	311 (31.1%)
	Type d	22 (2.2%)
Ethnicity	African American	463 (46.3%)
	Caucasian	441 (44.1%)
	Other/Unknown	96 (9.6%)

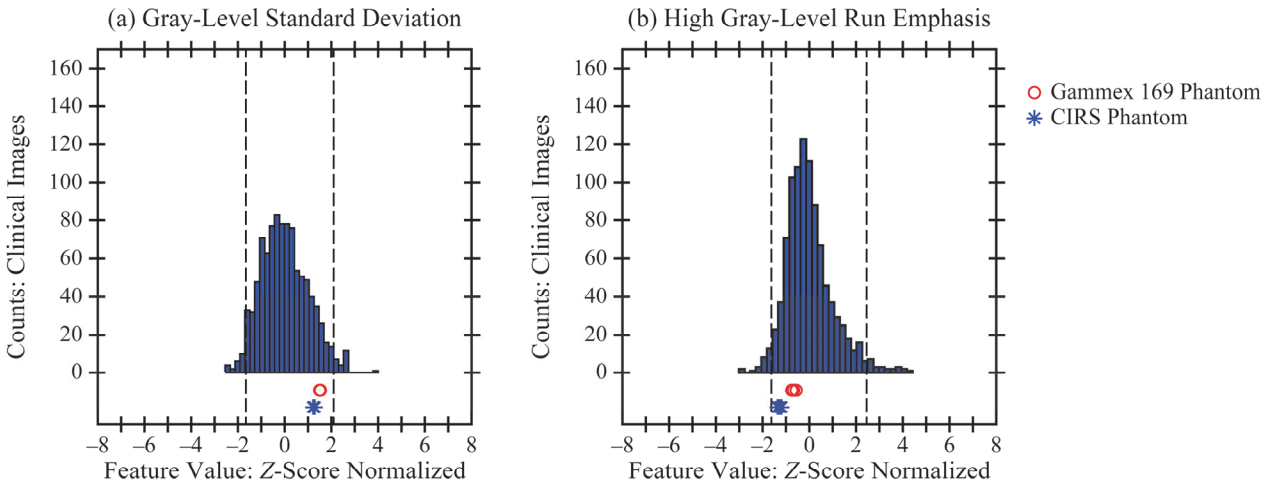

Figure 3. Each phantom was found to have realistic texture in terms of these two features. The phantom data points derived from six images are all within the middle 95% of the clinical distribution. Dashed lines denote the 2.5th and 97.5th percentiles of the clinical distribution.

2.4 Analysis of Textural Realism of Phantoms

For the two phantoms, the textural realism of each feature was defined based on the middle 95% of the clinical distribution; this was considered to be a realistic range of values for a feature. More specifically, a feature was considered realistic if all six data points derived from phantom images were between the 2.5th and 97.5th percentiles of the clinical distribution. By contrast, a feature was considered unrealistic if the percentile ranks of at least one of the six phantom data points was below 2.5% or above 97.5% (dashed vertical lines in Figures 3-5). Note that other definitions of realism exist, and that different conclusions may result from the use of alternate definitions of realism. For example, in Figure 3, both phantoms are deemed realistic by our metric, but if we defined textural realism in terms of closeness to the 50th percentile of the clinical distribution, then the CIRS phantom is more realistic in terms of the gray-level standard deviation and the Gammex 169 phantom is more realistic in terms of high gray-level run emphasis.

3. RESULTS

3.1 Calculations of Textural Realism

For each feature, the distribution of values in the clinical data set was *Z*-score normalized and plotted as a histogram (Figures 3-5). This normalization was also applied to the six phantom data points. To illustrate examples of realistic texture in both phantoms, standard deviation (a gray-level feature) and high gray-level run emphasis (a run length feature) are shown in Figure 3. In these examples, the six data points derived from the phantom acquisitions are clustered over a narrow range of values within the middle 95% of the clinical distribution.

Table 3. Summary statistics for each phantom were calculated separately by feature family.

Feature Family (Number of Features)	Realistic Features in CIRS Phantom	Realistic Features in Gammex 169 Phantom
Co-occurrence (7)	7 (100%)	3 (42.86%)
Co-occurrence Laws (120)	106 (88.33%)	87 (72.50%)
Fractal Dimension (2)	1 (50%)	0 (0%)
Gabor Wavelet (32)	32 (100%)	32 (100%)
Gray Level (12)	12 (100%)	12 (100%)
Laws (125)	111 (88.80%)	93 (74.40%)
LBP (36)	29 (80.56%)	29 (80.56%)
Run Length (7)	7 (100%)	5 (71.43%)

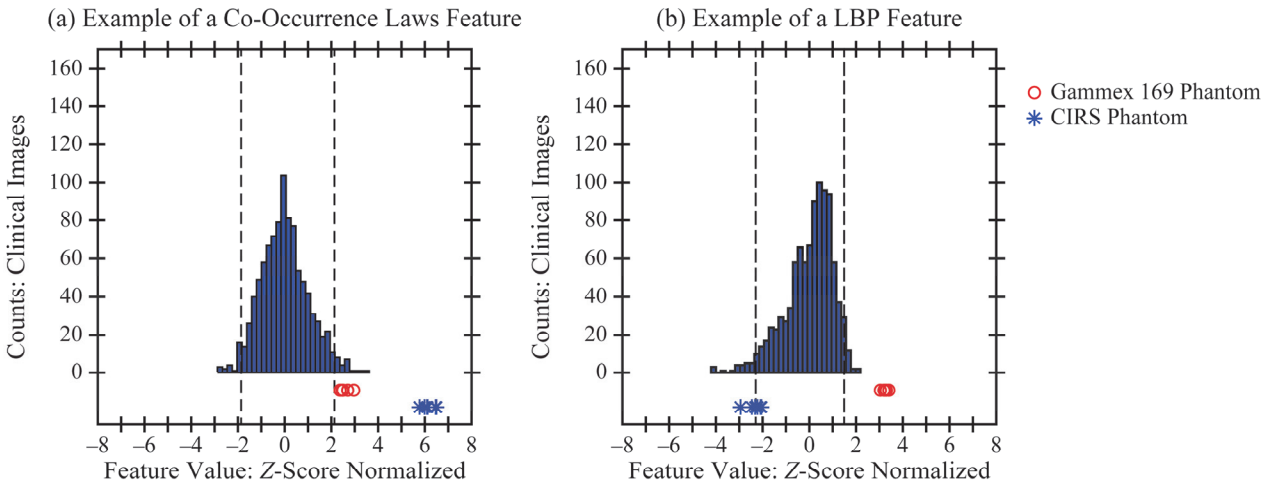

Figure 4. The phantoms were found to have unrealistic texture in terms of these two features. At least one of the six phantom data points is outside the middle 95% of the clinical distribution.

To illustrate the opposite result (unrealistic texture in both phantoms), two additional examples are shown in Figure 4. In some features, all six phantom data points were outside the middle 95% of the clinical distribution, as can be seen in one of the co-occurrence Laws features [Figure 4(a)]. The texture was also considered unrealistic if any subset of phantom data points was outside the middle 95% of the clinical distribution [Figure 4(b)].

3.2 Summary Statistics

The CIRS phantom was found to have realistic texture in terms of 305 features out of 341 (89.44%). By contrast, the Gammex 169 phantom was found to have realistic texture in terms of 261 features out of 341 (76.54%). These results can be analyzed in more detail on the basis of individual feature families (Table 3). The phantoms showed realistic texture in terms of all the gray-level and Gabor Wavelet features. The phantoms showed unrealistic texture in terms of some measures of fine structural detail.

It is also useful to create a confusion matrix (a 2 × 2 table) summarizing the results for each phantom (Table 4). Both phantoms were shown to have realistic texture in terms of 239 features (70.09%) and unrealistic texture in terms of 14 features (4.11%). In addition, there are 88 features (25.81%) for which the texture is realistic in one phantom but not the other; Figure 5 shows examples of these features.

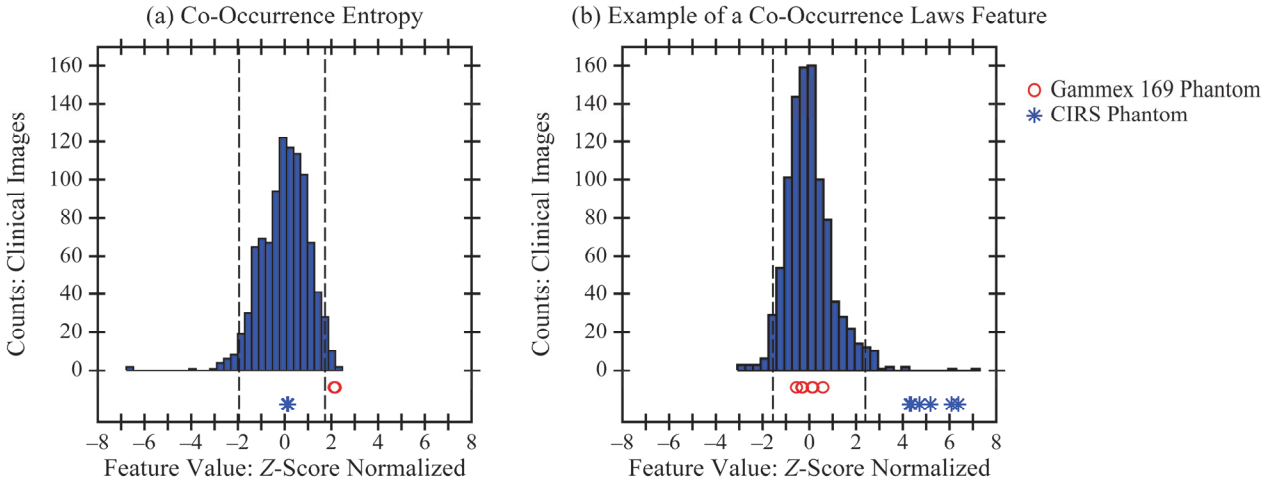

Figure 5. In some features, only one of the two phantoms was shown to have realistic texture; for example, the CIRS phantom in terms of co-occurrence entropy and the Gammex 169 phantom in terms of a Co-Occurrence Laws features.

Table 4. Summary statistics for each phantom can be analyzed with a confusion matrix.

Gammex 169 Phantom

CIRS Phantom	Realistic	Unrealistic	
Realistic	239 (70.09%)	66 (19.35%)	305 (89.44%)
Unrealistic	22 (6.45%)	14 (4.11%)	36 (10.56%)
	261 (76.54%)	80 (23.46%)	341 (100%)

4. DISCUSSION AND CONCLUSION

This paper evaluates the textural realism of two phantoms for DM. One would expect the Gammex 169 phantom to have realistic texture by its very nature, since it was created from an actual patient's mammogram. In this paper, we offer a validation of the textural realism of this phantom, and show that the CIRS phantom also has realistic texture. We conclude that phantoms based off a computational model can indeed have realistic texture.

In the years since the CIRS phantom was 3D printed, there have been advancements in the voxel phantom. The phantom now includes a model of tissue microstructure, which is simulated with the use of subcompartments of breast tissue designed to match the appearance of histological images.[19] Future work should investigate how the texture of the phantom changes based on the addition of these finer details.

5. ACKNOWLEDGEMENT

Support was provided by the following grants: R01CA207084 and U54CA163313 from the National Institute of Health, W81XWH-18-1-0082 from the Department of Defense Breast Cancer Research Program, and PDF17479714 from Susan G. Komen®. The content is solely the responsibility of the authors and does not necessarily represent the official views of the funding agencies.

ADAM receives research support from Hologic Inc., Barco NV, and Analogic Corporation. Also, ADAM is a shareholder and member of the scientific advisory board of Real Time Tomography, LLC. EFC receives grant support and is part of the advisory panel of Hologic Inc. EFC also receives grant support and is part of the advisory panel of iCAD Inc.

6. REFERENCES

1. Boyd NF, Rommens JM, Vogt K, et al. Mammographic breast density as an intermediate phenotype for breast cancer. *The Lancet Oncology.* 2005;6(10):798-808.
2. Boyd NF, Guo H, Martin LJ, et al. Mammographic Density and the Risk and Detection of Breast Cancer. *The New England Journal of Medicine.* 2007;356(3):227-236.
3. Zheng Y, Keller BM, Ray S, et al. Parenchymal texture analysis in digital mammography: A fully automated pipeline for breast cancer risk assessment. *Medical Physics.* 2015;42(7):4149-4160.
4. Gastounioti A, Conant EF, Kontos D. Beyond breast density: a review on the advancing role of parenchymal texture analysis in breast cancer risk assessment. *Breast Cancer Research.* 2016;18:91.
5. Chui JH, Pokrajac DD, Maidment ADA, Bakic PR. Towards Breast Anatomy Simulation Using GPUs. *Lecture Notes in Computer Science.* 2012;7361:506-513.
6. Pokrajac DD, Maidment ADA, Bakic PR. Optimized generation of high resolution breast anthropomorphic software phantoms. *Medical Physics.* 2012;39(4):2290-2302.

7. Chui JH, Zeng R, Pokrajac DD, et al. Two Methods for Simulation of Dense Tissue Distribution in Software Breast Phantoms. Paper presented at: SPIE Medical Imaging2013; Orlando, FL.
8. Barufaldi B, Bakic PR, Pokrajac DD, Lago MA, Maidment ADA. Developing Populations of Software Breast Phantoms for Virtual Clinical Trials. Paper presented at: 14th International Workshop on Breast Imaging (IWBI 2018)2018; Atlanta, GA.
9. Cockmartin L, Bakic PR, Bosmans H, et al. Power Spectrum Analysis of an Anthropomorphic Breast Phantom Compared to Patient Data in 2D Digital Mammography and Breast Tomosynthesis. *Lecture Notes in Computer Science.* 2014;8539:423-429.
10. Vieira MAC, Oliveira HCRd, Nunes PF, et al. Feasibility Study of Dose Reduction in Digital Breast Tomosynthesis Using Non-Local Denoising Algorithms. Paper presented at: SPIE Medical Imaging2015; Orlando, FL.
11. Yaffe MJ, Johns PC, Nishikawa RM, Mawdsley GE, Caldwell CB. Anthropomorphic radiologic phantoms. *Radiology.* 1986;158(2):550-552.
12. Acciavatti RJ, Hsieh M-K, Gastounioti A, et al. Validation of the Textural Realism of a 3D Anthropomorphic Phantom for Digital Breast Tomosynthesis. Paper presented at: 14th International Workshop on Breast Imaging (IWBI 2018)2018; Atlanta, GA.
13. Keller BM, Nathan DL, Wang Y, et al. Estimation of breast percent density in raw and processed full field digital mammography images via adaptive fuzzy c-means clustering and support vector machine segmentation. *Medical Physics.* 2012;39(8):4903-4917.
14. Haralick RM, Shanmugam K, Dinstein IH. Textural Features for Image Classification. *IEEE Transactions on Systems, Man, and Cybernetics.* 1973;SMC-3(6):610-621.
15. Galloway MM. Texture analysis using gray level run lengths. *Computer Graphics and Image Processing.* 1975;4(2):172-179.
16. Chu A, Sehgal CM, Greenleaf JF. Use of gray value distribution of run lengths for texture analysis. *Pattern Recognition Letters.* 1990;11(6):415-419.
17. Ojala T, Pietikäinen M, Mäenpää T. Multiresolution Gray-Scale and Rotation Invariant Texture Classification with Local Binary Patterns. *IEEE Transactions on Pattern Analysis and Machine Intelligence.* 2002;24(7):971-987.
18. Manduca A, Carston MJ, Heine JJ, et al. Texture Features from Mammographic Images and Risk of Breast Cancer. *Cancer Epidemiology, Biomarkers & Prevention.* 2009;18(3):837-845.
19. Bakic PR, Pokrajac DD, Caro RD, Maidment ADA. Realistic Simulation of Breast Tissue Microstructure in Software Anthropomorphic Phantoms. *Lecture Notes in Computer Science.* 2014;8539:348-355.

Super-Resolution in Digital Breast Tomosynthesis: Limitations of the Conventional System Design and Strategies for Optimization

Raymond J. Acciavatti[1], Trevor L. Vent[1], Bruno Barufaldi[1], E. Paul Wileyto[2],
Peter B. Noël[1], Andrew D. A. Maidment[1]
[1]University of Pennsylvania, Department of Radiology, 3400 Spruce Street, Philadelphia PA 19104
[2]University of Pennsylvania, Department of Epidemiology, Biostatistics, & Informatics,
423 Guardian Drive, Philadelphia, PA 19104
E-mail: {Raymond.Acciavatti | Trevor.Vent | Bruno.Barufaldi | epw |
Peter.Noel | Andrew.Maidment}@pennmedicine.upenn.edu

ABSTRACT

Our previous work explored the use of super-resolution as a way to improve the visibility of calcifications in digital breast tomosynthesis. This paper demonstrates that there are anisotropies in super-resolution throughout the reconstruction, and investigates new motion paths for the x-ray tube to suppress these anisotropies. We used a theoretical model of a sinusoidal test object to demonstrate the existence of the anisotropies. In addition, high-frequency test objects were simulated with virtual clinical trial (VCT) software developed for breast imaging. The simulated objects include a lead bar pattern phantom as well as punctate calcifications in a breast-like background. In a conventional acquisition geometry in which the source motion is directed laterally, we found that super-resolution is not achievable if the frequency is oriented in the perpendicular direction (posteroanteriorly). Also, there are positions, corresponding to various slices above the breast support, at which super-resolution is inherently not achievable. The existence of these anisotropies was validated with VCT simulations. At locations predicted by theoretical modeling, the bar pattern phantom showed aliasing, and the spacing between individual calcifications was not properly resolved. To show that super-resolution can be optimized by re-designing the acquisition geometry, we applied our theoretical model to the analysis of new motion paths for the x-ray tube; specifically, motions with more degrees of freedom and with more rapid pulsing (submillimeter spacing) between source positions. These two strategies can be used in combination to suppress the anisotropies in super-resolution.

Keywords: Digital Breast Tomosynthesis, Virtual Clinical Trials, Super-Resolution, Calcifications, Anthropomorphic Phantom, Fourier Transform, Image Quality, Image Reconstruction.

1. INTRODUCTION

1.1 Overview of Super-Resolution in Tomosynthesis

Many medical centers now use digital breast tomosynthesis (DBT) for breast cancer screening.[1-3] In DBT, the x-ray tube rotates in the plane of the chest wall, and a reconstruction is created from a small number of projection views (Figure 1). Since the image of an object is translated in subpixel increments between each projection, a reconstruction created with smaller pixelation than the detector is capable of super-resolution, or resolution of frequencies exceeding the alias frequency of the detector.[4,5] Super-resolution allows fine details to be visualized more clearly, including calcifications. These benefits can be achieved with either backprojection filtering[4] or iterative reconstructions[6].

With theoretical modeling, we have shown that there are some z-coordinates at which super-resolution cannot be achieved, corresponding to regularly-spaced slices in the reconstruction.[7] One of the aims of this paper is to understand how these anisotropies could impact virtual clinical trials (VCTs). A VCT is a software tool that allows for simulation of anatomical phantoms under different imaging conditions using model observers to quantify the detection of lesions (*e.g.*, calcifications) with receiver operating characteristic curves.[8] Our recent work showed that a VCT of DBT and 2D digital mammography (DM) performed extremely well in comparison with clinical data.[9] In this paper, we demonstrate that the visualization of calcifications in a VCT is impacted by the presence of the anisotropies in super-resolution. We use theoretical modeling to guide the positioning of these lesions based on the known locations of the anisotropies.

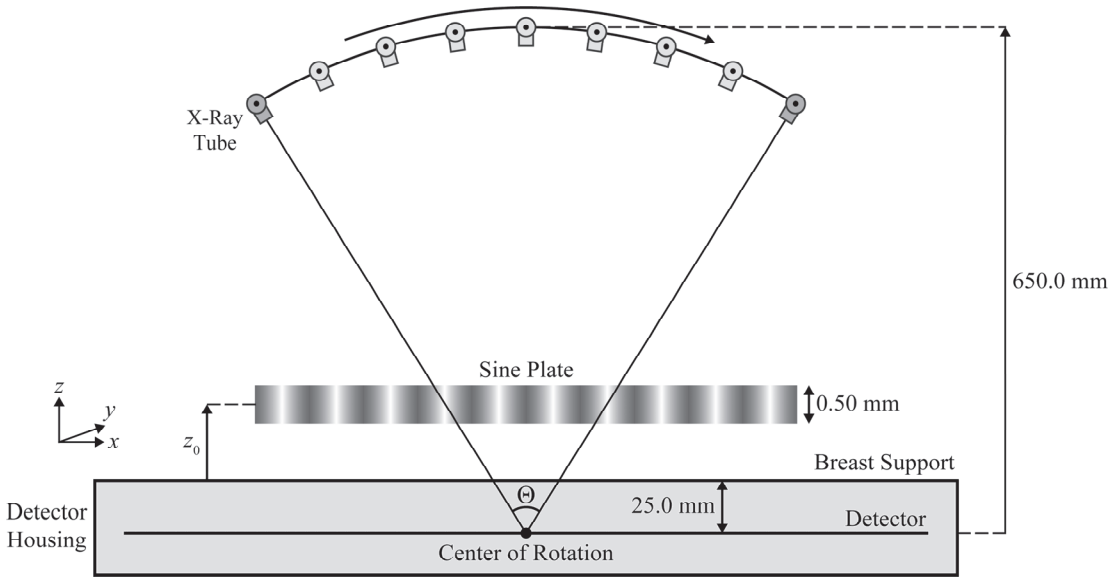

Figure 1. The sine plate is a test object for investigating the existence of super-resolution with theoretical modeling. In a conventional DBT scan, there is source motion in a circular arc in the *xz* plane; *i.e.*, the plane of the chest wall.

1.2 Design of a Next-Generation Tomosynthesis System

In our previous work, we showed that there are fewer anisotropies in a DBT system with narrowly-spaced source positions, but that it is not possible to eliminate the anisotropies entirely. Recently, we proposed a "next-generation" DBT system design in which additional source positions are clustered around the conventional positions in submillimeter increments.[10] This design can be implemented by rapidly pulsing the source during continuous motion of the x-ray tube. For frequencies oriented in the *x* direction (laterally or left-to-right in Figure 1), the anisotropies can be eliminated with the use of rapid source pulsing.

A limitation of our previous work[10] on rapid source pulsing is that the perpendicular orientation of the test frequency was not considered; *i.e.*, the posteroanterior (PA) orientation (into the plane of the page in Figure 1). In a conventional DBT system, super-resolution is not achievable in the PA direction. This idea can be illustrated with projection images of a point-like object (Figure 2). Because there is x-ray tube motion in the *x* direction (laterally), there are noticeable shifts in the image of the object between projections, and hence super-resolution is achieved in this direction. However, the shifts in the *y* direction are too small to achieve super-resolution; there is no x-ray tube motion in this direction. In this paper, we show that super-resolution can indeed be achieved in the PA direction with the use of source motion in this direction. This motion can be applied in combination with the use of rapid source pulsing to ensure that super-resolution is achieved with high quality, regardless of the orientation of the input frequency.

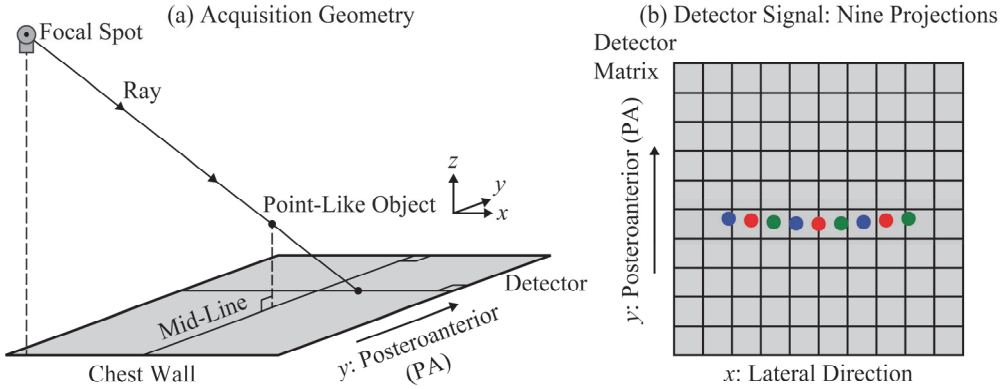

Figure 2. In clinical DBT systems, super-resolution is achieved in the *x* direction, since there is x-ray tube motion in this direction. However, super-resolution is not achieved in the *y* direction; the shifts in the object positions in this direction are minimal.

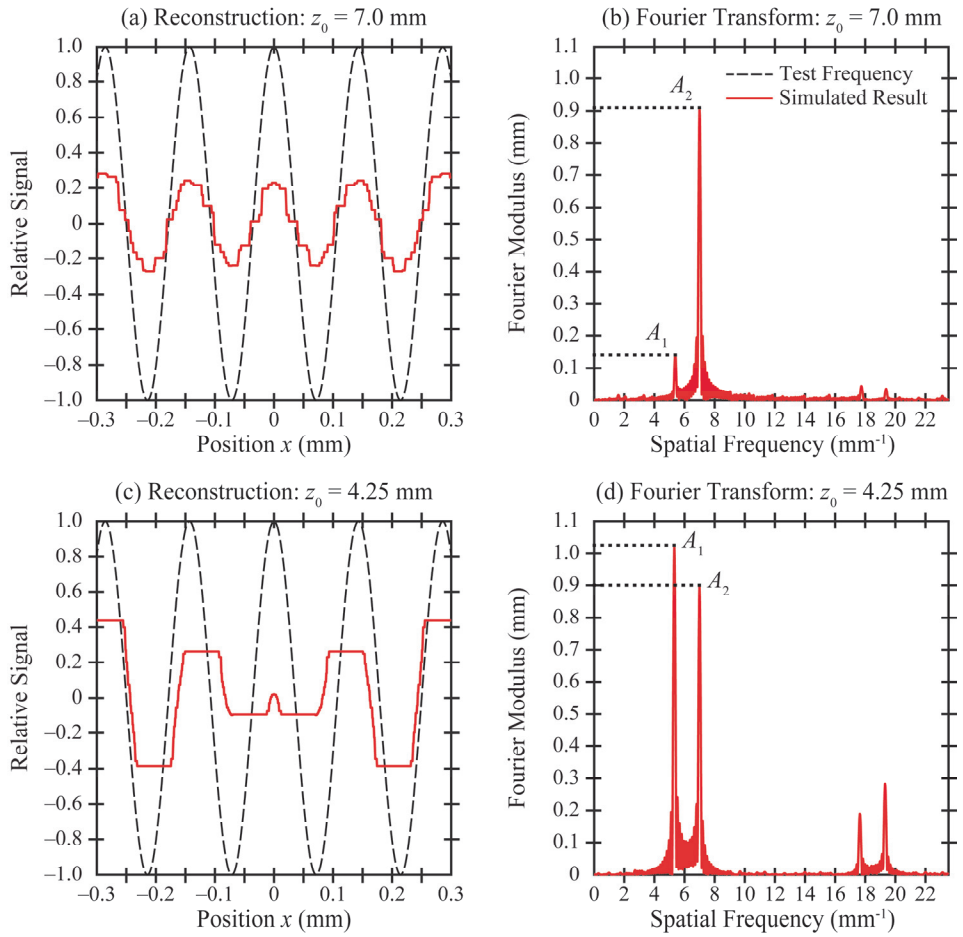

Figure 3. The Fourier transform of the reconstruction is analyzed in terms of two peaks: one at the input frequency (A_2) and one at a lower frequency (A_1). In order for super-resolution to be achieved with high quality, the ratio A_1/A_2 should be as small as possible.

2. METHODS

2.1 Identification of Anisotropies in the Conventional Design

As the first aim of this paper, we demonstrate the existence of anisotropies in the conventional system design. We apply the theoretical model of super-resolution developed in our previous work.[7] In that work, the reconstruction of a sinusoidal test object was calculated from first principles.

The input frequency is modeled separately in two directions: lateral and PA. Anisotropies are identified using the Fourier transform of the reconstruction; this is calculated over 50 cycles with 20 points sampled per cycle. To illustrate how the Fourier transform can be used to assess super-resolution, a 7.0 mm^{-1} test frequency is considered with sampling by a detector with 0.085 mm × 0.085 mm detector elements (Figure 3). The Fourier transform has a major peak at the input frequency if the object is resolved [Figure 3(b)], but has a major peak at a lower frequency if the object is aliased [Figure 3(d)]. Our previous work defined the *r*-factor as a metric to summarize the results in Fourier space.[4,7]

$$r\text{-Factor} = \frac{A_1}{A_2} \tag{1}$$

In order for super-resolution to be achieved with high quality, the *r*-factor should be as small as possible. That is, the amplitude of the low-frequency peak (A_1) should be smaller than the amplitude at the input frequency (A_2). For the purpose of this paper, the threshold for high-quality super-resolution is: *r*-factor < 1/3.

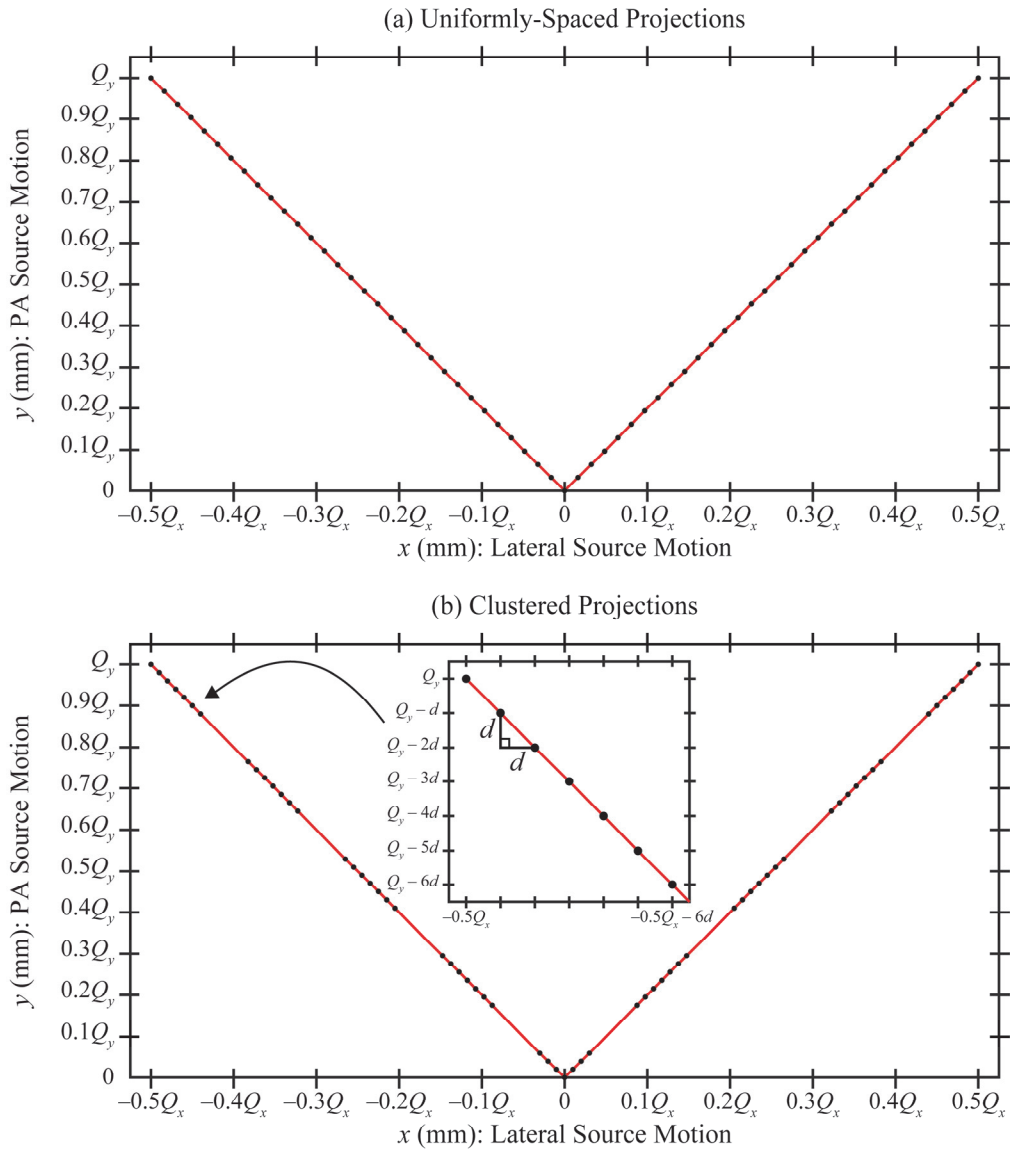

Figure 4. (a) There are 63 source positions spaced uniformly along a V-shaped trajectory. (b) The source positions are re-arranged in nine clusters in the same V-shaped trajectory. There is submillimeter spacing between the seven source positions in each cluster (d = 0.5 mm).

To identify all the coordinates of the anisotropies in the range between z_0 = 0 and z_0 = 50.0 mm, we generated a plot of r-factor as a function of z_0. For this simulation, the sine wave was centered at the position 25.0 mm anterior to the chest wall along the mid-line defined in Figure 2. The acquisition parameters for this simulation are summarized in Table 1.

2.2 VCT Simulations of Bar Pattern Phantom and Calcifications

VCT software was then used to validate the position of the anisotropies expected from theoretical modeling. The acquisition parameters in this simulation are detailed in Table 1. First, we simulated a bar pattern phantom with 0.070 mm cubic voxels, a thickness of 0.070 mm, and a frequency of 7.0 mm^{-1} oriented laterally (parallel with the source motion); *i.e.*, the same orientation as Figure 1. Since the input frequency is higher than the alias frequency of the detector (5.9 mm^{-1} in a 0.085 mm detector), this object can be used to investigate super-resolution.

Table 1. The acquisition parameters for theoretical modeling and VCT simulations are summarized below.

Acquisition Parameter	Theoretical Modeling: Conventional DBT	VCT Simulation: Conventional DBT	Theoretical Modeling: Next-Generation DBT
Source Motion	Circular Arc (*xz* Plane)	Linear (*x*): Constant *z*	V-Shaped: Constant *z*
Source-to-Image Distance	650.0 mm (Central Projection)	621.0 mm	650.0 mm
Number of Projections	15	15	63
Range of Source Motion	$\Theta = 17.7°$ (200.0 mm in *x*)	182.7 mm (in *x*)	200.0 mm (*x*), 100.0 mm (*y*)

Secondly, punctate calcifications[11] were simulated in an anthropomorphic voxel phantom.[12] The phantom was positioned in such a way that the inferior surface was in contact with the detector. Each calcification was modeled by a single voxel with dimensions of 0.070 mm in each direction. There were 25 calcifications arranged linearly in the direction of the source motion. Reconstructions for both the bar pattern and calcifications were prepared with Piccolo™ (Real Time Tomography, LLC, Villanova, PA).[13]

The calcification size and composition were chosen with care. The linear dimension (0.070 mm) was chosen to ensure that the frequency of the array of calcifications was greater than the alias frequency of the detector (5.9 mm^{-1}). This linear dimension is smaller than the smallest calcification (0.16 mm) within the Gammex 156 American College of Radiology (ACR) Mammography Accreditation Phantom; however, the shape of the calcifications in the ACR phantom is unspecified and the volume is less than a cube of that size. In our other work[14], we typically use cubic calcifications with dimensions 0.001 mm^3, 0.002 mm^3, and 0.003 mm^3, with weighting factors (fraction by mass) between 10% and 100% hydroxyapatite. These calcifications are equivalent in volume to spherical calcifications of diameters 0.124, 0.156, and 0.180 mm. In this paper, we use a $(0.070\ mm)^3$ calcification with a weighting factor of 100%, which has the same attenuation as a 0.124 mm diameter calcification with a weighting factor of 0.34, consistent with our other VCTs.

2.3 Modeling A New System Design

Next, we investigated a "next-generation" system design. The number of projections (63) is well above the number used clinically (Table 1); this is known from our previous work to improve the quality of super-resolution.[10] The design modeled in this paper differs from our previous work in that we model PA source motion; *i.e.*, an additional degree of freedom in the *y* direction. The motion follows a V-shape (Figure 4). The ranges of source motion in the lateral and PA directions (Q_x and Q_y) are 200.0 mm and 100.0 mm, respectively. The range of 200.0 mm in the *x* direction is similar to the conventional system described in Section 2.1.

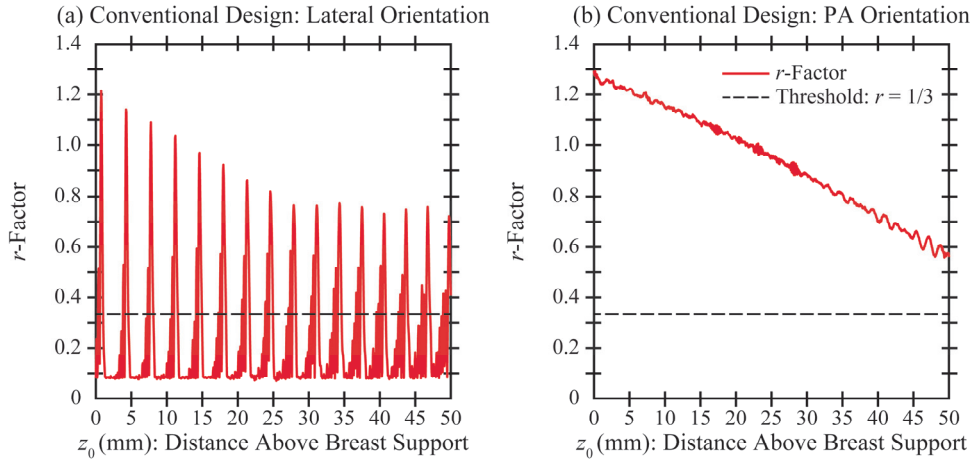

Figure 5. To achieve super-resolution with high quality, the *r*-factor should be as small as possible (below the threshold of 1/3 for the purpose of this paper). The coordinates of the anisotropies differ based on the orientation of the input frequency.

Figure 6. VCT simulations of a 7.0 mm^{-1} bar pattern phantom illustrate the z-dependency of super-resolution in the reconstruction.

For the same V-shaped motion, we investigated two acquisition geometries, each differing in terms of the choice of source positions. In one scan, we applied the principle of rapid source pulsing [Figure 4(b)], which was proposed in our previous work.[10] The source positions were arranged in nine sets of clusters with seven source positions per cluster (63 source positions in total). Within each cluster, the spacing (d) between the source positions was 0.50 mm in each direction. By contrast, in a second scan, there was equal spacing between all 63 source positions [Figure 4(a)]. We investigated whether the use of clustering offers a benefit over the use of uniform spacing. Like the simulations described in Section 2.1, we calculated the r-factor to determine which of these two acquisition geometries offers the best image quality over the broadest range of positions (z_0).

3. RESULTS

3.1 Modeling the Conventional System Design

First, image quality in a conventional DBT system was modeled by the r-factor (Figure 5). Anisotropies are present in both orientations of the input frequency. In the lateral orientation, super-resolution is not achieved at the z-coordinates at which the r-factor peaks sharply. In the PA orientation, super-resolution is not achieved with high quality anywhere; the r-factor is above the threshold of 1/3. In summary, these results illustrate the limitations of current clinical systems.

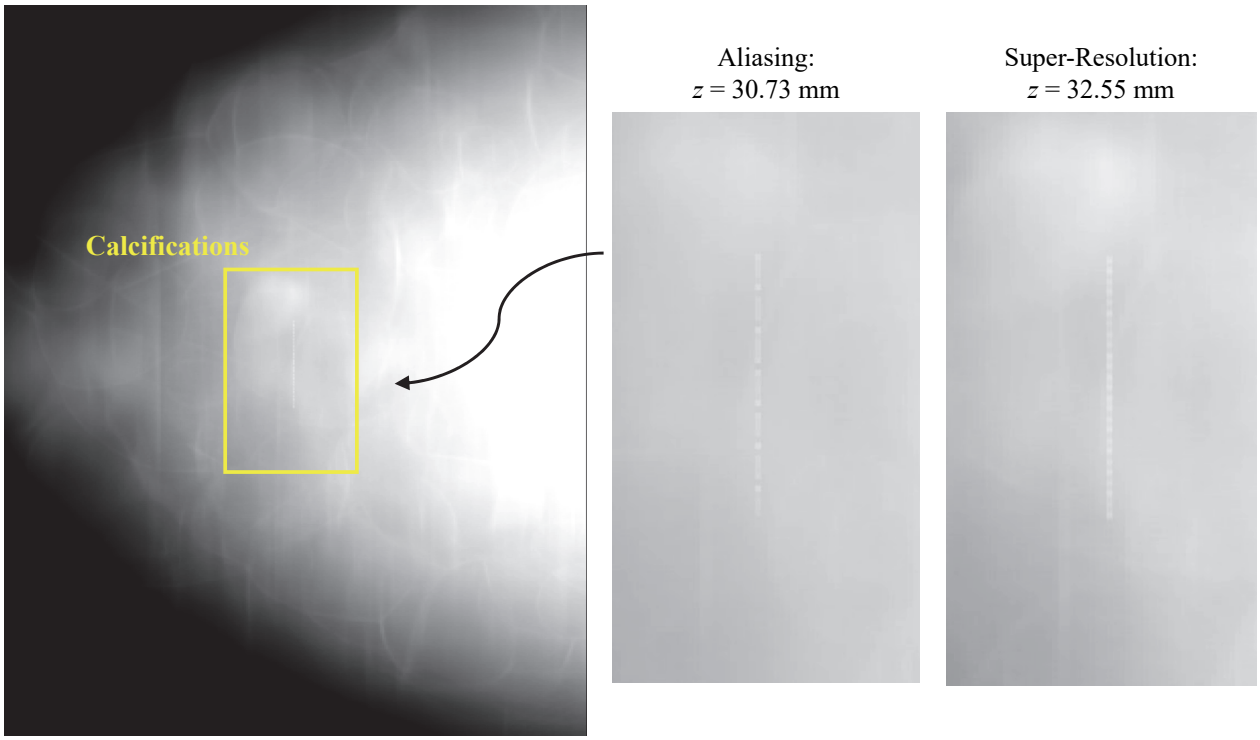

Figure 7. The ability to resolve individual punctate calcifications in a linear array is dependent on the positioning of the cluster.

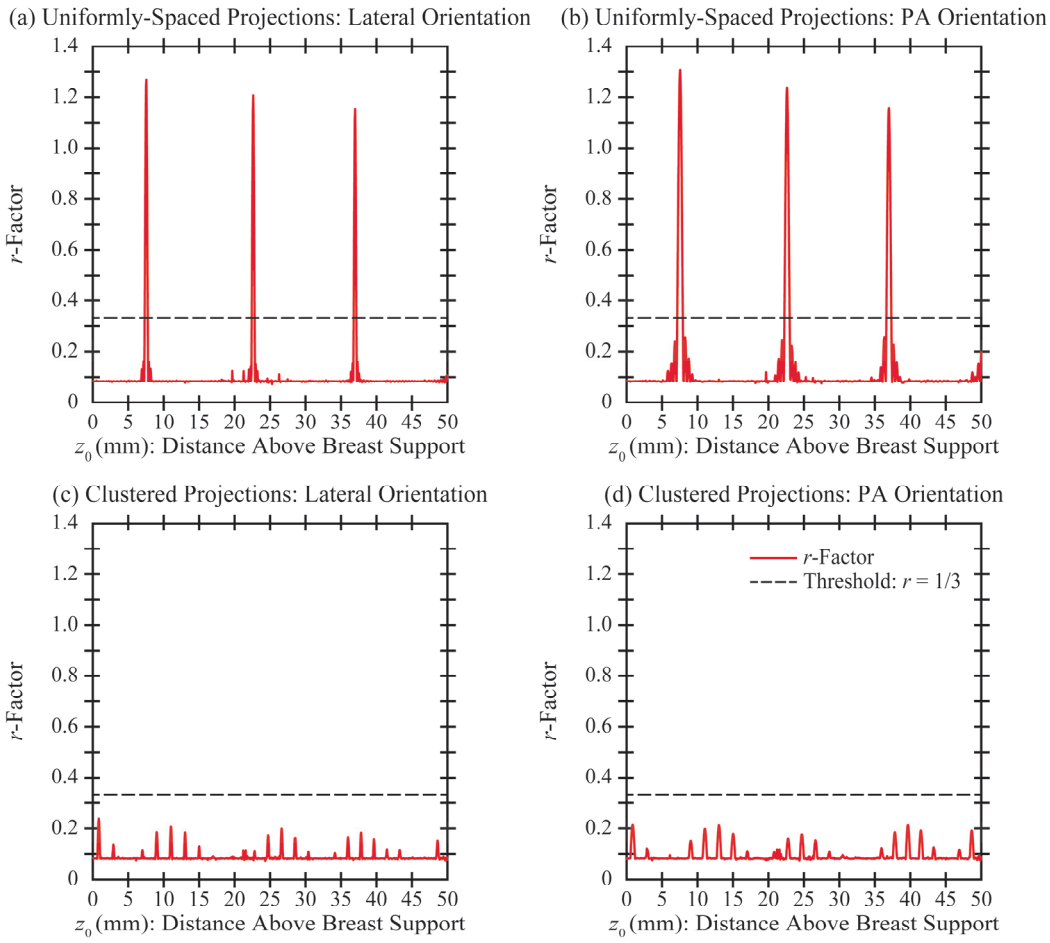

Figure 8. A DBT system is modeled with V-shaped source motion and 63 projections (well above the number of projections used clinically). To eliminate the anisotropies, the source positions should be arranged in clusters; this ensures that the *r*-factor is below 1/3 (the threshold for high-quality super-resolution).

3.2 VCT Simulations of Bar Pattern Phantom and Calcifications

Next, the bar pattern phantom and calcifications were simulated with VCT software in a conventional acquisition geometry (Table 1). This geometry differs slightly from the one analyzed with theoretical modeling (Section 3.1) in that the orbit of the x-ray tube does not follow an arc in the *xz* plane. Instead, the source is translated in only one direction (*x*) at constant *z*. This motion is consistent with the next-generation tomosynthesis (NGT) system, which we built for research use to investigate different acquisitions geometries for DBT.[15]

With theoretical modeling of the *r*-factor, a plot similar to Figure 5(a) can be created to identify anisotropies in this acquisition geometry. It can be shown, for example, that there is an anisotropy at the position 30.73 mm above the detector. At this position, the bar pattern phantom shows aliasing (Figure 6), and it is not possible to resolve each individual calcification in the reconstruction (Figure 7). However, super-resolution is supported at other positions in the reconstruction; for example, at the coordinate 32.55 mm above the detector. Here, the bar pattern phantom is resolved and each individual calcification is discernable.

3.3 Modeling A New System Design

Finally, the two V-shaped acquisition geometries were analyzed with theoretical modeling (Figure 8). Unlike the conventional acquisition geometry, super-resolution can indeed be achieved in the PA orientation; this is due to the use of PA source motion, which introduces subpixel sampling gain in that direction. The disadvantage of having uniform spacing between projections is that there are anisotropies; *i.e.*, three peaks in the *r*-factor [Figure 8(a)-(b)]. In order for the anisotropies to be eliminated, the source positions should be re-arranged in clusters [Figure 8(c)-(d)]; this design ensures that the *r*-factor is below 1/3 at all positions in the reconstruction.

4. DISCUSSION AND CONCLUSION

In our previous work, we showed that DBT is capable of super-resolution, but that clinical systems are not yet designed to optimize this effect.[4,7] There are regularly-spaced positions in the *z* direction at which super-resolution is not achievable. This paper validates the VCT software as a tool to simulate the anisotropies. We also show that the appearance of calcifications can be distorted by the presence of anisotropies; this could potentially impact the way calcifications are characterized by a radiologist.

A design for optimizing super-resolution was proposed in our previous work.[10] We modeled a system with additional source positions clustered around the conventional positions in submillimeter increments, and found that super-resolution is achieved everywhere in the reconstruction. A limitation of our previous work is that we only considered frequencies oriented laterally (Figure 1). In this paper, the PA orientation is also analyzed. Anisotropies in both orientations can be eliminated by applying the use of clustering in combination with PA motion; *i.e.*, an additional degree of freedom in the source motion.

Our previous work demonstrated that the use of PA source motion is also beneficial in other imaging tasks. In clinical DBT systems, there is a cone-beam artifact in the PA direction.[16] With Defrise phantoms, we showed that this artifact can be suppressed with the use of PA source motion.[15,17] Another advantage of PA source motion is that the accuracy of the breast outline segmentation in the reconstruction is improved.[18] The air gap between the breast support and the anterior aspect of the breast is visualized more clearly with the PA projection views.

In our previous work, we investigated a new design for the detector (motion in the *z* direction) as an alternative strategy for optimizing super-resolution.[7] In order for this strategy to be implemented clinically, it may be necessary to increase the thickness of the detector housing, which could be cumbersome for patient positioning. The advantage of the design proposed in this paper is that the detector can remain stationary during the scan. This design will require a detector capable of a high frame rate, since the number of projection views (63) exceeds the number that is typically used clinically. Also, the radiation dose per projection will need to be reduced so that the total dose of the scan is unchanged.

5. ACKNOWLEDGEMENT

We thank Johnny Kuo, Susan Ng, and Peter Ringer of Real Time Tomography (RTT) for technical assistance with Piccolo™. Andrew D. A. Maidment is a shareholder of RTT, and is a member of the scientific advisory board. Support was provided by the following grants: W81XWH-18-1-0082 from the Department of Defense Breast Cancer Research Program, IRSA 1016451 from the Burroughs Wellcome Fund, 1R01CA196528 from the National Institute of Health, and IIR13264610 from Susan G. Komen®. In addition, equipment support was provided by Analogic Inc., Barco NV, and RTT. The content is solely the responsibility of the authors and does not necessarily represent the official views of the funding agencies.

6. REFERENCES

1. Friedewald SM, Rafferty EA, Rose SL, et al. Breast Cancer Screening Using Tomosynthesis in Combination With Digital Mammography. *Journal of the American Medical Association.* 2014;311(24):2499-2507.
2. Sechopoulos I. A review of breast tomosynthesis. Part I. The image acquisition process. *Medical Physics.* 2013;40(1):014301-014301 to 014301-014312.
3. Sechopoulos I. A review of breast tomosynthesis. Part II. Image reconstruction, processing and analysis, and advanced applications. *Medical Physics.* 2013;40(1):014302-014301 to 014302-014317.
4. Acciavatti RJ, Maidment ADA. Observation of super-resolution in digital breast tomosynthesis. *Medical Physics.* 2012;39(12):7518-7539.
5. Acciavatti RJ, Maidment ADA. Investigating the Potential for Super-Resolution in Digital Breast Tomosynthesis. Paper presented at: SPIE Medical Imaging2011; Lake Buena Vista, FL.
6. Lu Y, Chan H-P, Wei J, Hadjiiski L, Samala R. Study of Image Quality in Digital Breast Tomosynthesis by Subpixel Reconstruction. Paper presented at: SPIE Medical Imaging2013; Lake Buena Vista, FL.
7. Acciavatti RJ, Wileyto EP, Maidment ADA. Modeling Acquisition Geometries with Improved Super-Resolution in Digital Breast Tomosynthesis. Paper presented at: SPIE Medical Imaging2016; San Diego, CA.

8. Barufaldi B, Higginbotham D, Bakic PR, Maidment ADA. OpenVCT: A GPU-Accelerated Virtual Clinical Trial Pipeline for Mammography and Digital Breast Tomosynthesis. Paper presented at: SPIE Medical Imaging2018; Houston, TX.

9. Bakic PR, Barufaldi B, Higginbotham D, et al. Virtual Clinical Trial of Lesion Detection in Digital Mammography and Digital Breast Tomosynthesis. Paper presented at: SPIE Medical Imaging2018; Houston, TX.

10. Acciavatti RJ, Noël PB, Maidment ADA. Proposing Rapid Source Pulsing for Improved Super-Resolution in Digital Breast Tomosynthesis. Paper presented at: SPIE Medical Imaging2020 (accepted); Houston, TX.

11. Lanyi M. Chapter 4: Calcifications Within the Lobular and Ductal System of the Breast. *Diagnosis and Differential Diagnosis of Breast Calcifications*. Berlin: Springer-Verlag; 1988:29-143.

12. Pokrajac DD, Maidment ADA, Bakic PR. Optimized generation of high resolution breast anthropomorphic software phantoms. *Medical Physics*. 2012;39(4):2290-2302.

13. Kuo J, Ringer PA, Fallows SG, Bakic PR, Maidment ADA, Ng S. Dynamic Reconstruction and Rendering of 3D Tomosynthesis Images. Paper presented at: SPIE Medical Imaging2011; Lake Buena Vista, FL.

14. Barufaldi B, Vent TL, Acciavatti RJ, et al. Determining the Optimal Angular Range of the X-Ray Source Motion in Tomosynthesis Using Virtual Clinical Trials. Paper presented at: SPIE Medical Imaging2020 (accepted); Houston, TX.

15. Eben JE, Vent TL, Choi CJ, et al. Development of a Next Generation Tomosynthesis System. Paper presented at: SPIE Medical Imaging2018; Houston, TX.

16. Acciavatti RJ, Mannherz W, Nolan M, Maidment ADA. An Alternate Design for the Defrise Phantom To Quantify Resolution in Digital Breast Tomosynthesis. Paper presented at: SPIE Medical Imaging2017; Orlando, FL.

17. Acciavatti RJ, Barufaldi B, Vent TL, Wileyto EP, Maidment ADA. Personalization of X-Ray Tube Motion in Digital Breast Tomosynthesis Using Virtual Defrise Phantoms. Paper presented at: SPIE Medical Imaging2019; San Diego, CA.

18. Acciavatti RJ, Rodriguez-Ruiz A, Vent TL, et al. Analysis of Volume Overestimation Artifacts in the Breast Outline Segmentation in Tomosynthesis. Paper presented at: SPIE Medical Imaging2018; Houston, TX.

MRMC ROC Analysis of Calcification Detection in Tomosynthesis Using Computed Super Resolution and Virtual Clinical Trials

Bruno Barufaldi*, Trevor L. Vent, Raymond J. Acciavatti, Predrag R. Bakic, Peter B. Noël and Andrew D. A. Maidment

Department of Radiology, University of Pennsylvania, Philadelphia, United States.
*Bruno.Barufaldi@pennmedicine.upenn.edu

ABSTRACT

Digital breast tomosynthesis (DBT) reduces breast tissue overlap, which is a major limitation of digital mammography. However, DBT does not show significant improvement in calcification detection, because of the limited angle and small number of projections used to reconstruct the 3D breast volume. Virtual clinical trials (VCTs) were used to evaluate the benefits of computed super resolution (SR) and the optimal combination of the acquisition parameters to improve calcification detection in DBT. We simulated calcifications that were embedded into software breast phantoms. DBT projections of the breast phantoms with and without calcifications were synthesized. We simulated detector elements of 0.085 mm and reconstructed DBT images using 0.0425 mm and 0.085 mm voxels. Channelized Hotelling observers (CHOs) were trained and tested to simulate five virtual readers. Differences in area under the curve (AUC) between SR images and images synthesized with 0.085 mm voxels were calculated using the one-shot multiple-reader multiple-case receiver operator curve (MRMC ROC) methods. Our preliminary results show that the differences in AUC is approximately 0.021 and 0.016 for DBT images simulated using one- and two-voxel calcifications, respectively. SR shows a substantial improvement for calcification detection in DBT. The impact of SR on calcification detection is more prominent for small calcifications.

Keywords: virtual clinical trial; multiple-reader, multiple-case; digital breast tomosynthesis; super resolution.

1. INTRODUCTION

Digital breast tomosynthesis (DBT) has been shown to reduce recall rates by resolving overlapped breast structures not seen on digital mammography.[1] However, there is some concern that DBT may not depict small breast structures, such as calcifications,[2,3] due to the limited angle and small number of tomographic projections. Alternative imaging methods are required to improve calcification detection and to maximize the benefits of mammography screening with DBT.

Computed super-resolution (SR) is a reconstruction method with pixels that are smaller than the detector element size; superior spatial resolution is achieved through the elimination of aliasing and alteration of the sampling function imposed by the reconstructed pixel aperture.[4] However, this reconstruction method is not well explored by others because it can increase the image size and time to reconstruct tomographic projections.

We have developed an open-source Virtual Clinical Trial (Open VCT) framework that allows the projection and reconstruction of DBT images in real-time. Our VCT framework has been used to evaluate and to optimize imaging systems by performing simulations of the human breast anatomy, DBT image acquisition, and image interpretation.[5–7]

We have shown in a previous study that calcification detection in DBT is substantially affected by reconstructed voxel size, detector element size, and tube motion.[8] However, the optimal combination of the acquisition parameters in DBT is still under investigation.[9] VCTs can be used to investigate the limit of calcification detection and to evaluate promising imaging designs, avoiding the pursuit of inefficient DBT acquisition parameters.[8,10]

In this work, we present a VCT method for determining the most suitable reconstructed voxel size for calcification detection in DBT. Voxelized single calcifications of 100 and 200 μm³ were inserted into software breast phantoms. Fifteen DBT projections of the breast phantoms with and without lesions were synthesized simulating the imaging geometry of the next generation of tomosynthesis (NGT) system. We simulated and varied the reconstructed voxel size using 0.085 mm and 0.0425 mm, with 0.085 mm detector elements (del). We also simulate five virtual readers to evaluate the calcification detection using multiple-reader, multiple-case (MRMC) receiver operator curve (ROC) analyses.[11]

2. MATERIALS & METHODS

2.1 DBT Image Simulations

Virtual anthropomorphic breast phantoms were developed to simulate healthy breast anatomy using an efficient recursive partitioning method.[12,13] The recursive partitioning method supports a large number of breast simulations in terms of simulations per GPU-hour.[5] In this work, we simulated 80 breast phantoms with 700mL and uncompressed breast thickness of 126.6 mm. We combined coarse- and fine-breast phantoms,[13] with volumetric breast densities that varied from 5% to 60% to improve the realism of the anthropomorphic breast phantoms.

The simulation of medio-lateral (ML) breast compression uses a GPU accelerated 3D mesh software.[14] The breast tissue compression was simulated using neo-Hookean models, with Poisson ratio of 0.49 and Young's modulus of 12.75 kPa, to reduce the phantom thickness by 50% (thickness=63.3 mm).[6]

Single calcifications were simulated using one- and two- voxel polycubes,[13] with voxel sizes of 100 μm^3. The calcification composition was varied by a weighting factor, which controls the calcification attenuation in the synthesized x-ray image. This factor represents the fraction of hydroxyapatite in the calcifications. The weighting factor was varied in 0.55, 0.65, and 0.75 of hydroxyapatite. We inserted a dense array of 42 calcifications, arranged 20 mm apart, into each compressed breast phantoms. The array was positioned in the central plane parallel to detector at the level of the nipple (ML phantom view). The method used for inserting calcifications into the breast phantoms was described in previous studies.[8,15]

In this study, we simulated the NGT acquisition geometry to synthesize DBT projections of the breast phantoms with and without calcifications. The image acquisition was simulated using step-and-shoot tube motion, and the angular range of the x-ray source was simulated using ±7.5°. In total, 15 equally-spaced DBT projections were simulated using the Siddon algorithm for x-ray tracing.[16] The DBT projections were generated using 0.085 mm^2 del, with a detector contained a total of 3584×2816 dels. The DBT images were reconstructed using 0.085 mm and 0.0425 mm reconstructed voxel sizes. DBT images reconstructed with 0.0425 mm voxel size represent the SR images. The images were reconstructed only at the central ML phantom view to accelerate the image simulations. The reconstructed DBT images were synthesized using the Briona software (Real-Time Tomography, Villanova, PA).[17]

We cropped regions of interest (ROIs) with and without calcifications, with sizes of 175×175 and 350×350 pixels for each image reconstructed using 0.085 mm and 0.0425 mm reconstructed voxel size, respectively. The ROIs with lesions were selected with the calcifications centered at the ROI.

2.2 Virtual Readers and ROC analyses

Channelized Hotelling observers (CHOs) were trained and tested to simulate five virtual readers.[18,19] The CHOs were simulated using 15 Laguerre-Gauss (LG) channels. We used LG spread sizes of 26 and 52, for each image reconstructed with reconstructed voxel size of 0.085 mm and 0.0425 mm, respectively. For each reader, independent training and testing image sets included 252 ROIs with simulated calcifications and 252 calcification-free ROIs. The readers were tested with a common image set that also included 252 ROIs. The ROIs used for training and testing were selected randomly.

We measured the readers' performance in calcification detection using MRMC ROC analyses provided by the MeVIC software (Barco NV, Kortrijk, Belgium).[20] The MeVIC software provides a separate module that estimates one-shot MRMC statistics.[11,21] We calculated the ROCs of each individual reader using the readers' scores. We analyzed the differences in area under the curve (AUC) and SE AUC between readers. We also evaluated differences in AUC between SR images and images reconstructed with 0.085 mm voxel size. Finally, we calculated the one-shot MRMC, which summarizes the ROC statistics of five readers.

3. RESULTS & DISCUSSION

The following parameters were varied and evaluated in our DBT simulations: number of calcification voxels (100 and 200 μm^3), weighting factor (0.55, 0.65, and 0.75), and reconstructed voxel size (0.085 mm and 0.0425 mm). The detector element was not varied, so we can evaluate the performance of each individual reader in calcification detection using smaller reconstructed voxel sizes (i.e., SR images). The pooled ROC curves of mixed calcifications using the three weighting factors are shown in Figure 1. Note that there is a small variation between readers for each analyzed condition because of the large number of ROIs used for training and testing. There is a slightly improvement in the ROC operating points for images reconstructed using 0.0425 mm reconstructed voxel size. The improvement in calcification detection using smaller reconstructed voxels is more prominent for 1-voxel calcifications.

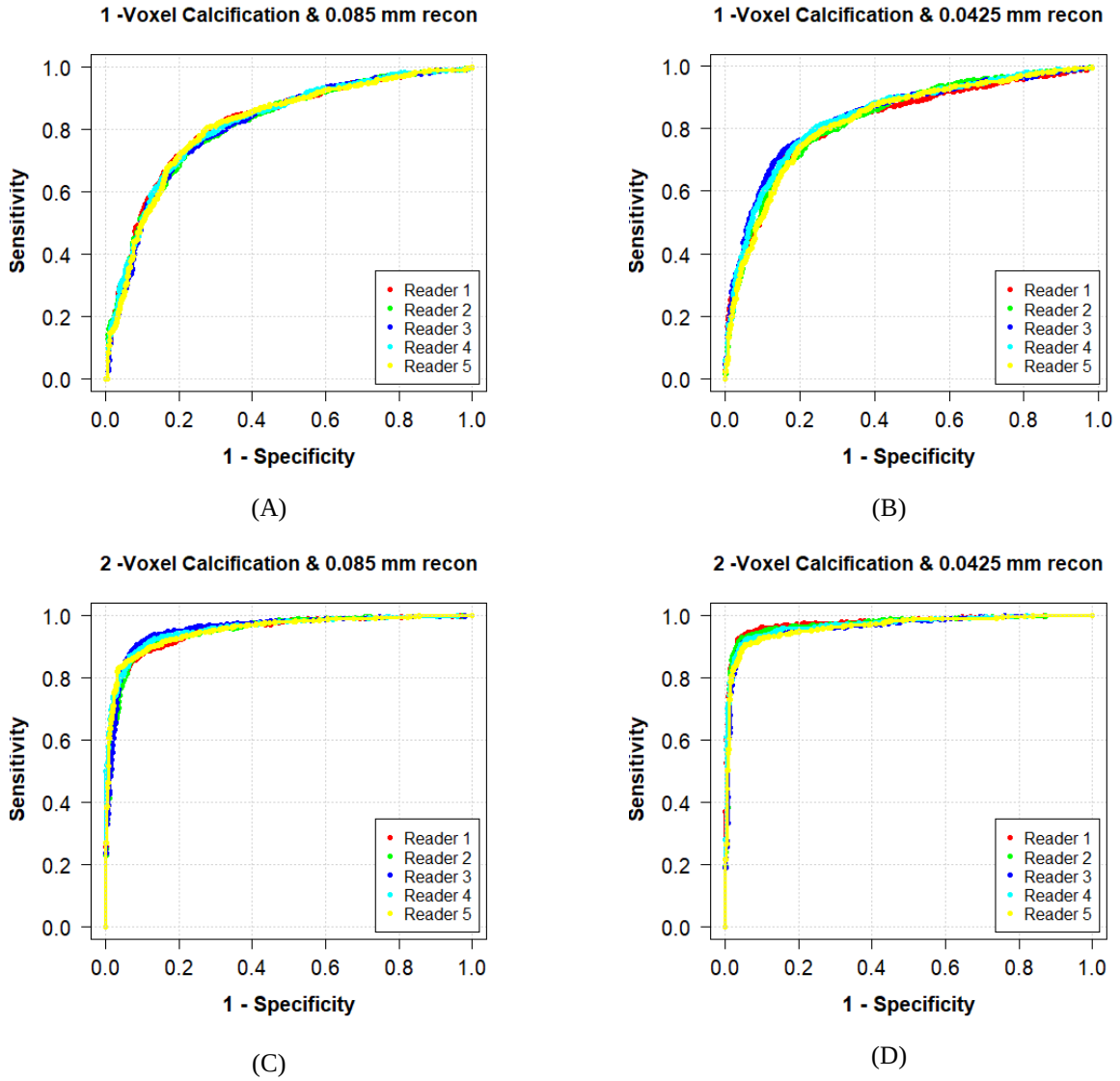

Figure 1. ROC curves of each individual reader using the image set: (A) 1-voxel calcifications and 0.085 mm reconstructed voxel size, (B) 1-voxel calcifications and 0.0425 mm reconstructed voxel size, (C) 2-voxel calcifications and 0.085 mm reconstructed voxel size, and (D) 2-voxel calcifications and 0.0425 mm reconstructed voxel size.

The AUC results of each reader are summarized in Table 1. Note that SR images (Table 1B and Table 1D) have an AUC improvement in calcification detection. For DBT projections simulated using 0.085 mm del, the calcification detection is substantially affected using SR images. The SR impact is more prominent for images synthesized using 1-voxel calcifications.

For calcification detection, the differences in AUC between SR images and images synthesized with 0.085 mm reconstructed voxel size were calculated using the one-shot MRMC ROC statistics. The differences in AUC were approximately 0.021 and 0.016 for DBT images simulated using 1- and 2-voxel calcifications, respectively (Figure 2). Although the AUC difference is higher for 1-voxel calcifications, the standard deviation is also higher. Due to the small detector element size used to simulate the reconstructed DBT images (del = 0.085 mm), the 1-voxel calcifications are close to the noise levels in the images (voxel size = 100 μm^3).

Table 1. Summary of the AUCs of each individual reader. Standard error (SE) AUC, 95% CI upper and lower are shown.

	(A) 1-Voxel Calcification & 0.085 mm recon					(B) 1-Voxel Calcification & 0.0425 mm recon				
	Reader 1	**Reader 2**	**Reader 3**	**Reader 4**	**Reader 5**	**Reader 1**	**Reader 2**	**Reader 3**	**Reader 4**	**Reader 5**
AUC	0.8198	0.8139	0.8124	0.8186	0.8153	0.8292	0.8324	0.8454	0.8467	0.8295
SE AUC	0.0109	0.0109	0.0111	0.0109	0.0111	0.0106	0.0104	0.0101	0.01	0.0106
95% CI upper	0.8411	0.8354	0.8341	0.8399	0.837	0.8501	0.8528	0.8652	0.8663	0.8502
95% CI lower	0.7985	0.7925	0.7907	0.7973	0.7937	0.8084	0.8119	0.8255	0.8271	0.8087
	(C) 2-Voxel Calcification & 0.085 mm recon					**(D) 2-Voxel Calcification & 0.0425 mm recon**				
	Reader 1	**Reader 2**	**Reader 3**	**Reader 4**	**Reader 5**	**Reader 1**	**Reader 2**	**Reader 3**	**Reader 4**	**Reader 5**
AUC	0.95069	0.95143	0.95821	0.9582	0.9545	0.97859	0.97392	0.96476	0.97191	0.96524
SE AUC	0.00527	0.00517	0.00502	0.00482	0.00507	0.00346	0.00401	0.00464	0.00396	0.00452
95% CI upper	0.96102	0.96157	0.96806	0.96764	0.96443	0.98538	0.98178	0.97385	0.97966	0.9741
95% CI lower	0.94037	0.9413	0.94836	0.94876	0.94457	0.97181	0.96606	0.95566	0.96415	0.95638

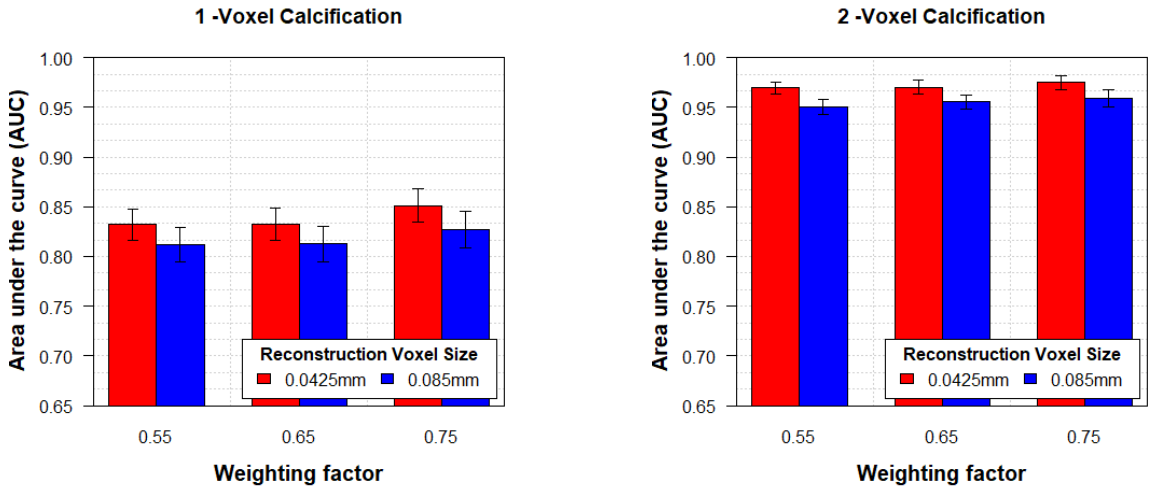

(A) (B)

Figure 2. Summary of the AUCs of one-shot MRMC ROC analyses, categorized by weighing factor. Standard deviations between five virtual readers are shown.

4. CONCLUSION

Computed-SR is superior to conventional reconstruction methods for calcification detection in DBT. In this study, the impact of SR on calcification detection is more prominent for small calcifications. These results are preliminary; however, we believe they provide guidance on how to improve the detectability of calcifications, which is an ongoing problem in tomosynthesis. Analysis of how additional conditions may affect calcification detection are forthcoming. By the IWBI meeting, we propose to evaluate calcification detection in DBT using SR images synthesized with larger detector element sizes, larger calcifications, and variable range of weighting factors. We also propose to calculate the *d'* statistics and validate results acquired using the one-shot MRMC ROC.

REFERENCES

[1] Gur, D., Abrams, G. S., Chough, D. M., Ganott, M. a., Hakim, C. M., Perrin, R. L., Rathfon, G. Y., Sumkin, J. H., Zuley, M. L. and Bandos, A. I., "Digital breast tomosynthesis: Observer performance study," Am. J. Roentgenol. **193**(2), 586–591 (2009).

[2] Poplack, S. P., Tosteson, T. D., Kogel, C. A. and Nagy, H. M., "Digital breast tomosynthesis: Initial experience in 98 women with abnormal digital screening mammography," Am. J. Roentgenol. **189**(3), 616–623 (2007).

[3] Rafferty, E. A., Park, J. M., Philpotts, L. E., Poplack, S. P., Sumkin, J. H., Halpern, E. F. and Niklason, L. T., "Diagnostic accuracy and recall rates for digital mammography and digital mammography combined with one-view and two-view tomosynthesis: Results of an enriched reader study," Am. J. Roentgenol. **202**(2), 273–281 (2014).

[4] Maidment, T. D., Vent, T. L., Ferris, W. S., Wurtele, D. E., Acciavatti, R. J. and Maidment, A. D. A., "Comparing the imaging performance of computed super resolution and magnification tomosynthesis," Med. Imaging 2017 Phys. Med. Imaging **10132**, 1013222 (2017).

[5] Barufaldi, B., Bakic, P. R., Higginbotham, D. and Maidment, A. D. A., "OpenVCT: a GPU-accelerated virtual clinical trial pipeline for mammography and digital breast tomosynthesis," SPIE Med. Imaging 2018 **1057358**(March), 1–8, Houston, TX (2018).

[6] Barufaldi, B., Bakic, P. R., Pokrajac, D. D., Lago, M. A. and Maidment, A. D. A., "Developing populations of software breast phantoms for virtual clinical trials," 14th Int. Work. Breast Imaging (IWBI 2018)(July), 73 (2018).

[7] Badano, A., Graff, C. G., Badal, A., Sharma, D., Zeng, R., Samuelson, F. W., Glick, S. J. and Myers, K. J., "Evaluation of Digital Breast Tomosynthesis as Replacement of Full-Field Digital Mammography Using an In Silico Imaging Trial," JAMA Netw. Open **1**(7), 1–12 (2018).

[8] Barufaldi, B., Bakic, P. R. and Maidment, A. D. A., "Multiple-reader, multiple-case ROC analysis for determining the limit of calcification detection in tomosynthesis," SPIE Med. Imaging 2019 Phys. od Med. Imaging **10948**(March), 22 (2019).

[9] Elangovan, P., Mackenzie, A., Dance, D. R., Young, K. C., Cooke, V., Wilkinson, L., Given-Wilson, R. M., Wallis, M. G. and Wells, K., "Design and validation of realistic breast models for use in multiple alternative forced choice virtual clinical trials," Phys. Med. Biol. (2017).

[10] Vent, T. L., Barufaldi, B. and Maidment, A. D. A., "Simulation and experimental validation of high-resolution test objects for evaluating a next-generation digital breast tomosynthesis prototype," SPIE Med. Imaging 2019(March), 21 (2019).

[11] Gallas, B. D., "One-shot estimate of MRMC variance: AUC," Acad. Radiol. **13**(3), 353–362 (2006).

[12] Pokrajac, D. D., Maidment, A. D. A. and Bakic, P. R., "Optimized generation of high resolution breast anthropomorphic software phantoms," Med. Phys. **39**(4), 2290 (2012).

[13] Bakic, P. R., Barufaldi, B., Pokrajac, D., Weinstein, S. P. and Maidment, A. D., "Optimized simulation of breast anatomy for virtual clinical trials," 14th Int. Work. Breast Imaging (IWBI 2018)(July), 73 (2018).

[14] Lago, M. A., Maidment, A. D. A. and Bakic, P. R., "Modelling of mammographic compression of anthropomorphic software breast phantom using FEBio," Int'l Symp. Comput. Methods Biomech. Biomed. Eng., Salt Lake City, UT (2013).

[15] Bakic, P. R., Barufaldi, B., Higginbotham, D., Weinstein, S. P., Avanaki, A., Espig, K., Xthona, A., Kimpe, T. and Maidment, A. D. A., "Virtual clinical trial of lesion detection in digital mammography and digital breast tomosynthesis," SPIE Med. Imaging 2018 **1057306**(March), 1–13 (2018).

[16] Siddon, R. L., "Fast calculation of the exact radiological path for a three dimensional CT array," Med. Phys. **12**(2), 252–255 (1985).

[17] Kuo, J., Ringer, P. A., Fallows, S. G., Bakic, P. R., Maidment, A. D. A. and Ng, S., "Dynamic reconstruction and rendering of 3D tomosynthesis images," SPIE Med. Imaging **796116**(March 2011), 796116-796116–11, Orlando, FL (2011).

[18] Abbey, C. K. and Barrett, H. H., "Human- and model-observer performance in ramp-spectrum noise: effects of regularization and object variability," J. Opt. Soc. Am. A (2001).

[19] Park, S., Zhang, G. and Myers, K. J., "Comparison of Channel Methods and Observer Models for the Task-Based Assessment of Multi-Projection Imaging in the Presence of Structured Anatomical Noise," IEEE Trans. Med. Imaging **35**(6), 1431–1442 (2016).

[20] Marchessoux, C., Kimpe, T. and Bert, T., "A virtual image chain for perceived and clinical image quality of medical display," IEEE/OSA J. Disp. Technol. **4**(4), 356–368 (2008).

[21] Gallas, B. D. and Barrett, H. H., "Validating the use of channels to estimate the ideal linear observer.," J. Opt. Soc. Am. A. Opt. Image Sci. Vis. **20**(9), 1725–1738 (2003).

Simulation of High-Resolution Test Objects using Non-Isocentric Acquisition Geometries in Next-Generation Digital Tomosynthesis

Trevor L. Vent, Bruno Barufaldi, Raymond J. Acciavatti, Andrew D.A. Maidment
University of Pennsylvania, Department of Radiology, 3400 Spruce Street, Philadelphia PA 19104

ABSTRACT

Digital breast tomosynthesis (DBT) systems utilize an isocentric acquisition geometry which introduces imaging artifacts that are deleterious to image reconstructions. The next-generation tomosynthesis (NGT) prototype was designed to incorporate various x-ray source and detector motions to investigate alternative acquisition geometries and improve microcalcification detection for DBT. Non-isocentric acquisition geometries, acquisitions that vary the image magnification between projection images, are capable of ameliorating aliasing and other artifacts that are intrinsic to conventional DBT. We used virtual clinical trials (VCTs) to develop custom acquisition geometries for the NGT prototype. A high-resolution (5μm voxel size) star pattern test object was simulated to compare the high-frequency performance of isocentric with non-isocentric acquisition geometries. Three x-ray source-motion paths were simulated to obtain super-sampled image reconstructions of the virtual star pattern. An aliasing-sensitive metric was used to evaluate spatial resolution performance for two frequency orientations. Pairwise comparisons were made for twelve conditions between the isocentric and non-isocentric acquisition geometries. Non-isocentric acquisition geometries show an improvement over isocentric acquisition geometries for all six conditions. The greatest improvement was 75.2% for frequencies aligned perpendicular to x-ray source motion, which is the direction of frequencies for which DBT is prone to aliasing. All six non-isocentric conditions exhibit super-resolution, whereas half of the isocentric conditions were prone to aliasing.

1. INTRODUCTION

Digital breast tomosynthesis (DBT) acquires a three-dimensional (3D) image of a patient's breast by acquiring multiple, two-dimensional x-ray images from serial source positions. For a conventional DBT acquisition, the x-ray projections are acquired by translating the x-ray source along an arc in the mediolateral (ML) direction. The projections are typically spaced equidistantly in the chest-wall plane of the patient. This **acquisition geometry**, defined as the configuration of 2D x-ray projection images that are used for the 3D image reconstruction is Isocentric, meaning that the arc is centered about a single point in space. Such DBT systems benefit the detection of masses and low-frequency objects in the breast[1]. That said, results considering high-frequency objects, like microcalcifications, are only marginally superior when compared with full-field digital mammography. Resolution for conventional DBT is anisotropic, favoring the frequencies that are aligned parallel to x-ray source motion.

The next-generation tomosynthesis (NGT) system is a DBT prototype that was designed to improve the detection of microcalcifications in the breast. This prototype system investigates alternative acquisition geometries by introducing novel x-ray source and detector motions. Introducing posteroanterior (PA) x-ray source motion has been shown to improve spatial resolution with super-sampling techniques in the image reconstruction[2–5] and the volume estimation of anthropomorphic breast phantoms[6,7]. Non-isocentric acquisition geometries can improve spatial sampling further and lessen the impact of imaging artifacts like, masking[8,9], spatial resolution anisotropies[10,11], and aliasing[11,12], to which conventional DBT is prone. Non-isocentric geometries also avoid degeneracies in the reconstructed volume[13].

Clinical trials of medical imaging systems require a large number of patients, who are imaged repeatedly to compare the performance of different systems. The associated cost, duration, and radiation risk represent a significant impediment to the efficient introduction of novel imaging technologies. Virtual clinical trials (VCTs) represent an approach, based upon computer simulation of human anatomy and imaging modalities, which can help develop, optimize, and validate new and existing medical imaging methods. Fast and detailed simulations of device performance are also instrumental in prototyping clinical trials and augmenting them with simulated data, and may also assist with regulatory approval[4,14,15]. VCTs have become particularly popular for breast imaging research, because of the low prevalence of breast cancer in screening populations.

Physics VCTs, in contrast to traditional VCTs, are intended to evaluate the implementation of the novel designs using simulated image acquisitions of virtual test objects and objective metrics to evaluate device performance. We have used

Physics VCTs to investigate novel acquisition geometries for the NGT prototype[4]. We have shown that physics VCTs can be used to investigate novel acquisition geometries for the NGT system without exhausting valuable resources. In this work, we use physics VCTs and a voxelized star pattern test object to compare the performance of isocentric and non-isocentric acquisition geometries for DBT using the simulated configuration of the NGT prototype.

2. MATERIALS

Virtual Clinical Trial pipeline

Physics VCTs are implemented using our X-ray Physics Lab's (XPL) physics VCT pipeline. The physics VCT pipeline has been modified from the original VCT pipeline. Physics VCTs simulate the image acquisition of physical test objects and phantoms. Rather than using a virtual reader phase of the original VCT pipeline, objective measures of physics are used to evaluate the performance of an imaging device. A tomosynthesis acquisition is simulated, in the same manner as the original pipeline, using ray-tracing methods with a dedicated graphics processing unit (GPU). The mechanical configuration of the NGT prototype is modeled using the physics VCT pipeline, where various acquisition geometries can be simulated.

Next-generation tomosynthesis prototype

The NGT system is a prototype device that is used to investigate alternative acquisition geometries for DBT. Alternative acquisition geometries are achieved by creating custom x-ray source and detector motion paths for the series of x-ray projection images. The collection of projection images obtained from each custom acquisition geometry are used for tomographic reconstructions.

The origin of the NGT system is defined at the center of the chest-wall edge of the breast support (Figure 1). The **x**-**y** plane of the NGT system serves as an address space for the x-ray focal spot to determine an acquisition geometry. The range of the source is ±150mm in **x** and +180mm in **y**. The NGT achieves non-isocentric acquisition geometries by translating the detector in **z** between x-ray projections with a 50mm range. The detector of the NGT prototype has a detector element size of 85µm.

The geometric configuration and constraints of the NGT prototype dictate the image acquisition simulation of the physics VCTs. Tomographic image reconstructions are created using commercial reconstruction software (Briona version 7.12, Real Time Tomography, Villanova, PA).

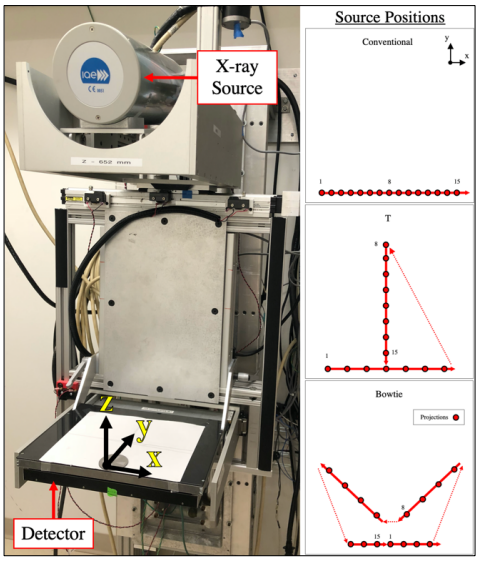

Figure 1: The NGT prototype and three typical acquisition geometries

Star pattern test object

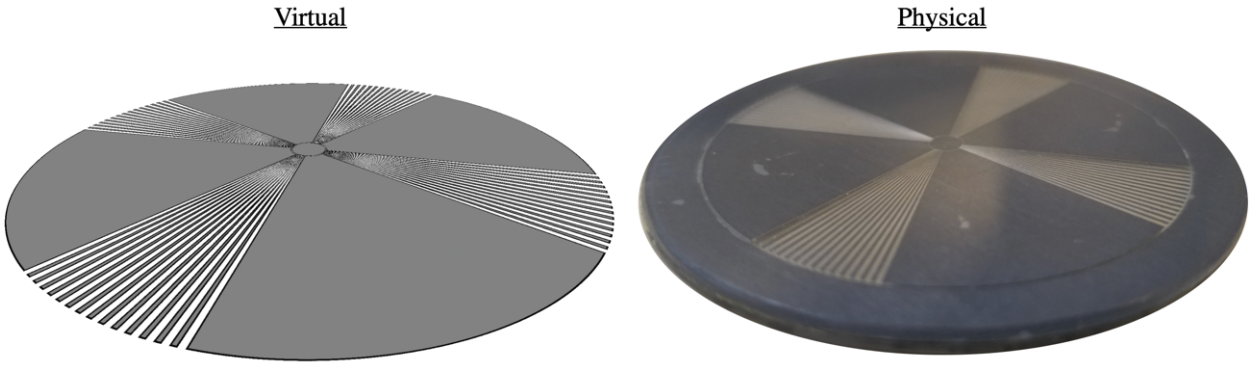

Figure 2: The virtual star pattern test object that was created to simulate the physical star pattern.

A voxelized model of a star pattern test object (Model 07-542-1000, Supertech, Elkhart, IN) was created using Matlab (MathWorks, Natick, Massachusetts, version 2018a). This virtual star pattern (Figure 2) consists of 5µm isotropic voxels with three material indices: lead, acrylic, and air. The diameter of the star pattern is 45mm with a total thickness of 30µm.

The range of resolution for this star pattern, from the outer edge to the innermost circle, is 1.3–20.0 line pairs per millimeter (lp/mm). This virtual phantom was used as the test object for simulated image acquisitions of the NGT prototype.

3. METHOD

Physics VCTs were used to simulate the image acquisition of the virtual star pattern using various configurations of the NGT prototype. In total, six acquisition geometries are considered. Three typical x-ray source motion paths (Figure 1, right) were simulated with and without **z**-direction detector motion, to simulate non-isocentric and isocentric acquisition geometries, respectively. Image reconstructions of the star pattern test object were obtained using the simulated 2D projection images of each image acquisition simulation.

The slice of the image reconstruction that contained the plane of the star pattern was used to evaluate the resolution properties of each image reconstruction. An aliasing-sensitive spatial resolution metric (Radial FFT)[16] was used to evaluate the spatial resolution performance of all six acquisition geometries. This metric used the star pattern image as an input to produce the contrast transfer function (CTF) and radial fast Fourier transform (RFFT) graphs (e.g. Figure 4). The CTF is analogous to the modulation transfer function (MTF) but is not normalized to unity at the zero spatial frequency. The RFFT graph shows modulation of all frequencies contained in a quadrant of a star pattern image reconstruction with the modulation of aliased signals. The CTF was used to determine the limit of spatial resolution (LSR). Conventional DBT is spatially anisotropic[11]; therefore, each image reconstruction is evaluated for frequencies aligned parallel to both **x** and **y**.

4. RESULTS AND DISCUSSION

Simulated image reconstructions

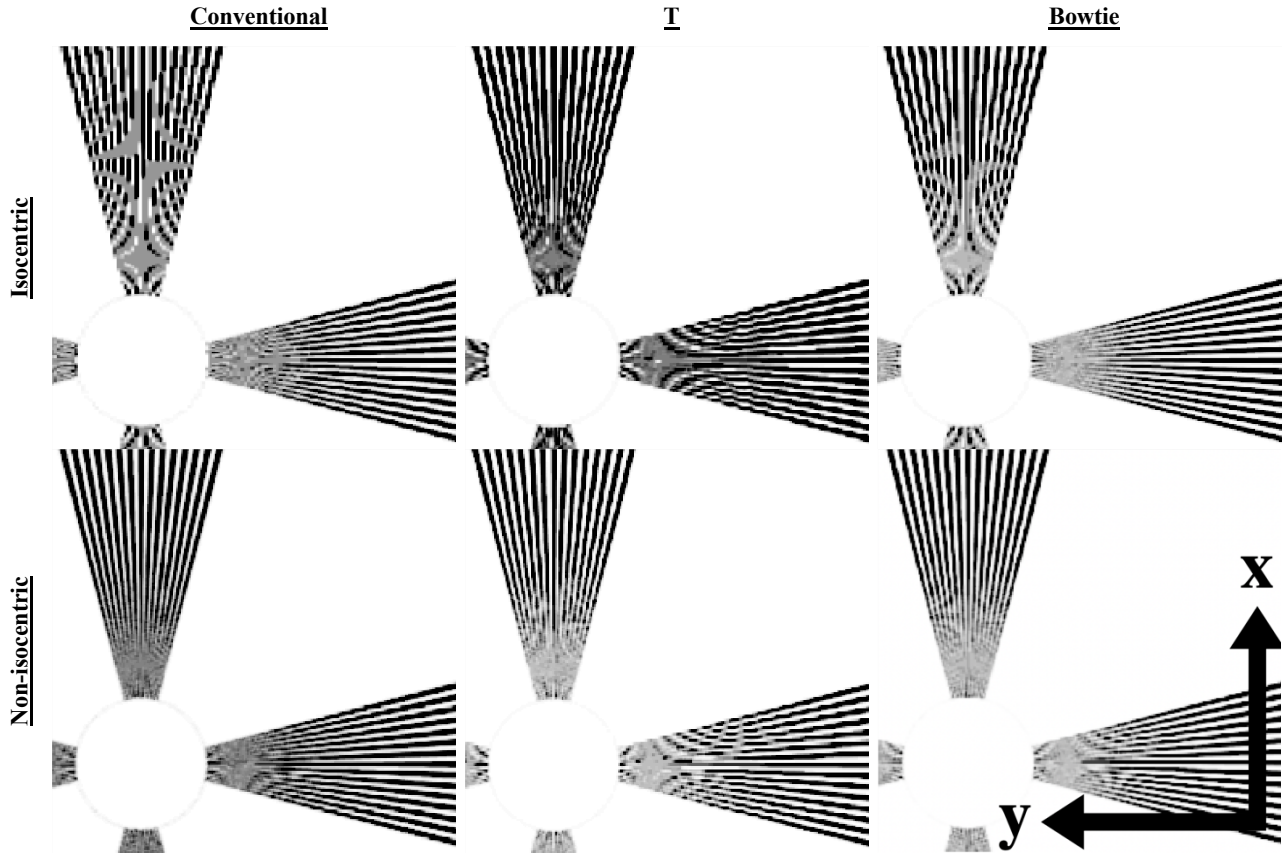

Figure 3: Simulated image reconstructions of the isocentric and non-isocentric acquisition geometries.

The isocentric acquisition geometries show more significant aliasing in the form of Moiré patterns compared with the non-isocentric acquisition geometries (Figure 3). The non-isocentric acquisition geometries exhibit more isotropic resolution than the isocentric acquisition geometries. The modulation contrast appears to be higher for the isocentric acquisition geometries at the lower spatial frequencies. The results vary also by source-motion path; the greatest improvement of isocentric to non-isocentric geometries appears to be that of the conventional acquisition geometry.

Radial FFT

The Radial FFT was computed for all twelve conditions. The RFFT and CTF graphs of the non-isocentric acquisition geometries show a reduction of measurement noise compared with the isocentric acquisition geometries. Figure 4 is an example of the comparison of isocentric with non-isocentric acquisition geometries for the conventional source-motion path.

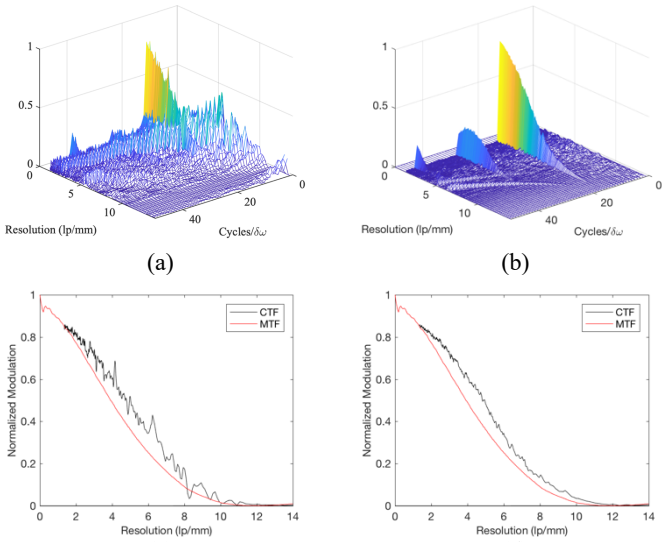

Figure 4: (a) Radial FFT for conventional, isocentric geometry, (b) Radial FFT for conventional, non-isocentric geometry, (c) MTF vs. CTF for conventional isocentric geometry, (d) MTF vs. CTF for conventional, non-isocentric geometry.

Limit of spatial resolution

The LSR of the twelve conditions was measured using images of the star pattern and the CTF. Various image reconstructions exhibited significant aliasing, and the LSR was limited to near the alias frequency of the detector (5.88 lp/mm). For cases where super-resolution was achieved, the LSR was measured at a 5% modulation of the CTF. The measured LSR for the twelve conditions tested and the improvement of non-isocentric over isocentric acquisition geometries are reported in Table 1.

Table 1: Summary of the limit of spatial resolution for all simulated conditions.

	Isocentric (lp/mm)		**Non-Isocentric (lp/mm)**		**Difference (%)**	
Source Motion	**x**	**y**	**x**	**y**	**x**	**y**
Bowtie	9.44	8.24	9.99	9.98	5.8	21.1
Conventional	9.34	5.81	10.21	10.18	9.4	**75.2**
T-Shape	5.83	5.84	9.75	9.68	67.2	65.8

These results represent a single simulation. The VCT software can use perturbative methods to shift the phantom slightly to simulate the removal and positioning of the phantom between acquisitions. We can use this method to simulate multiple acquisitions to validate these results statistically and obtain an analysis of the error.

5. CONCLUSION

We have shown that non-isocentric acquisition geometries can be simulated using physics VCTs. The LSR improved for every frequency orientation with the introduction of **z**-detector motion. The highest overall improvement in LSR for the non-isocentric over isocentric acquisition geometries is the **y**-direction frequencies of the conventional x-ray source motion path (75.2%). All six non-isocentric conditions exhibit super-resolution, whereas half of the isocentric conditions were prone to aliasing. These results suggest that the NGT prototype is capable of isotropic super-resolution with proper calibration. We will validate the results of the physics VCTs using experimental images acquired on the physical NGT prototype with proper geometric calibration.

REFERENCES

[1] Rafferty, E. a, Park, J. M., Philpotts, L. E., Poplack, S. P. and Sumkin, J. H., "Digital Mammography and Breast Tomosynthesis Compared with Digital Mammography Alone : Results of a Multicenter, multireader trial," Radiology **266**(1), 104–113 (2013).

[2] Eben, J. E., Vent, T. L., Choi, C. J., Yarrabothula, S., Chai, L., Nolan, M., Kobe, E., Acciavatti, R. J. and Maidment, A. D. A., "Development of a next generation tomosynthesis system," Prog. Biomed. Opt. Imaging - Proc. SPIE **10573** (2018).

[3] Maidment, T. D., Vent, T. L., Ferris, W. S., Wurtele, D. E., Acciavatti, R. J. and Maidment, A. D. A., "Comparing the imaging performance of computed super resolution and magnification tomosynthesis," Med. Imaging 2017 Phys. Med. Imaging **10132**, 1013222 (2017).

[4] Vent, T. L., Barufaldi, B. and Maidment, A. D. A., "Simulation and experimental validation of high-resolution test objects for evaluating a next-generation digital breast tomosynthesis prototype," 21 (2019).

[5] Vent, T. L., Lepore, B. L. and Maidment, A. D. A., "Evaluating the imaging performance of a next-generation digital breast tomosynthesis prototype," Med. Imaging 2019 Phys. Med. Imaging(March), 19 (2019).

[6] Acciavatti, Raymond; Rodriguez-Ruiz, Alejandro; Vent, Trevor L.; Bakic, Predrag R.; Reiser, Ingrid; Sechopoulos, Ioannis; Maidment, A. D. A., "Analysis of volume overestimation artifacts in the breast outline segmentation in tomosynthesis," Med. Imaging 2018 Phys. Med. Imaging, 10573 (2018).

[7] Acciavatti, R. J., Barufaldi, B., Vent, T. L., Wileyto, E. P. and Maidment, A. D. A., "Personalization of x-ray tube motion in digital breast tomosynthesis using virtual Defrise phantoms," Med. Imaging 2019 Phys. Med. Imaging(March), 10 (2019).

[8] Friedewald, S. M., Rafferty, E. A., Rose, S. L., Durand, M. A., Plecha, D. M., Greenberg, J. S., Hayes, M. K., Copit, D. S., Carlson, K. L., Cink, T. M., Barke, L. D., Greer, L. N., Miller, D. P. and Conant, E. F., "Breast cancer screening using tomosynthesis in combination with digital mammography," JAMA - J. Am. Med. Assoc. **311**(24), 2499–2507 (2014).

[9] Roth, R. G., Maidment, A. D. A., Weinstein, S. P., Roth, S. O. and Conant, E. F., "Digital Breast Tomosynthesis: Lessons Learned from Early Clinical Implementation," RadioGraphics **34**(4), E89–E102 (2014).

[10] Hu, Y.-H., Zhao, B. and Zhao, W., "Image artifacts in digital breast tomosynthesis: Investigation of the effects of system geometry and reconstruction parameters using a linear system approach," Med. Phys. **35**(12), 5242–5252 (2008).

[11] Acciavatti, R. J. and Maidment, A. D. A., "Observation of super-resolution in digital breast tomosynthesis," Med. Phys. **39**(12), 7518–7539 (2012).

[12] Vent, T. L., Acciavatti, R. J., Kwon, Y. J. and Maidment, A. D. A., "Quantification of resolution in multiplanar reconstructions for digital breast tomosynthesis," Med. Imaging 2016 Phys. Med. Imaging **9783**(March 2016), 978303 (2016).

[13] Hatt, C. R., Tomkowiak, M. T., Dunkerley, D. A. P., Slagowski, J. M., Funk, T., Raval, A. N. and Speidel, M. A., "Depth-resolved registration of transesophageal echo to x-ray fluoroscopy using an inverse geometry fluoroscopy system," Med. Phys. **42**(12), 7022–7033 (2015).

[14] Bakic, P. R., Barufaldi, B., Pokrajac, D., Lago, M. A. and Maidment, A. D., "Developing populations of software breast phantoms for virtual clinical trials," 14th Int. Work. Breast Imaging (IWBI 2018)(July 2018), 73 (2018).

[15] Barufaldi, B., Bakic, P. R., Higginbotham, D. and Maidment, A. D. A., "OpenVCT: a GPU-accelerated virtual clinical trial pipeline for mammography and digital breast tomosynthesis," Med. Imaging 2018 Phys. Med. Imaging **1057358**(March), 194 (2018).

[16] Vent, T., Acciavatti, R. and Maidment, A., "Development and Evaluation of a Spatial Resolution Metric for Tomosynthesis: we-g-601-02," Med. Phys. **44**(6), 3261 (2017).

4A.

Automation of Virtual Clinical Trials Used to Evaluate Efficacy of Breast Cancer Screening Modalities

Brian-Tinh Vu[1, 2], Bruno Barufaldi[1], Trevor Vent[1], Raymond Acciavatti[1], Andrew Maidment[1].

[1] Department of Radiology, Perelman School of Medicine, University of Pennsylvania, Philadelphia, PA 19104, [2] Department of Physics, University of Houston, Houston, TX 77004

Clinical trials aimed at evaluating the relative efficacies of breast cancer screening modalities are often delayed by the need to recruit patients. Virtual clinical trials (VCTs) save time and cost by circumventing the need for patient recruitment while providing researchers the ability to finely control parameters of a virtual breast. *OpenVCT* has shown it can accurately simulate 2D and 3D breast screening modalities. In this study, the following steps of the *OpenVCT* pipeline were automated: lesion insertion, x-ray projection, 3D reconstruction, and isolation of regions of interest (ROIs) containing lesions. Automation of the pipeline removes the need for human presence during the experiments altogether. Digital mammography (DM), digital breast tomosynthesis (DBT), and synthetic 2D mammography (a 2D alternative to DM by processing 3D images from DBT) experiments were conducted with 36 phantoms; each phantom had differing tissue structure and was presented to the pipeline. From these, 1296 additional phantoms were generated, each with 42 equally-spaced calcifications (milk-like secretions) varying in lesion size (0.1-0.5 mm) and weighting fraction (how subtle the lesion appears) inserted in the breast's midplane. At the end of the automated pipeline 42 regions of interest containing calcifications were isolated from each phantom in preparation for model observers to generate the receiver operating characteristic curve, used for measuring true positive and false positive rates. This process took 4.28 days, or approximately 2.86 hours per phantom. The implementation and automation of *OpenVCT* in Python will further solidify its use as a cost- and time-saving tool in the evaluation of breast cancer x-ray imaging modality efficacy. The implementation of the pipeline's functions in Python, a high-level and open-source programming language, make them accessible to scientists without an extensive programming background. The automated pipeline currently is being used in the evaluation of efficacies of conventional DM, DBT, and synthetic 2D mammography.

5A.

High Resolution Profiling of EGFR Mutations in Glioblastoma Patients using an Ultrasensitive Digital PCR Approach

Sujay Ratna[1,2], Deeksha Saxena[1], Jay Dorsey[1]. [1]Department of Radiation Oncology, Smilow Center for Translational Research, Perelman School of Medicine, University of Pennsylvania, Philadelphia, PA 19104; [2]Rutgers University

Glioblastoma Multiforme (GBM) is the most aggressive adult brain cancer. The average survival time after GBM diagnosis is 14.6 months even with current trimodality therapy. In 57% of gliomas, the Epidermal Growth Factor Receptor, a tyrosine kinase gene, is amplified. Mutations such as EGFR variant III, A289V, and R108K lead to more aggressive & malignant tumors, and a lower survival time. We are in need of an assay that detects these mutations as soon as possible since other assays currently available in clinical workflows, like Next Generation Sequencing, may take up to 3-4 weeks. Our lab has established a very sensitive and novel digital Polymerase Chain

W81XWH-18-1-0082 (BC170226): Design of a 3D Mammography System in the Age of Personalized Medicine

PI: Raymond J. Acciavatti, University of Pennsylvania

Budget: $603,749.00 **Topic Area:** Breast Cancer Research Program **Mechanism:** Breakthrough Award-Level 1

Research Area: X-Ray Imaging (708) Digital Imaging (704) **Award Status: Open** March 15, 2018 to March 14, 2021

Study Goals:

Even with the latest "3D" digital breast tomosynthesis systems, most women that are recalled for follow-up testing after a suspicious mammogram are ultimately found to be cancer-free. To improve the sensitivity and specificity of breast imaging for cancer detection, we are proposing to re-design mammography systems around the principle of "personalized medicine", so that the orbits of the detector and x-ray tube are customized to the size, shape, and composition of each breast. The new designs for both screening and diagnostic mammography will be validated with a virtual clinical trial using realistic simulations of breast anatomy and a highly-validated observer model.

Specific Aims:

SA1. Design a personalized image acquisition technique for screening mammography.
SA2. Design a 3D magnification mammography call-back exam.
SA3. Evaluate the new designs for screening and call-back imaging with a virtual clinical trial.

Key Accomplishments:

Publications:

1. Acciavatti RJ, Barufaldi B, Vent TL, Wileyto EP, Maidment ADA. Personalization of x-ray tube motion in digital breast tomosynthesis using virtual Defrise phantoms. In: Schmidt TG, Chen G-H, Bosmans H, editors; Physics of Medical Imaging; 2019; San Diego, CA: SPIE; 2019. p. 109480B.
2. Acciavatti RJ, Maidment ADA. Non-stationary model of oblique x-ray incidence in amorphous selenium detectors: I. Point spread function. Medical Physics. 2019; 46(2):494-504.
3. Acciavatti RJ, Maidment ADA. Nonstationary model of oblique x-ray incidence in amorphous selenium detectors: II. Transfer Functions. Medical Physics. 2019; 46(2); 505-16.
4. Acciavatti RJ, Vent TL, Barufaldi B, Wileyto EP, Noël PB, Maidment ADA. Proposing Rapid Source Pulsing for Improved Super-Resolution in Digital Breast Tomosynthesis. In: Chen G-H, Bosmans H, editors; Physics of Medical Imaging; 2020; Houston, TX: SPIE; 2020. p. 113125G.
5. Acciavatti RJ, Cohen EA, Maghsoudi OH, Gastounioti A, Pantalone L, Hsieh M-K, Conant EF, Scott CG, Winham SJ, Kerlikowske K, Vachon C, Maidment ADA, Kontos D. Robust Radiomic Feature Selection in Digital Mammography: Understanding the Effect of Imaging Acquisition Physics Using Phantom and Clinical Data Analysis. In: Hahn HK, Mazurowski MA, editors; Computer-Aided Diagnosis; 2020; Houston, TX: SPIE; 2020. p. 113140W.
6. Barufaldi B, Vent TL, Acciavatti RJ, Bakic PR, Noël PB, Conant EF, Maidment ADA. Determining the Optimal Angular Range of the X-Ray Source Motion in Tomosynthesis Using Virtual Clinical Trials. In: Chen G-H, Bosmans H, editors; Physics of Medical Imaging; 2020; Houston, TX: SPIE; 2020. p. 113120I.
7. Acciavatti RJ, Cohen EA, Maghsoudi OH, Gastounioti A, Pantalone L, Hsieh M-K, Barufaldi B, Bakic PR, Chen J, Conant EF, Kontos D, Maidment ADA. Calculation of Radiomic Features to Validate the Textural Realism of Physical Anthropomorphic Phantoms for Digital Mammography (IWBI 2020, in press).
8. Acciavatti RJ, Vent TL, Barufaldi B, Wileyto EP, Noël PB, Maidment ADA. Super-Resolution in Digital Breast Tomosynthesis: Limitations of the Conventional System Design and Strategies for Optimization (IWBI 2020, in press).
9. Barufaldi B, Vent TL, Acciavatti RJ, Bakic PR, Noël PB, Maidment ADA. MRMC ROC Analysis of Calcification Detection in Tomosynthesis Using Computed Super-Resolution and Virtual Clinical Trials (IWBI 2020, in press).
10. Vent TL, Barufaldi B, Acciavatti RJ, Maidment ADA. Simulation of High-Resolution Test Objects using Non-Isocentric Acquisition Geometries in Next-Generation Digital Tomosynthesis (IWBI 2020, in press).

Patents: None as of the end of Year 2 of this grant.

Funding Obtained: The PI (Raymond Acciavatti) was a mentor for the 2019 summer undergraduate fellowship program through the American Association of Physicists in Medicine (AAPM). Stipend funding was provided directly to the undergraduate student, who performed research in virtual clinical trials.